REPORT DOCUMENTATION PAGE

Form Approved OMB NO. 0704-0188

1. REPORT DATE (DD-MM-YYYY)	2. REPORT TYPE	3. DATES COVERED (From - To)
28-08-2013	Ph.D. Dissertation	-

4. TITLE AND SUBTITLE	5a. CONTRACT NUMBER
Development of HgCdSe for Third Generation Focal Plane Arrays using Molecular Beam Epitaxy	W911NF-10-1-0335
	5b. GRANT NUMBER
	5c. PROGRAM ELEMENT NUMBER
	611102

6. AUTHORS	5d. PROJECT NUMBER
Kevin Doyle	
	5e. TASK NUMBER
	5f. WORK UNIT NUMBER

7. PERFORMING ORGANIZATION NAMES AND ADDRESSES	8. PERFORMING ORGANIZATION REPORT NUMBER
Texas State University 601 University Dr. San Marcos, TX 78666 -4684	

9. SPONSORING/MONITORING AGENCY NAME(S) AND ADDRESS(ES)	10. SPONSOR/MONITOR'S ACRONYM(S)
U.S. Army Research Office P.O. Box 12211 Research Triangle Park, NC 27709-2211	ARO
	11. SPONSOR/MONITOR'S REPORT NUMBER(S)
	57432-EL.12

12. DISTRIBUTION AVAILIBILITY STATEMENT

Approved for public release; distribution is unlimited.

13. SUPPLEMENTARY NOTES

The views, opinions and/or findings contained in this report are those of the author(s) and should not contrued as an official Department of the Army position, policy or decision, unless so designated by other documentation.

14. ABSTRACT

ZnTe and ZnTe1-xSex layers were grown on GaSb substrates prepared with atomic hydrogen cleaning. The lattice constant of ZnTe1-xSex was tuned by controlling the ratio of Se/Te beam equivalent pressures, and ZnTe1-xSex was found to be lattice-matched to GaSb for x=0.01. Confocal photoluminescence measurements indicated that ZnTe0.99Se¬0.01 layers grown on GaSb have dislocation densities ~7x104 cm-2, indicating that ZnTe0.99Se¬0.01/GaSb provides a high quality substrate with low dislocation densities for Hg1 xCdxSe growth.

15. SUBJECT TERMS

HgCdSe, IR, MBE

16. SECURITY CLASSIFICATION OF:			17. LIMITATION OF ABSTRACT	15. NUMBER OF PAGES	19a. NAME OF RESPONSIBLE PERSON
a. REPORT	b. ABSTRACT	c. THIS PAGE	UU		John Dinan
UU	UU	UU			19b. TELEPHONE NUMBER
					512-245-6711

Development of HgCdSe for Third Generation Focal Plane Arrays using Molecular Beam Epitaxy

ABSTRACT

ZnTe and ZnTe1-xSex layers were grown on GaSb substrates prepared with atomic hydrogen cleaning. The lattice constant of ZnTe1-xSex was tuned by controlling the ratio of Se/Te beam equivalent pressures, and ZnTe1-xSex was found to be lattice-matched to GaSb for x=0.01. Confocal photoluminescence measurements indicated that ZnTe0.99Se¬0.01 layers grown on GaSb have dislocation densities ~7x104 cm-2, indicating that ZnTe0.99Se¬0.01/GaSb provides a high quality substrate with low dislocation densities for Hg1 xCdxSe growth.

In parallel with the ZnTe1-xSex/GaSb substrate development, the growth of Hg1 xCdxSe was studied via molecular beam epitaxy on GaSb substrates and Si substrates with ZnTe buffer layers. Growth rate, composition, and surface quality were evaluated for different growth parameters. Two sources of Se were used, an effusion cell loaded with 5N purity source material that produced a predominantly Se6 flux, and a disassociation source loaded with 6N purity source material that could produce either a predominantly Se2 or a predominantly Se6 flux. For a given substrate temperature and Hg overpressure, the growth rate was controlled by the Se flux and the x¬-value was controlled by the Cd/Se flux ratio. Growths under Hg-deficient conditions produced "needle" and "diamond"-shaped defects. The optimal substrate temperature was found to be 90-110 °C for growths performed with a predominantly Se6 flux from the effusion cell and a standard Hg flux of 2.5x10-4 Torr.

Previous studies of nominally undoped Hg1 xCdxSe samples have reported large background electron concentrations ranging from 1017-1018 cm-3 at temperatures as low as 4K. In the study reported here, the use of Se source material with 6N purity instead of 5N reduced the electron concentration in Hg1-xCdxSe by an order of magnitude, suggesting contaminants in the Se source material are a significant source of the background electrons. Certain anneals can alter the electron concentration of Hg1 xCdxSe, suggesting the presence of native point defects as well as background impurities. Positron annihilation spectroscopy measurements strongly suggest the presence of p-type mercury vacancies in Hg1 xCdxSe samples both as-grown and after annealing under an Se overpressure. Temperature-dependent Hall measurements of annealed samples suggest two donor energy levels: one in the bandgap with ionization energy of ~40 meV that produces an electron concentration of ~8x1015 cm-3 at 300K, and one in the conduction band with a concentration of ~2x1016 cm-3. The former could originate from n-type Se vacancies, while the latter is most likely impurities from the Se source material.

Development of $Hg_{1-x}Cd_xSe$ for 3rd Generation Focal Plane Arrays using Molecular Beam Epitaxy

Kevin Doyle

Dissertation submitted to the
Eberly College of Arts and Sciences
at West Virginia University
in partial fulfillment of the requirements
for the degree of

Doctor of Philosophy
in
Physics

David Lederman, Ph.D., Chair
Thomas H. Myers, Ph.D.
Mohinder Seehra, Ph.D.
Dimitris Korakakis, Ph.D
James P. Lewis, Ph.D.

Morgantown, West Virginia

2013

Keywords:
$Hg_{1-x}Cd_xSe$, $ZnTe_{1-x}Se_x$, GaSb, Molecular Beam Epitaxy, Infrared Materials

ABSTRACT

Development of $Hg_{1-x}Cd_xSe$ for 3rd Generation Focal Plane Arrays using Molecular Beam Epitaxy

Kevin Doyle

$Hg_{1-x}Cd_xSe$ grown on nearly lattice-matched GaSb substrates could serve as a new basis for infrared detector development. The preparation of the GaSb substrate surfaces and the growth of $ZnTe_{1-x}Se_x$ buffer layers via molecular beam epitaxy were investigated. ZnTe and $ZnTe_{1-x}Se_x$ layers were grown on GaSb substrates prepared with atomic hydrogen cleaning. The lattice constant of $ZnTe_{1-x}Se_x$ was tuned by controlling the ratio of Se/Te beam equivalent pressures, and $ZnTe_{1-x}Se_x$ was found to be lattice-matched to GaSb for x=0.01. Confocal photoluminescence measurements indicated that $ZnTe_{0.99}Se_{0.01}$ layers grown on GaSb have dislocation densities $\sim 7 \times 10^4$ cm^{-2}, indicating that $ZnTe_{0.99}Se_{0.01}$/GaSb provides a high quality substrate with low dislocation densities for $Hg_{1-x}Cd_xSe$ growth.

In parallel with the $ZnTe_{1-x}Se_x$/GaSb substrate development, the growth of $Hg_{1-x}Cd_xSe$ was studied via molecular beam epitaxy on GaSb substrates and Si substrates with ZnTe buffer layers. Growth rate, composition, and surface quality were evaluated for different growth parameters. Two sources of Se were used, an effusion cell loaded with 5N purity source material that produced a predominantly Se_6 flux, and a disassociation source loaded with 6N purity source material that could produce either a predominantly Se_2 or a predominantly Se_6 flux. For a given substrate temperature and Hg overpressure, the growth rate was controlled by the Se flux and the x-value was controlled by the Cd/Se flux ratio. Growths under Hg-deficient conditions produced "needle" and "diamond"-shaped defects. The optimal substrate temperature was found to be 90-110 °C for growths performed with a predominantly Se_6 flux from the effusion cell and a standard Hg flux of 2.5×10^{-4} Torr.

Previous studies of nominally undoped $Hg_{1-x}Cd_xSe$ samples have reported large background electron concentrations ranging from 10^{17}-10^{18} cm^{-3} at temperatures as low as 4K. In the study reported here, the use of Se source material with 6N purity instead of 5N reduced the electron concentration in $Hg_{1-x}Cd_xSe$ by an order of magnitude, suggesting contaminants in the Se source material are a significant source of the background electrons. Certain anneals can alter the electron concentration of $Hg_{1-x}Cd_xSe$, suggesting the presence of native point defects as well as background impurities. Positron annihilation spectroscopy measurements strongly suggest the presence of p-type mercury vacancies in $Hg_{1-x}Cd_xSe$ samples both as-grown and after annealing under an Se overpressure. Temperature-dependent Hall measurements of annealed samples suggest two donor energy levels: one in the bandgap with ionization energy of ~ 40 meV that produces an electron concentration of $\sim 8 \times 10^{15}$ cm^{-3} at 300K, and one in the conduction band with a concentration of $\sim 2 \times 10^{16}$ cm^{-3}. The former could originate from n-type Se vacancies, while the latter is most likely impurities from the Se source material.

Acknowledgements

Table of Contents

List of Figures

List of Tables

List of Commonly Used Abbreviations

IR	Infrared
SWIR	short -wave infrared
MWIR	mid-wave infrared
LWIR	long-wave infrared
VLWIR	very-long-wave infrared
FPA	focal plane array
TxState	Texas State University—San Marcos
ARL	U.S. Army Research
MBE	molecular beam epitaxy
UHV	ultra-high vacuum
BEP	beam equivalent pressure
BFM	beam flux monitor
AHC	atomic hydrogen cleaning
$\sim Se_6$	predominantly Se_6
$\sim Se_2$	predominantly Se_2
RHEED	reflection high energy electron diffraction
LRI	laser reflectance interferometry
XRD	x-ray diffraction
FWHM	full-width-half-maximum
XPS	x-ray photoelectron spectroscopy
AFM	atomic force microscopy
SEM	scanning electron microscopy
EDX	electron dispersive x-ray spectroscopy
FTIR	Fourier transform infrared spectroscopy
cPL	confocal photo-luminescence
SIMS	secondary ion mass spectrometry
PAS	positron annihilation spectroscopy

S	PAS shape factor
RBS	Rutherford back-scattering spectroscopy
EPD	etch pit density
VFH	variable-field Hall
QMSA	quantitative mobility spectrum analysis
MCF	multiple-carrier fit
V_{Hg}	mercury vacancy
V_{Se}	selenium vacancy
Hg_i	mercury interstitial
σ	conductivity
n	electron concentration
n_{int}	intrinsic electron concentration
μ	electron mobility
τ	excess carrier lifetime
e	elementary charge (1.602×10^{-19} Coulombs)
N_i	ionized impurity density
E_d	ionization energy
a_o	cubic lattice parameter
T	Temperature
k_B	Boltzmann's constant (8.617×10^{-5} eV/K)

1 Introduction

1.1 Infrared Sensor Applications

Most passive detection approaches for security and defense applications rely on radiation emitted by objects of interest. The thermal radiation emitted by most objects tends to fall in the infrared (IR) spectrum. IR wavelengths are divided into four categories based on transmission through the atmosphere over appreciable distances. Wavelengths of 1-3 μm are considered short-wave infrared (SWIR), 3-8 μm are mid-wave infrared (MWIR), 8-12 μm are long-wave infrared (LWIR), and IR wavelengths greater than 12 μm are very-long-wave infrared (VLWIR). Devices that can detect and form images from the thermal radiation emanating from both warm targets with high background irradiance (SWIR, MWIR) and cool targets with low background irradiance (LWIR, VLWIR) have many strategic and tactical applications. Different components in the atmosphere such as water and carbon dioxide will absorb certain IR wavelengths, creating "transmission" windows of IR wavelengths in the atmosphere shown in Figure 1-1. Thus IR sensors and imaging devices sensitive to the specific wavelengths that fall within atmospheric transmission windows need to be developed [1].

1.2 Infrared Materials

There are many types of IR detector systems, but most involve semiconductor materials. Charge carriers (electrons and holes) are generated in a semiconductor when it absorbs radiation greater than its energy bandgap, and so radiation in the desired IR spectrum can be detected by selecting a semiconductor material with a bandgap sensitive to that spectrum and forming certain device structures such as p-n junctions and focal plane arrays (FPAs). There are a number of different semiconductor materials that can be fabricated into IR devices, but certain properties of
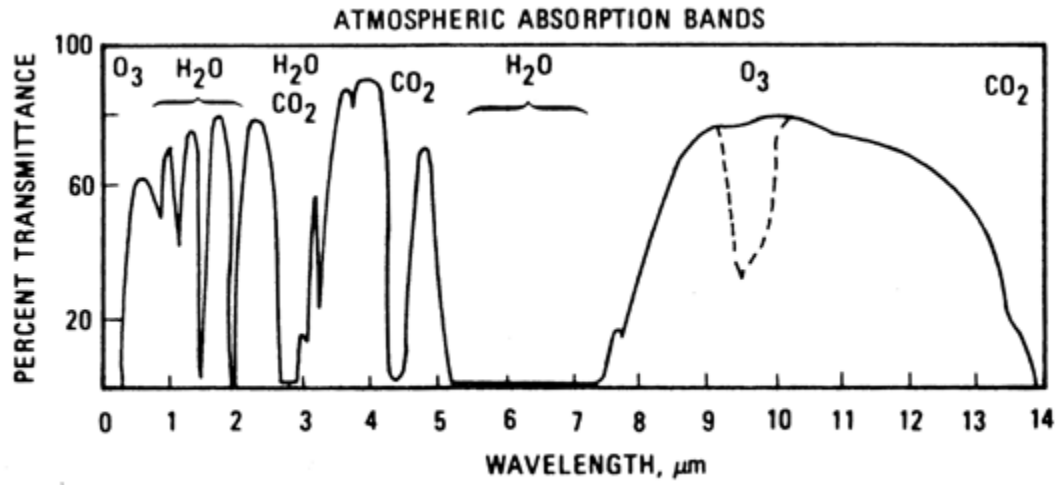
Figure 1-1: Transmittance of various IR wavelengths through the atmosphere, and the gases responsible for absorption. Taken from Reference [2].

Material	E_g (eV)		n_{int} (cm^{-3})		μ_e (x10^4 cm^{2}V^{-1}s^{-1})		μ_h (x10^4 cm^{2}V^{-1}s^{-1})	
	77K	**300K**	**77K**	**300K**	**77K**	**300K**	**77K**	**300K**
InAs	0.414	0.359	6.5×10^3	9.3×10^{14}	8	3	0.07	0.02
InSb	0.228	0.18	2.6×10^9	1.9×10^{16}	100	8	1	0.08
In$_{0.53}$Ga$_{0.47}$As	0.66	0.75	--	5.4×10^{11}	7	1.38	--	0.05
PbS	0.31	0.42	3×10^7	1.0×10^{15}	1.5	0.05	1.5	0.06
PbSe	0.17	0.28	6×10^{11}	2.0×10^{16}	3	0.10	3	0.1
PbTe	0.22	0.31	1.5×10^{10}	1.5×10^{16}	3	0.17	2	0.08
Pb$_{1-x}$Sn$_x$Te	0.1	0.1	3.0×10^{13}	2.0×10^{16}	3	0.12	2	0.08
Hg$_{1-x}$Cd$_x$Te	0.1	0.1	3.2×10^{13}	2.3×10^{16}	20	1	0.044	0.01

Table 1-1: Bandgap, intrinsic carrier concentration, and electron and hole mobility at 300K and 77K for various IR semiconductor materials [3].

these materials will affect their relative performance. Ideally, the material should have a low intrinsic carrier concentration (n_{int}), as this will allow greater control over the carrier concentration through doping. The charge carriers in material should have high mobilities (μ) and excess carrier lifetimes (τ) to maximize the diffusion length of the photo-generated carriers and thus the collection efficiency of the detector. Other properties that increase device performance are high optical absorption coefficients and low dielectric functions. Some commonly used IR materials and certain electrical properties are listed in Table 1-1.

1.3 Infrared Material of Choice—Mercury Cadmium Telluride

Currently, the material of choice for IR applications is mercury cadmium telluride ($Hg_{1-x}Cd_xTe$). $Hg_{1-x}Cd_xTe$ is an alloy of the semimetal mercury telluride (HgTe) and the semiconductor cadmium telluride (CdTe), both of which crystallize in the cubic zinc-blende structure. By adjusting the mole fraction of Cd (x-value) in $Hg_{1-x}Cd_xTe$, the cut-off wavelength can be tailored from 1 μm to 30 μm. This allows $Hg_{1-x}Cd_xTe$ to be used in sensor applications from the SWIR to the VLWIR.

Controlling the carrier concentration of $Hg_{1-x}Cd_xTe$ through doping is well understood. Due to the relatively weak Hg-Te bond, vacancies form on Hg sites (V_{Hg}) in the lattice during most growth processes. As a result, $Hg_{1-x}Cd_xTe$ tends to be vacancy-doped p-type unless heavily n-type doped to compensate. However, V_{Hg} can be filled by annealing under an Hg overpressure after growth. N-type $Hg_{1-x}Cd_xTe$ can be produced by adding donor impurities during growth, typically indium (In). Although V_{Hg} alone can produce a p-type concentration, it is generally preferred to add acceptor impurities—typically arsenic (As)—as this provides greater control over the p-type concentration as well as improved minority carrier lifetime [4]. Through Hg

annealing and the use of In and As doping, the carrier concentration of $Hg_{1-x}Cd_xTe$ can be controlled from the 10^{14} to $10^{18}\,cm^{-3}$ range and be either n-type or p-type.

While other IR materials such as InSb and InAs may have higher mobilities, their bandgaps are not tunable, and thus they are restricted to single cut-off wavelengths in the SWIR and MWIR regions. $Hg_{1-x}Cd_xTe$ currently has the highest electron mobility of any LWIR material. $Hg_{1-x}Cd_xTe$ charge carriers also have long lifetimes, and thus long diffusion lengths which improves the performance of $Hg_{1-x}Cd_xTe$ p-n junctions. At this time, no other material has a tunable cut-off wavelength in the IR spectrum with such favorable properties for IR sensor applications. $Hg_{1-x}Cd_xTe$ remains the gold standard by which other IR materials are measured, particularly for LWIR applications [3].

1.4   Infrared Detector Material Requirements

The material requirements for IR devices change as new IR devices are developed. One such device is an FPA, which consist of an array of IR detectors connected to a read-out integrated circuit (ROIC) that combines the signals from the IR detector elements to form images. As FPA structures have evolved, so too have the requirements for the IR materials used to fabricate them.

The first generation FPAs consisted of a linear array of detector elements, as shown in Figure 1-2 (a). A rotating mirror directed the image across the linear array, generating images at a video frame rate. These first generation FPAs, also referred to as scanning arrays, could be formed from bulk-grown ingots of PbS, PbSe, or $Hg_{1-x}Cd_xTe$. 1st generation scanning arrays gave way to 2nd generation staring arrays shown in Figure 1-2(b), in which the detector elements were arranged on a 2-dimenional grid. Each detector element forms a pixel in the image, and so the resolution of staring arrays can be improved by increasing the number of detector elements in the
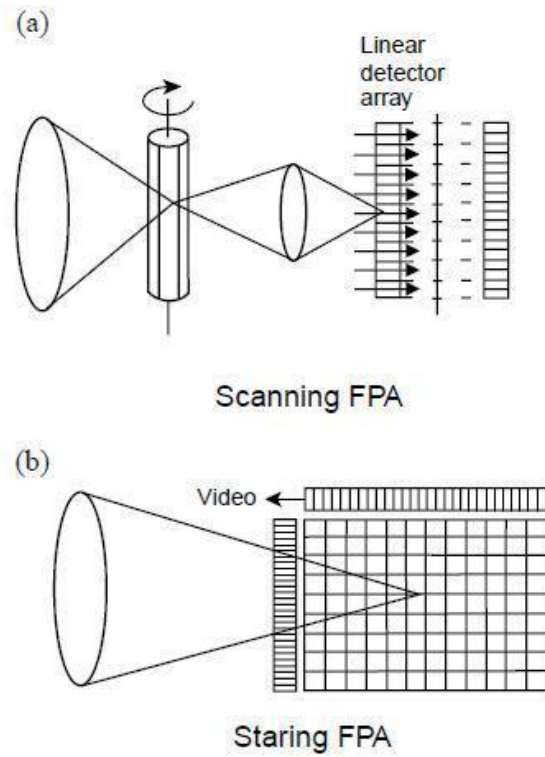
Figure 1-2: Diagram of (a) 1st generation scanning arrays and (b) 2nd generation staring arrays. Taken from Reference [5].

array. Since 2nd generation FPAs are two-dimensional, a greater number of FPAs can be fabricated from material produced with large cross-sectional areas, which is difficult for many bulk-grown IR materials such as $Hg_{1-x}Cd_xTe$. Thus 2nd generation FPAs required that materials such as $Hg_{1-x}Cd_xTe$ be grown epitaxially over a large area substrate.

Heteroepitaxy—epitaxial growth on a substrate of a different material—raises new concerns when selecting the IR material. If the lattice parameters of the sample (a_o) and the substrate (a_s) do not match up, defects will form in the crystal lattice of the epilayer called misfit dislocations as shown in Figure 1-3. Additionally, dislocations already present in the substrate will propagate into the epilayer during growth. Thus the IR material in 2nd generation FPAs must be epitaxially grown on lattice-matched substrates with low dislocation densities.

Bulk cadmium telluride (CdTe) was initially chosen as a substrate for $Hg_{1-x}Cd_xTe$ growth. CdTe serves as an adequate substrate for SWIR $Hg_{1-x}Cd_xTe$, but MWIR and LWIR $Hg_{1-x}Cd_xTe/CdTe$ layers have unacceptably large dislocation densities (~10^7 cm^{-2}) even though the lattice constants differ by less than 1%. Dislocation densities higher than 10^6 cm^{-2} have been found to limit the performance of LWIR $Hg_{1-x}Cd_xTe$ p-n junctions (and thus LWIR $Hg_{1-x}Cd_xTe$ FPAs), particularly at lower temperatures as shown in Figure 1-4 [6]. However, by alloying CdTe with zinc telluride (ZnTe) to form $Cd_{1-x}Zn_xTe$, the lattice constant of the bulk $Cd_{1-x}Zn_xTe$ substrates can be tuned to match MWIR or LWIR $Hg_{1-x}Cd_xTe$. Thus LWIR $Hg_{1-x}Cd_xTe$ can be produced with dislocation densities limited to that of the $Cd_{1-x}Zn_xTe$ substrate (~10^5 cm^{-2}), suitable for 2nd generation LWIR FPAs [3].

While 2nd generation IR FPAs are only sensitive in one spectral region, the 3rd generation of FPAs now under development must provide simultaneous detection in multiple spectral regions, This again creates new requirements for the IR material. Larger area substrates are desirable, as this will allow multiple arrays to be produced in the same growth run thus lowering

6
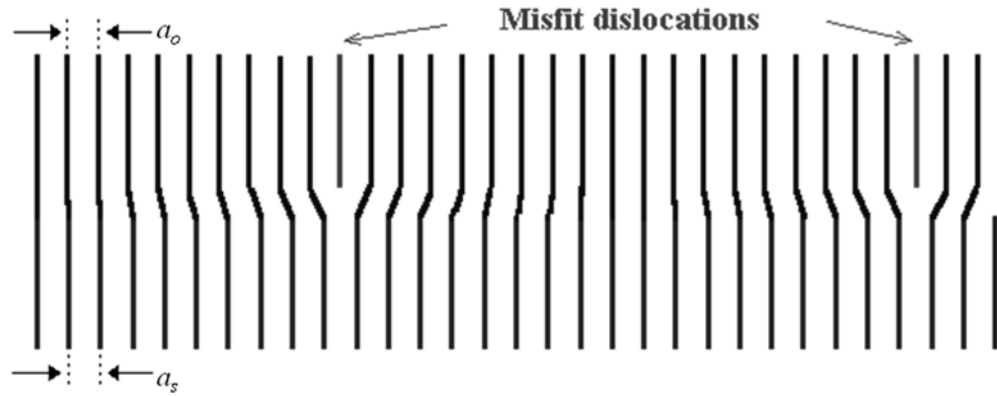
Figure 1-3: The formation of misfit dislocations as the lattice constant of the epilayer shifts from that of the substrate a_s to that of the material in equilibrium a_o. Taken from Reference [7]
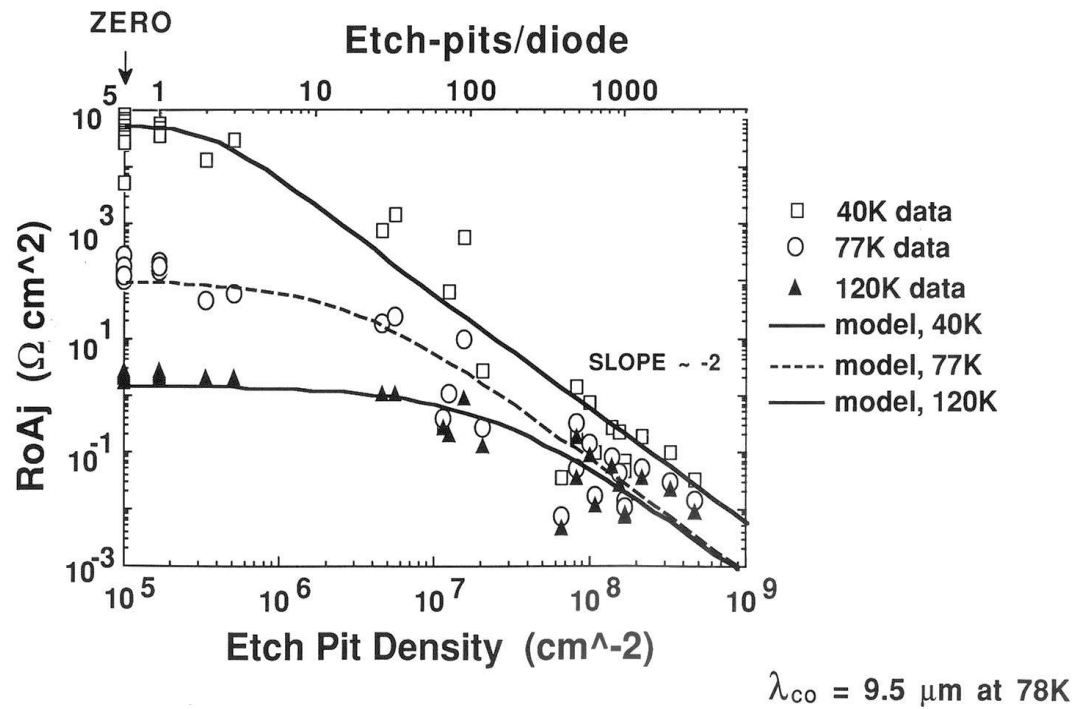
Figure 1-4: R_oA (diode figure of merit) for LWIR HgCdTe diodes versus dislocation density as measured by defect etching at different temperatures. Taken from Reference [6].

the cost. However, bulk $Cd_{1-x}Zn_xTe$ can only be produced with a maximum area of ~50 cm^2 so other scalable substrates for $Hg_{1-x}Cd_xTe$ had to be considered. InSb is lattice-matched to SWIR $Hg_{1-x}Cd_xTe$, but is hard to prepare as a bulk substrate. Other scalable substrates considered for $Hg_{1-x}Cd_xTe$ growth include highly lattice-mismatched sapphire (Al_2O_3), GaAs and Si.

Si is of particular interest, since the ROIC is also made of Si. One drawback to $Hg_{1-x}Cd_xTe/$ $Cd_{1-x}Zn_xTe$ FPAs is that the significant mismatch in the coefficient of thermal expansion (CTE) between the $Cd_{1-x}Zn_xTe$ substrate and the Si ROIC creates stress every time the FPA is cooled or warmed. This problem would obviously be eliminated if the both the substrate and ROIC were made of Si. Table 1-2 compares Si and $Cd_{1-x}Zn_xTe$ substrates for $Hg_{1-x}Cd_xTe$ FPA production, and Si is the preferred substrate in every respect except one: the 19% mismatch in lattice constant between Si and $Hg_{1-x}Cd_xTe$, which results in large densities of misfit dislocations. For this reason, Al_2O_3, GaAs, and Si are unsuitable as substrates for LWIR $Hg_{1-x}Cd_xTe$ growth. Various schemes have been attempted to alleviate this problem, such as using CdTe buffer layers on Si substrates. However, so far the best LWIR $Hg_{1-x}Cd_xTe$ grown on CdTe/Si still has dislocation densities ~10^6 cm^{-2} [8].

Twenty years of research into suitable substrates for LWIR $Hg_{1-x}Cd_xTe$ FPAs suggests that this could be an intractable problem. Additionally, $Hg_{1-x}Cd_xTe$ may not be a suitable material for multi-spectral arrays because the lattice constant varies along with the cut-off wavelength for different x-values. Small variations in lattice constant produce significant misfit dislocations in $Hg_{1-x}Cd_xTe$ layers, so growing $Hg_{1-x}Cd_xTe$ layers of different compositions on the same structure (such as SWIR $Hg_{1-x}Cd_xTe$ on top of LWIR $Hg_{1-x}Cd_xTe$) could create misfit dislocations which limit FPA performance [9]. Thus the development of 3rd generation LWIR FPAs may require an alternate IR material to $Hg_{1-x}Cd_xTe$.

	Substrate Technology		
	Bulk $Cd_{1-x}Zn_xTe$	**Si**	**Advantage**
Maximum Size	7 x 7 cm^2	6 in. diameter	Si
Maximum Area	~50 cm^2	~180 cm^2	Si
Scalability	No	Yes	Si
Cost	$220/cm^2	~$1/cm^2	Si
Thermal match to Si ROIC	No	Yes	Si
Robustness	Brittle	Hard	Si
Lattice match to $Hg_{1-x}Cd_xTe$	Yes	No	$Cd_{1-x}Zn_xTe$
Surface	Smooth	Smooth	None
Orientation Available	(112)	(112)	None
Vendors	1 (foreign	Numerous (domestic)	Si
Substrate Quality (dislocations)	<10000 cm^{-2}	<100 cm^{-2}	Si
Impurities	Low	Extremely Low	Si

Table 1-2: Comparison of Si and $Cd_{1-x}Zn_xTe$ substrates for $Hg_{1-x}Cd_xTe$ FPAs [8].

1.5 Statement of Problem

Alternative IR materials to $Hg_{1-x}Cd_xTe$ for IR FPAs, particularly LWIR FPAs, need to be investigated. A viable material would require a suitable large area substrate that is available for epitaxial growth. Specifically, the substrate must be scalable to large cross-sectional areas while being lattice-matched to the IR material to prevent misfit dislocations. This material should also be closely lattice-matched to other materials with different IR spectra to form multi-spectral FPAs. Ideally, the CTE of this substrate should be closely matched to the Si ROIC, and the properties of this material should lead to similar device performance as $Hg_{1-x}Cd_xTe$. Many such alternatives are being explored, such as ternary lead salt alloys, InSb, and indium gallium arsenide ($In_{1-x}Ga_xAs$). Additionally, new device structures such as strained layer superlattices (SLS) and quantum well infrared photodetectors (QWIPs) are being developed with various III-V materials that could serve as alternatives to $Hg_{1-x}Cd_xTe$ [3]. However, a relatively unexplored option that has recently come to be of interest is mercury cadmium selenide ($Hg_{1-x}Cd_xSe$).

The main advantage of $Hg_{1-x}Cd_xSe$ is that it belongs to a family of materials that all have lattice constants near 6.1 Å shown in Figure 1-5. This family also includes two III-V compounds that are commercially available as bulk wafers from commercial suppliers, namely GaSb and InAs. Bulk GaSb wafers have low dislocation densities ($\sim 10^4$ cm^{-2}), and since $Hg_{1-x}Cd_xSe$ and GaSb are nearly lattice-matched, this means that $Hg_{1-x}Cd_xSe$ layers could conceivably be grown on GaSb substrates with dislocation densities comparable to $Hg_{1-x}Cd_xTe$ layers grown on $Cd_{1-x}Zn_xTe$. GaSb wafers are available in up to 4 inches in diameter; larger wafers up to 6 inches in diameter are under development. Thus LWIR $Hg_{1-x}Cd_xSe$ could be grown on large area GaSb substrates with low dislocation densities suitable for the next generation of FPAs [10].

The other 6.1 Å materials provide additional opportunities for $Hg_{1-x}Cd_xSe$ development. There is still a small lattice-mismatch between GaSb and $Hg_{1-x}Cd_xSe$ that would still result in
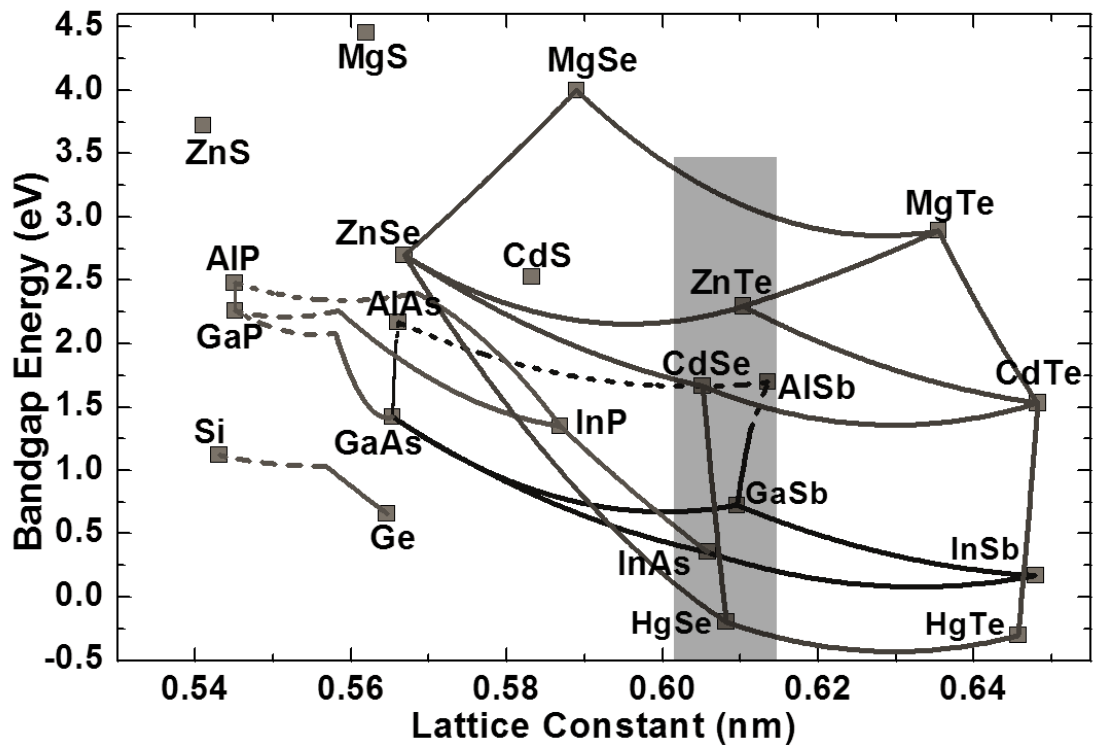
Figure 1-5: Bandgap vs. lattice constant for various materials, lattice constants near 6.1 Å highlighted. Taken from Reference [10].

misfit dislocations. This problem could be alleviated by using a buffer layer composed of $ZnTe_{1-x}Se_x$. $ZnTe_{1-x}Se_x$ is a ternary alloy with a lattice constant that can be tuned to match either GaSb or $Hg_{1-x}Cd_xSe$ by adjusting the ZnTe/ZnSe ratio. Additionally, a $ZnTe_{1-x}Se_x$ buffer layer would also provide II-VI surface for II-VI $Hg_{1-x}Cd_xSe$ deposition, eliminating the mixed-phase and doping concerns that arise from depositing a II-VI material on a III-V substrate [11].

Finally, it should be noted that the 6.1Å family of materials have bandgaps that range from zero to ~3 eV. Detectors fabricated from these materials could span the VLWIR to SWIR ($Hg_{1-x}Cd_xSe$), the visible (ZnTe and CdSe), and the ultraviolet ($MgSe_{1-x}Te_x$). At this point $Hg_{1-x}Cd_xSe$ research has been focused on developing it solely for IR applications. However, future research could be performed to integrate $Hg_{1-x}Cd_xSe$ with other 6.1 Å materials in a multi-junction platform, thus leading to multi-spectral device ranging from the ultraviolet to the VLWIR built on a single chip [10].

1.6 **Mercury Cadmium Selenide**

The properties of $Hg_{1-x}Cd_xSe$ and $Hg_{1-x}Cd_xTe$ are quite similar. Both are ternary alloys with binary end points consisting of a semimetal and a wide-gap semiconductor. The bandgaps of both alloys can be tuned across the IR spectrum as shown in Figure 1-6. However, one difference with $Hg_{1-x}Cd_xTe$ is that $Hg_{1-x}Cd_xSe$ is an alloy of two compounds which tend to crystallize in two different structures. HgSe crystallizes in the cubic zinc blende structure, as does HgTe and CdTe (and therefore $Hg_{1-x}Cd_xTe$). The cubic lattice parameter a_o of HgSe at room temperature has been measured as ranging from 6.085-6.088 Å. CdSe, on the other hand, tends to crystallize in the hexagonal wurtzite structure, both of which are shown in Figure 1-7. The hexagonal lattice parameters a and c of CdSe at room temperature have been measured as ranging from 4.299-4.309 Å and 7.009-7.024 Å for a and c respectively.
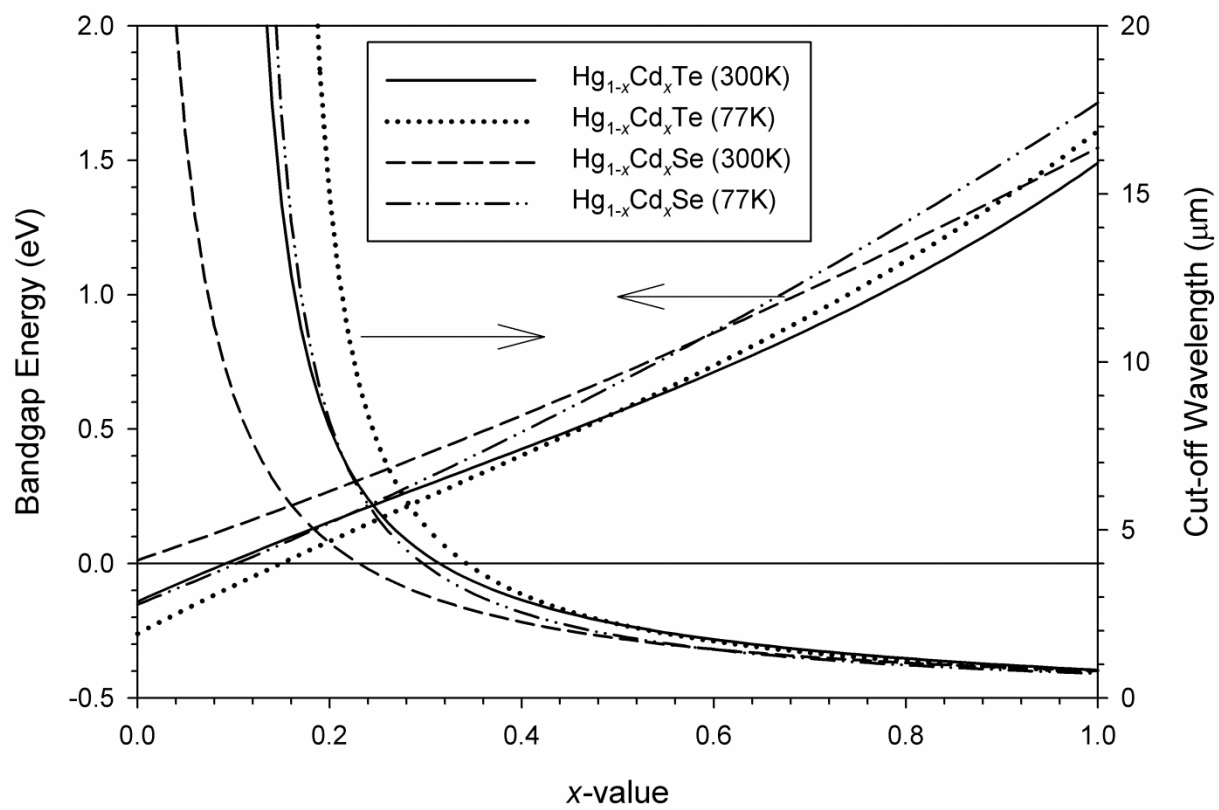
Figure 1-6: Variation of bandgap (Left Axis) and cut-off wavelength (Right Axis) for Hg$_{1-x}$Cd$_x$Te [3] and Hg$_{1-x}$Cd$_x$Se [12] with x-value.
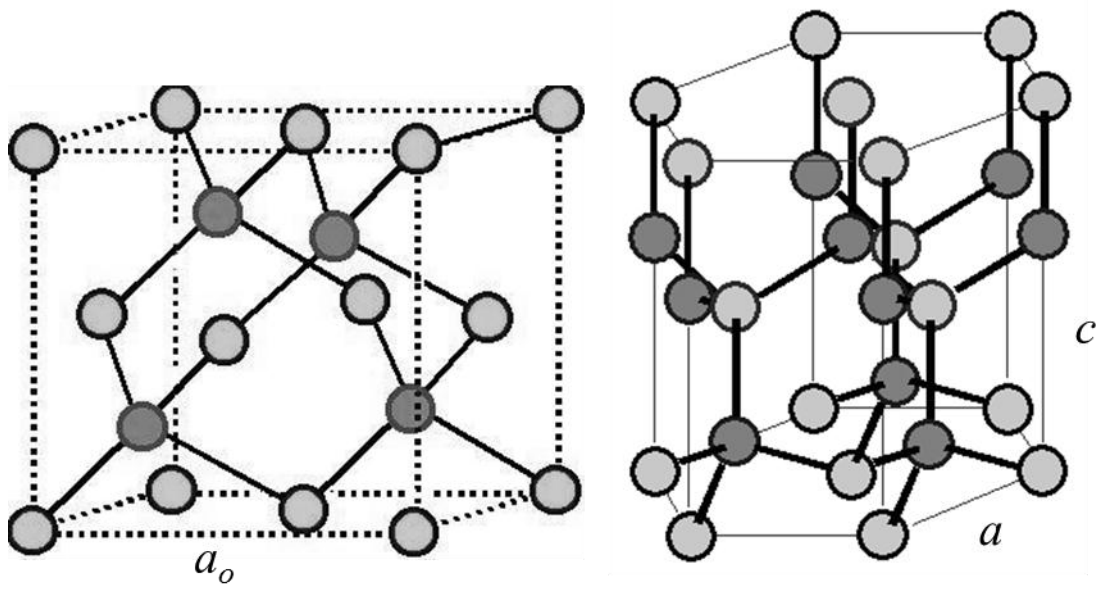
Figure 1-7: Diagram of the cubic zinc blende lattice (Left) and the hexagonal wurtzite lattice (Right). Taken from Reference [13].

Figure 1-8 gives the lattice parameters of bulk-grown $Hg_{1-x}Cd_xSe$ for different x-values. When grown as a bulk crystal (rather than a thin film), $Hg_{1-x}Cd_xSe$ will crystallize in the zinc-blende structure when $x<0.77$, and in the wurtzite structure for $x>0.81$. For $0.77<x<0.81$, the alloy is immiscible and does not form a single crystal structure. Fortunately, infrared applications (particularly LWIR) require x-values well below 0.77 where the crystal structure is zinc-blende [12]. A potential advantage of $Hg_{1-x}Cd_xSe$ over $Hg_{1-x}Cd_xTe$ is that for zinc-blende $Hg_{1-x}Cd_xSe$, a_o does not appear to vary significantly with x-value. Adjusting the composition of a ternary alloy changes the lattice parameter as well as the bandgap, and thus the lattice-mismatch between a LWIR $Hg_{1-x}Cd_xTe$ layer grown on top of a MWIR $Hg_{1-x}Cd_xTe$ layer can lead to misfit dislocations that limit device performance [9]. Since $Hg_{1-x}Cd_xSe$ has less variation in a_o with x-value than $Hg_{1-x}Cd_xTe$, multi-layer $Hg_{1-x}Cd_xSe$ structures will have less lattice-mismatch and thus may be better suited for multi-junction FPAs.

$Hg_{1-x}Cd_xSe$ samples have been grown as bulk crystals via the Bridgeman technique [12], and as thin films via molecular beam epitaxy (MBE) [14]. However, $Hg_{1-x}Cd_xSe$ was not pursued for IR applications because of the high background electron concentration observed in these early samples. As stated in Section 1.3, nominally undoped $Hg_{1-x}Cd_xTe$ tends to be p-type as-grown. By contrast, as-grown $Hg_{1-x}Cd_xSe$ appears to be n-type even when not intentionally doped. Typical electron concentrations for both bulk and thin film samples were between 10^{17} and 10^{18} cm^{-3}, with some samples containing concentrations as high as 10^{20} cm^{-3}. These high electron concentrations persisted at lower temperatures, showing little temperature variation below 100K [12], [14].

The electron concentration of $Hg_{1-x}Cd_xSe$ samples was increased by post-growth annealing under Hg, and reduced somewhat with vacuum and Se anneals for samples with lower x-values. This suggests that native defects could be contributing to the background electron
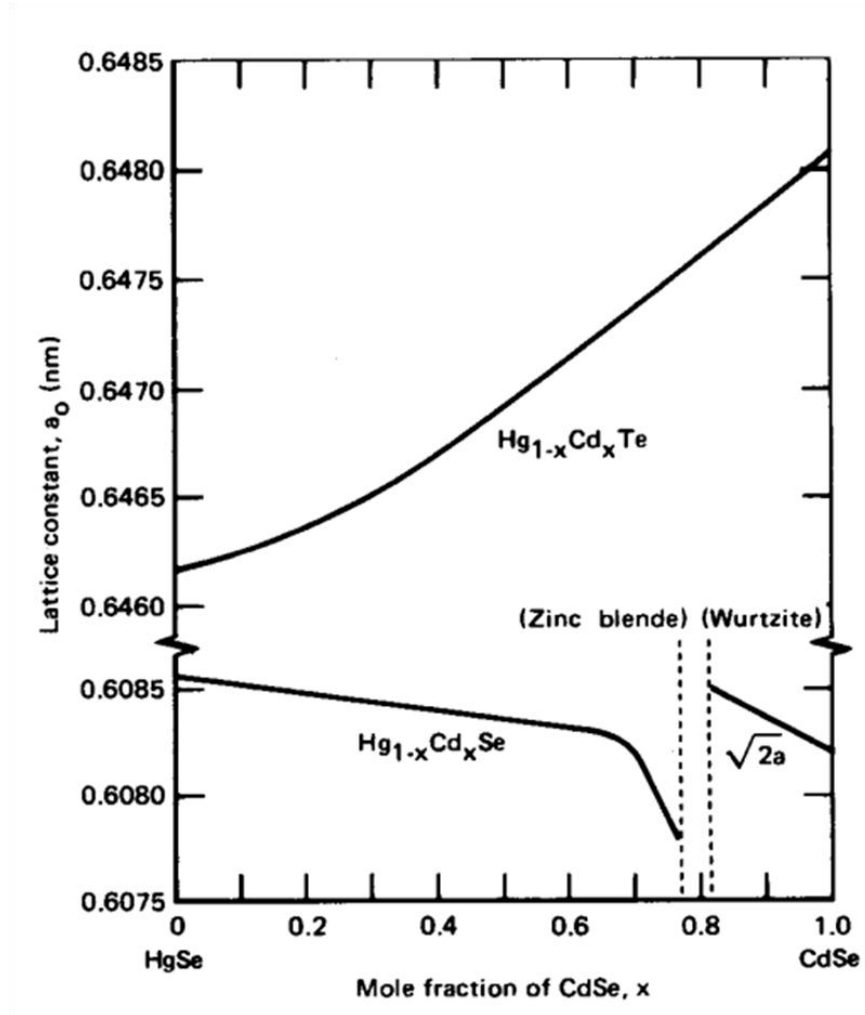
Figure 1-8: Lattice constant vs. *x*-value for bulk-grown Hg$_{1-x}$Cd$_x$Te and Hg$_{1-x}$Cd$_x$Se. For wurtzite Hg$_{1-x}$Cd$_x$Se, $\sqrt{2}a$ is given as this is directly comparable to the zinc-blende a_o. Taken from Reference [12].

concentration. Prior studies of the change in electron concentration and mobility after annealing HgSe samples suggested potential presence of p-type V_{Hg}, n-type Hg interstitials (Hg_i), and n-type Se vacancies (V_{Se}) [12]. Additionally, some electrons could be produced from unknown impurities introduced during sample growth. Before any $Hg_{1-x}Cd_xSe$ devices can be developed, the defects and impurities responsible for these high background electron concentrations must be identified and controlled.

1.7 **Technical Approach**

The ultimate objective of this study is to develop high quality $Hg_{1-x}Cd_xSe$ epitaxial layers on lattice-matched $ZnTe_{1-x}Se_x$/GaSb substrates. Research was performed as a collaborative effort between Texas State University—San Marcos, TX (TxState) and the U.S. Army Research Laboratory—Adelphi, MD (ARL). First, the preparation of GaSb substrates and the growth of $ZnTe_{1-x}Se_x$ buffer layers via molecular beam epitaxy (MBE) were investigated at TxState, in order to demonstrate that low dislocation density $ZnTe_{1-x}Se_x$/GaSb could be produced for $Hg_{1-x}Cd_xSe$ growth. The structural properties of these samples were evaluated using x-ray diffraction (XRD), x-ray photon spectroscopy (XPS), and atomic force microscopy (AFM).

While the $ZnTe_{1-x}Se_x$/GaSb substrate development was being investigated at TxState, the MBE growth of $Hg_{1-x}Cd_xSe$ was investigated at ARL on ZnTe/Si substrates. Si is significantly cheaper than GaSb, and unlike GaSb the preparation of Si for epitaxial growth has been well developed. Thus Si substrates were used as a cheaper alternative while the $ZnTe_{1-x}Se_x$/GaSb composite substrates were developed. A ZnTe buffer layer was used to alleviate the lattice mismatch between $Hg_{1-x}Cd_xSe$ and Si, much like a CdTe buffer layer is used for $Hg_{1-x}Cd_xTe$ growth on Si. These ZnTe/Si substrates were developed and supplied by ARL [15]. Of particular

interest were growth techniques and post-growth anneals that could reduce the large background electron concentration of $Hg_{1-x}Cd_xSe$.

$Hg_{1-x}Cd_xSe$ samples were characterized using Hall measurements, Fourier transmission infrared spectroscopy (FTIR), Nomarski microscopy, scanning electron microscopy (SEM), energy dispersive x-ray spectroscopy (EDX), AFM, and XRD. Various techniques were employed to try and determine what defects are present in $Hg_{1-x}Cd_xSe$, such as secondary ion mass spectrometry (SIMS), Rutherford backscattering spectroscopy (RBS), and positron annihilation spectroscopy (PAS). The first two were performed by the Charles Evans Analytical Group, the last one was performed as a collaboration with Washington State University—Pullman, Wa. Additionally, a suitable defect etch for etch pit density (EPD) measurements was explored. The results of this research will be presented in this dissertation.

2   Molecular Beam Epitaxy

2.1   Overview

MBE is a crystal growth technique in which a series of thermal beams of different molecules and atoms are directed at a heated substrate in an ultrahigh vacuum (UHV) chamber. Due to the heated surface of the substrate, the atoms and molecules adsorbed from the beams will migrate across the surface of the growing layer before bonding with it, thus crystallizing into a smooth epitaxial film under the proper conditions, while some atoms will desorb from the surface before bonding. The uniformity and quality of the epitaxial layer depends on several parameters such as substrate temperature and the flux of the thermal beams. The uniformity of the epitaxial layer can be further increased by rotating the substrate during growth.

MBE provides a great deal of control over the composition structure of the epitaxial layer. The composition of the epitaxial film is determined by the arrival rates of the constituent materials and their evaporation rates from the substrate. Molecular beams are generated by heating the material in a cell to the point where a portion vaporizes, and then directing that vapor through a small aperture in the cell to form a beam aimed at the substrate. Increasing the temperature of the source material will increase the pressure of the molecular beam, and so the arrival rate of the constituent material can be controlled by the temperature of the source material.

By adding a shutter that can suddenly interrupt the beam, the molecular beam can be "turned on and off." Other sources also contain a programmable needle valve, which allows for rapid flux control by adjusting the aperture of the cell. Thus by controlling the relative pressures of the beams through the temperatures of the source material and the apertures of the cells, and

turning the beams on and off through the use of shutters, the thickness and composition of epitaxial layers through MBE can be controlled down to atomic dimensions [7].

2.2 **Equipment**

MBE of $ZnTe_{1-x}Se_x$ was performed at TxState, while MBE of $Hg_{1-x}Cd_xSe$ was performed at the ARL. Both facilities used similar MBE growth chambers purchased from DCA Instruments connected to UHV buffer lines that allow samples to be transferred *in situ* to other chambers as shown in Figure 2-1. These systems can accommodate wafers up to 3 inches in diameter. However, while only the II-VI growth chamber was used at ARL, multiple chambers on the UHV buffer line were used at TxState shown in Figure 2-2. In addition to the $ZnTe_{1-x}Se_x$ growth chamber, the TxState buffer line also included an atomic hydrogen cleaning station, systems for in-situ x-ray photoelectron spectroscopy and atomic force microscopy measurements, and a separate growth chamber dedicated to Sb-compounds that were used in this research.

2.2.1 **II-VI Deposition Chamber**

Both TxState and ARL used similar chambers purchased from DCA instruments shown in Figure 2-3 for the MBE growth of II-VI material. The II-VI chamber at TxState was used only for the growth of ZnTe and $ZnTe_{1-x}Se_x$, while the II-VI chamber at ARL was used to grow $Hg_{1-x}Cd_xSe$ and $Hg_{1-x}Cd_xTe$. The chambers were cylindrical with the various cells located at the bottom of the chamber, directing the molecular beams upwards towards the target substrate. The manipulator could adjust the position of the substrates in three dimensions, placing them in the path of the molecular beams. The manipulator also heated the substrates to the desired temperature and rotated the substrates during growth to enhance surface migration during growth

II-VI Growth Chamber

UHV Buffer Line

Gate Valve

Ports for additional chamber

Transfer arm

Load-lock
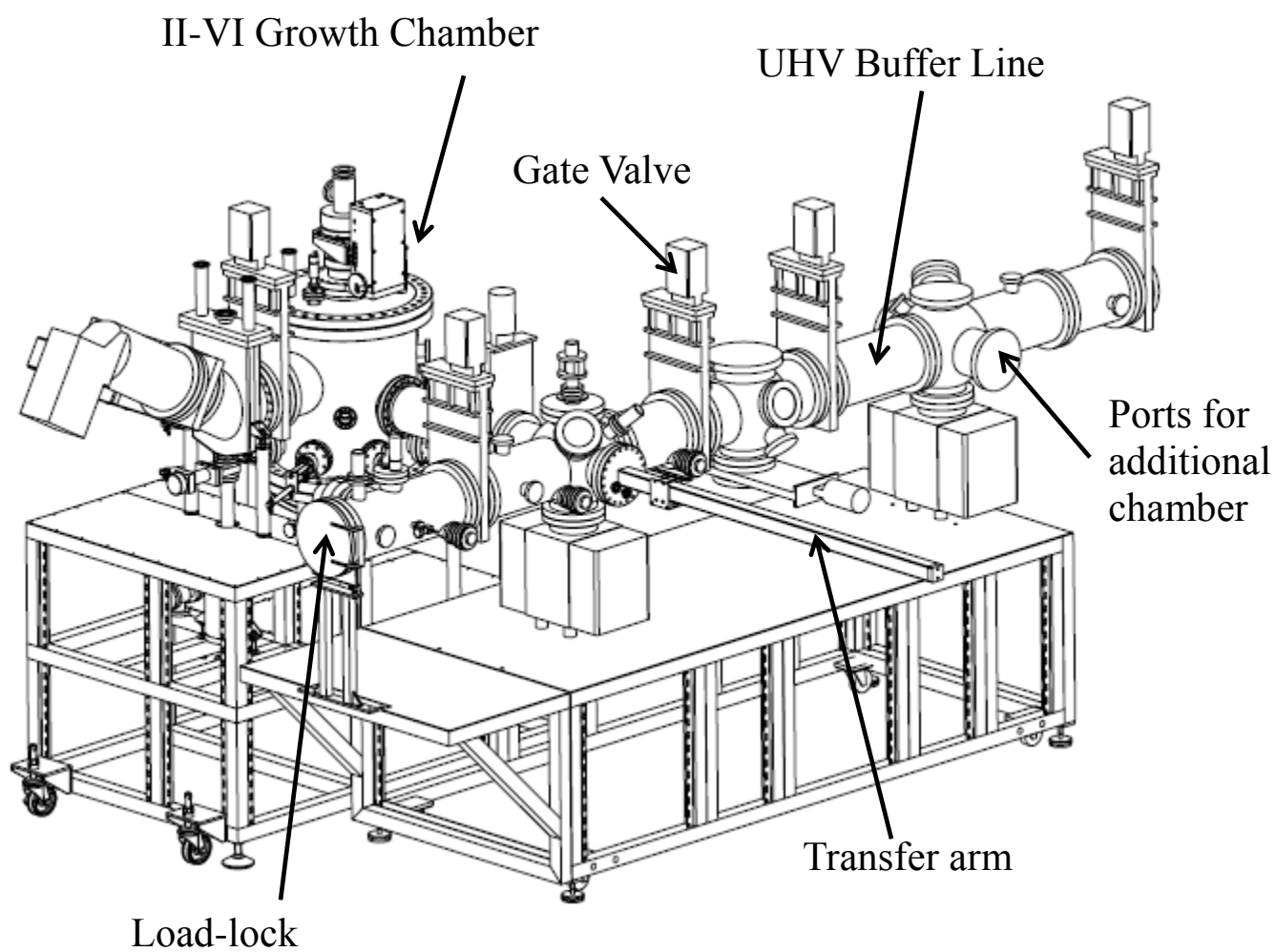
Figure 2-1: Diagram of the DCA Instruments growth chamber and UHV buffer line system used at TxState and ARL.

II-VI * **Chamber**   **Oxide I Chamber**   **Oxide II Chamber**   **As Chamber**   **GaSb *** **Chamber**

H *

Leadsalt Chamber   **XPS ***   **SPM ***   **Oxide III Chamber**
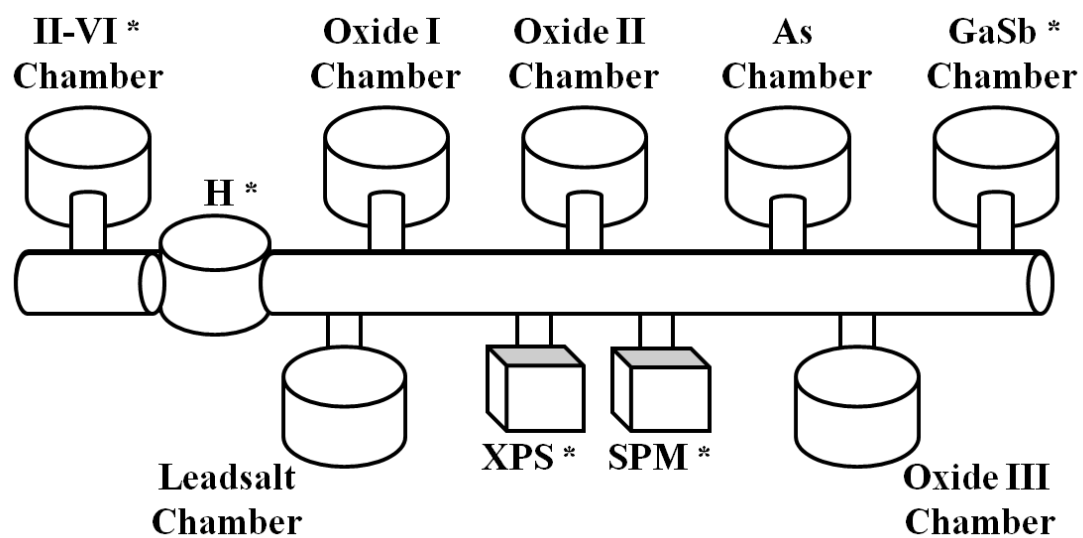
Figure 2-2: Diagram of the different chambers on the TxState buffer line. Chambers used in this research indicated by *.
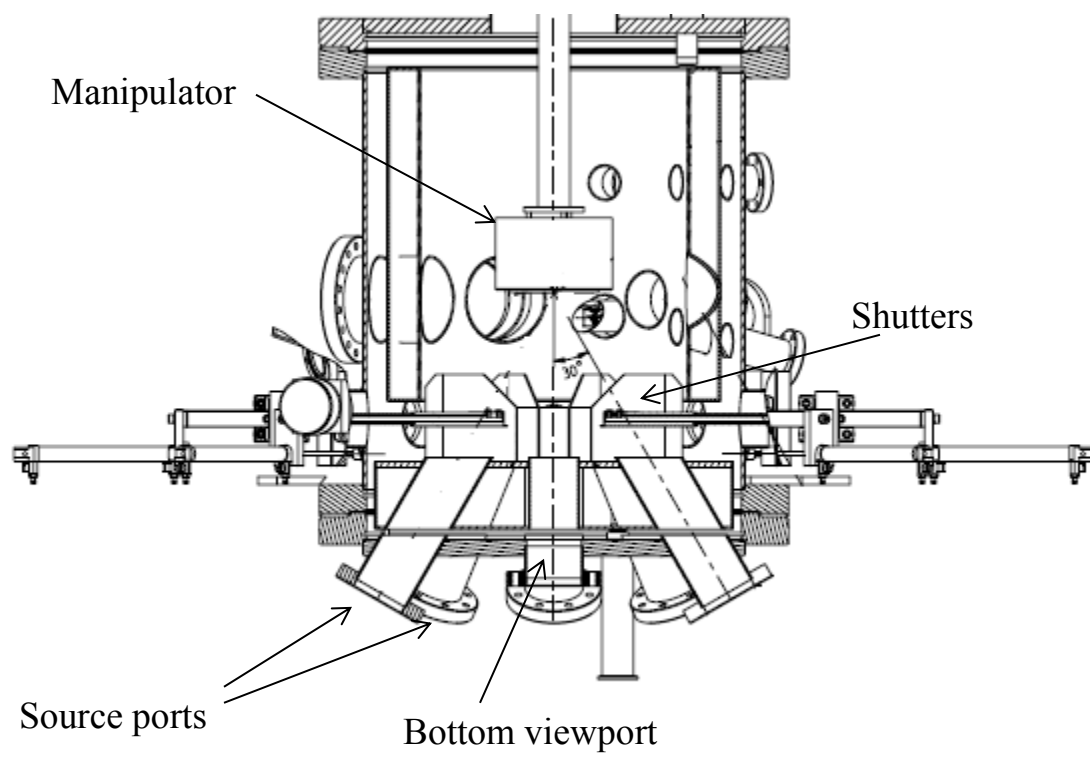
Figure 2-3: Diagram of the II-VI MBE deposition chamber.

and thus promote sample uniformity.

UHV was maintained in the deposition chamber with a cryopump. Additionally, the chamber includes a liquid nitrogen shroud to trap particles of excess high vapor pressure materials along the chamber walls, and a cold trap was used in the ARL chamber to capture stray Hg. The liquid nitrogen shroud also kept the sources thermally isolated, so that each could be independently controlled. Overall these systems maintain a system pressure in the mid-10^{10} to low-10^{-9} Torr range. In addition to the sources, the chambers included a phosphor screen and an electron gun directed at the substrate so that growths can be monitored via reflection high energy electron diffraction (RHEED) as described in Section 3.1. At the bottom of the chamber was a viewport aligned with the substrate that was used for pyrometry measurements on the ARL chamber and laser reflectance interferometry (LRI) at TxState, as described in Section 3.3.

The substrate temperature was controlled via a thermocouple and a Eurotherm feedback control system. Since the thermocouple cannot be placed directly on the substrate the thermocouple reading is not a direct measure of the substrate temperature. An Ircon Modline 3 pyrometer was used to determine the temperature based on the thermal radiation from the silicon substrate. However, this method is not as accurate at the relatively low growth temperatures of Hg_{1-x} $Cd_x Se$, and becomes less accurate as the growth progresses since the Hg_{1-x} $Cd_x Se$ film absorbs IR radiation. Thus the pyrometer can only provide an estimate of the substrate temperature used during growth.

The relative fluxes of the different sources were measured with a beam flux monitor (BFM). The BFM consisted of a nude ion gauge that could be moved into and out of the path of the molecular beams. Prior to growth, the beam equivalent pressure (BEP) for each source at the set temperature and/or valve position was determined by measuring the difference in the BFM pressure reading when the source was on (shutter/valve open) and the background reading

24

(shutter/valve closed).

2.2.2   Sources

2.2.2.1   Effusion Cells

With few exceptions, the molecular beams were generated with standard effusion cells, such as shown in Figure 2-4.The temperature of the cell was monitored with a thermocouple, and stabilized using a feedback loop. A cell at temperature T containing an aperture of area A, a distance l from the substrate will produce a flux of molecules or atoms striking a unit area of the substrate per second given by

$$J = (1.118 \times 10^{22}) \frac{pA}{l^2 \sqrt{MT}} \, molecules \Big/ cm^2 s \qquad \text{(2-1)}$$

where T is in Kelvin, p is the source pressure in cell in Torr, M is the molecular mass of the source material, and l and A are in cm and cm^2 respectively [7]. Usually A and l, are fixed by the design of the cell and the chamber, and M is an intrinsic property of the source material. Thus the flux is usually controlled by adjusting T, which also adjusts p according to the material's vapor pressure. Vapor pressure vs. T for various materials is given in Figure 2-5. Some cells also include an adjustable needle valve that allows the flux to be controlled by adjusting A as well as T.

The temperatures of all cells were monitored by thermocouples (either Type C or K), and the temperatures were stabilized within 1 °C with feedback control systems from Eurotherm. Cadmium and tellurium were supplied by effusion cells made by Applied EPI with capacities of up to 400 g of gallium. Mercury was supplied by a 600 cc effusion cell from Applied EPI, which contained an adjustable valve. Initially 5N selenium from Alfa Aesar was supplied with a Model VSb110 effusion cell made by ADDON also with adjustable valve. This Se source was later
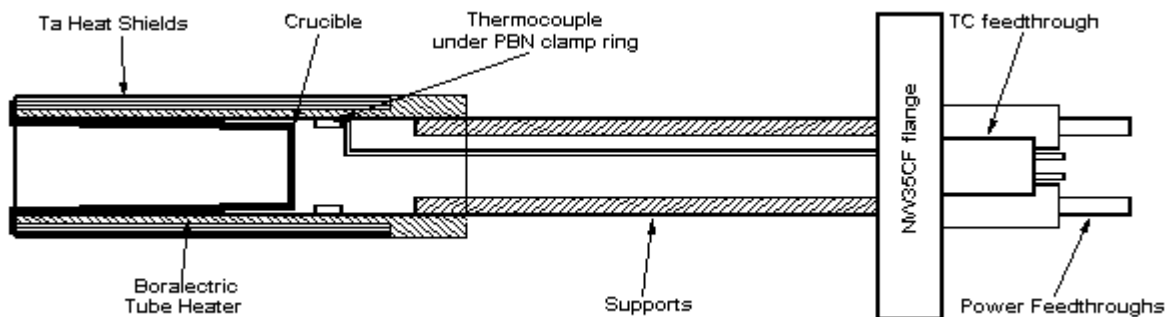
Figure 2-4: Diagram of a large capacity effusion cell. Taken from Reference [16].
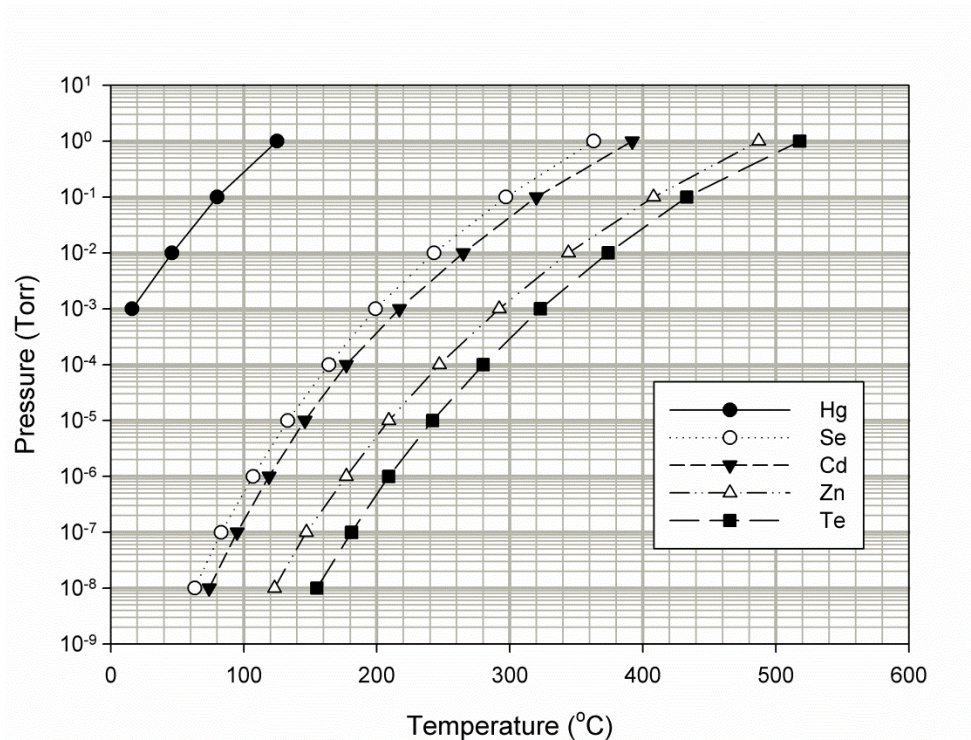
Figure 2-5: Vapor pressure vs. temperature for certain elements [17].

replaced with a disassociation source cracker.

2.2.2.2   Disassociation Source

Some materials do not form a monatomic flux upon sublimation, but instead consist of several polyatomic species. For some of these materials, the incorporation of these atoms into a growing layer can be improved by using a disassociation cell (cracker). A cracker directs the flux through a high temperature zone step to break apart (crack) the larger polyatomic species into simpler species [7]. Crackers were used for two materials in this research—hydrogen, and selenium (Se).

Hydrogen commonly forms H_2. A thermal hydrogen cracker, shown in Figure 2-6, was employed in order to investigate the use of atomic hydrogen (H) in preparing GaSb substrates. The hydrogen cracker, supplied by Veeco Instruments, used a tungsten filament heated to 2000 °C which catalytically cracked roughly 6% of the H_2 into H [18]. A Mark V Valved Se Cracker also made by Veeco, shown in Figure 2-7, was used to supply selenium for $ZnTe_{1-x}Se_x$ at TxState, and then later this source replaced the Se effusion cell used for $Hg_{1-x}Cd_xSe$ growth at ARL. Selenium vapor forms a mix of several atomic species, ranging from Se_2 to Se_8, as shown in Figure 2-8. The relative concentration of the different Se species depends on the temperature of the beam. For temperatures below ~650 K, the predominant species is Se_6 (~Se_6). As the temperature is increased, the predominant species transitions from Se_6 to Se_5 at ~650 K and then from Se_5 to Se_2 at ~900 K [19].

It was thought that using a cracker source to produce a predominantly Se_2 (~Se_2) flux would lead to better incorporation of Se in the $Hg_{1-x}Cd_xSe$ growths, and the Se effusion cell was replaced with the Se cracker to test this. A mass spectrometer that could measure the relative concentrations of the Se atomic species was unavailable. However, it was suggested that the

Figure 2-6: Picture of the standard atomic hydrogen source from Veeco Instruments. Taken from Reference [20].
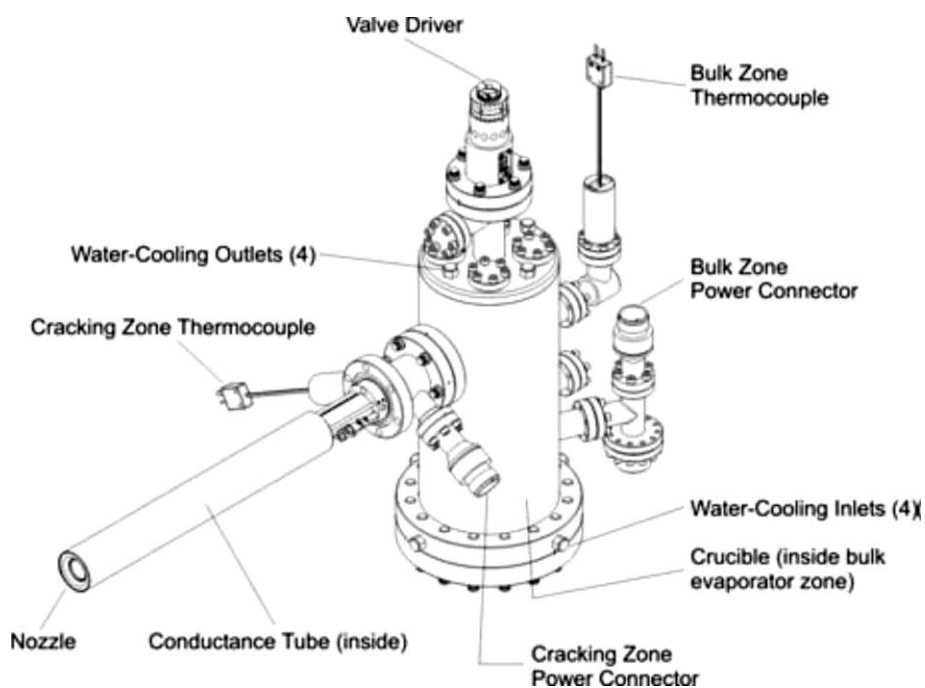
Figure 2-7: Diagram of the Mark V 500 CC Selenium Valved Cracker, made by VEECO. Taken from Reference [21].
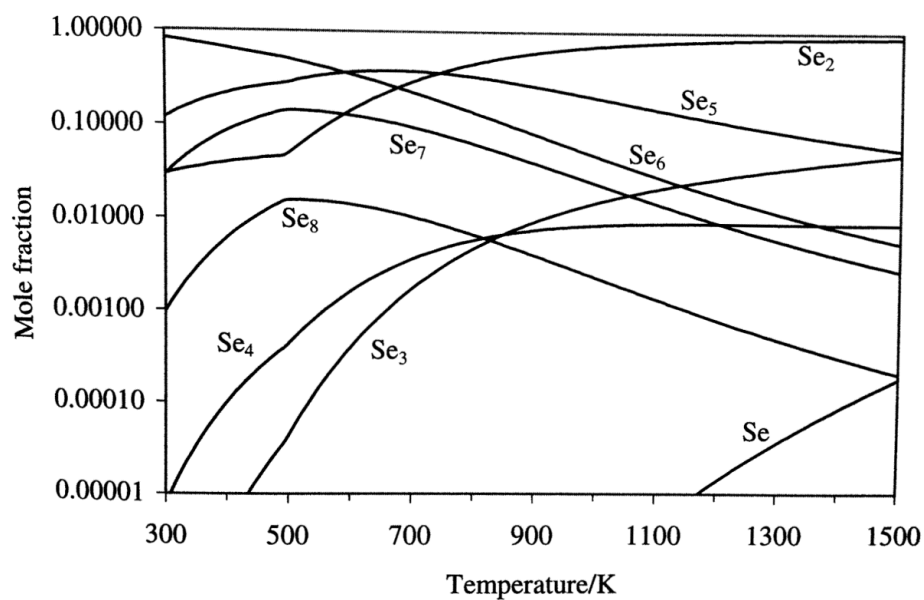
Figure 2-8: Mole fraction of Se polyatomic species in Se vapor vs. temperature. Taken from Reference [19].
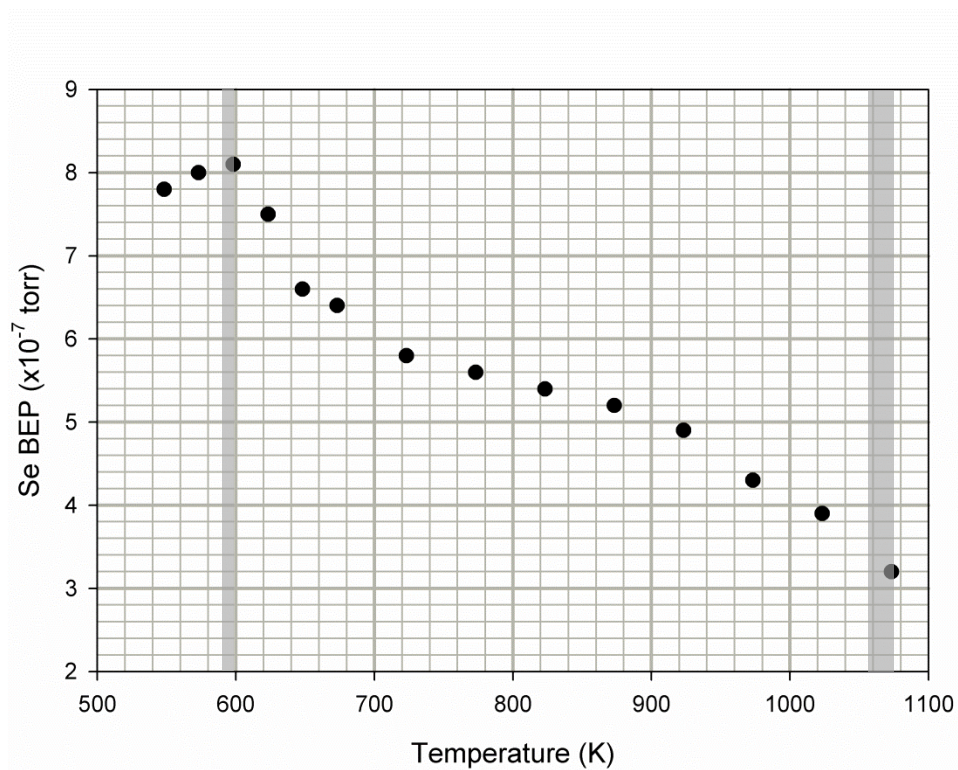
Figure 2-9: BEP measured from Se cracker for different cracking zone temperatures, with Se reservoir temperature fixed at 250 °C and valve position kept at 150 mils. Shaded regions represent the typical operating temperatures for the effusion cell (~600 K) and the Se cracker when producing a predominantly Se_2 flux (~1070 K).

different species of Se would have different ionization efficiencies, which would affect the BEP measured by the BFM. To determine the cracking zone temperatures required to crack the Se beam, Se BEP was measured as a function of the cracking zone temperature while the Se reservoir temperature and valve position were fixed at 250 °C and 150 mils respectively.

These measurements, given in Figure 2-9, show that as the cracking zone temperature increased the measured BEP changed due to the different sensitivities to the Se species. Two transition regions appear to occur at ~350 °C (600 K) and ~650 °C (920 K), which correspond with the expected transitions from ~Se_6 to ~Se_5 at ~650 K and from ~Se_5 to ~Se_2 at 900 K [19]. The Se BEP signal for the flux at the typical operating temperature for the cracker (800 °C) was found to be lower than the effusion cell temperature (325 °C) by factor of 2-3, and so an approximate correction factor of two was applied to the measured ~Se_2 fluxes.

2.2.2.3   Source Material

The purity of the source material used in MBE is of key importance for the $Hg_{1-x}Cd_xSe$ growth since one possible source of background electrons could be impurities introduced from contaminated source material. The mercury used during growth was supplied by Bethlehem Apparatus Co. This mercury was quadruple-distilled and had a stated purity of 99.9995%. Prior to growth, the substrates were annealed under a Te overpressure. However, it is unlikely that impurities were introduced from the Hg or Te source material. Both of these sources were also used to grow $Hg_{1-x}Cd_xTe$ samples in the same chamber as the $Hg_{1-x}Cd_xSe$ samples, and no background impurity problems were observed in the $Hg_{1-x}Cd_xTe$.

The material loaded in the Se and Cd sources are of bigger concern. Cd was supplied by Alfa Aesar and had a purity of 99.999% (5N). An analysis of the Cd source material indicated small concentrations of chlorine, silicon, and other materials that could potentially alter the

electrical properties of the samples. The Se material loaded into the effusion cell used for the initial $Hg_{1-x}Cd_xSe$ growth was also supplied by Alfa Aesar with 5N purity. In contrast, the Se loaded into the cracker consisted of a mix of material from two different companies, both of which were rated 6N or higher purity.

3　Characterization Techniques

3.1　Reflection High Energy Electron Diffraction

One advantage of MBE over other growth techniques is that since the growth is performed in ultra-high vacuum, the crystal quality can be monitored during growth through various techniques such as RHEED. A beam of energetic electrons strikes the sample surface at a grazing angle (1-2°), and the electrons are then diffracted on to a phosphor screen on the other side of the chamber. The sample surface acts as a diffraction grating, producing a diffraction pattern on the phosphor screen which is recorded by a camera. Due to the beam's small angle of incidence the electrons only interact with the top few monolayers of the sample, making this a technique surface sensitive. The diffraction pattern observed depends on the crystal lattice and orientation, surface morphology, and surface reconstructions.

A sample that is amorphous will not exhibit a pattern, instead displaying a featureless haze. Surface oxide layers are often amorphous, and so samples often appear hazy when first loaded and do not form a clear pattern until the oxides have been desorbed. Samples that are poly-crystalline rather than single-crystal will exhibit a pattern of concentric rings. A RHEED pattern consisting of evenly spaced spots (a "spotty" pattern) indicates that the sample has a single crystal structure, but has a rough, 3-dimensional surface. Smoother, more 2-dimensional surfaces will produce a "streaky" pattern, consisting of long uniform streaks. If the electron beam strikes a perfectly smooth surface, than it will produce a pattern consisting of a single ring of spots that corresponds to a perfect diffraction pattern [7]. Thus the ideal pattern is a single ring of spots, which indicates that that the surface of the sample is atomically smooth.

3.2 X-ray Photoelectron Spectroscopy

X-ray photoelectron spectroscopy (XPS) is a useful technique for determining the chemical composition of sample surfaces. The photoelectric effect demonstrated that all electrons bound to an atomic nucleus have a specific binding energy (*BE*), and that if the electron absorbs a photon with a higher energy than the binding energy the electron will be released. In XPS, a beam of x-rays with energy *hv* is directed at the surface of the sample, releasing electrons from the surface atoms with a certain kinetic energy (*KE*) that is measured by a spectrometer. The measured *KE* is given by

$$KE = h\nu - BE - \phi_s \tag{3-1}$$

where ϕ_s is the work function of the spectrometer. The binding energies of the released electrons is determined by measuring *KE* for a given *hv* and ϕ_s. Since these binding energies are specific to the atomic energy levels of the surface atoms, the identity and relative concentrations of the different surface atoms is determined by comparing the intensity of the measured signal for different values of BE [22].

XPS measurements were performed at TxState in a UHV chamber connected to the UHV buffer line. A monochromatic Mg K$_\alpha$ x-ray source from Specs was used to generate the x-rays (*hv* = 1253.6 eV), and the electrons were measured by a 300-mm-radius concentric hemispherical analyzer from VG Scienta SES-2002 [23].

3.3 Laser Reflectance Interferometry

Laser reflectance interferometry (LRI) is a useful technique for measuring the growth rate of a sample as it is being grown in real time. By measuring the growth rate of a sample as it is being grown, the effect of a parameter on the growth rate can be measured during a single

growth run, thus saving time and substrates. A laser is mounted on a viewport on the MBE system, and aligned so that the beam hits the sample at angle θ and is reflected off of the surface into a photodiode mounted on another viewport. If the wavelength λ of the laser is lower than the cut-off wavelength of the sample being grown, then the beam will be transmitted through the sample and reflected off of the substrate surface as well as the sample surface. Thus the reflected beams will interfere, with constructive interference occurring when

$$m\lambda = 2nd\cos(\theta) \tag{3-2}$$

where and n and d are the refractive index and thickness of the sample respectively, and m is an integer. As the growth progresses, d will increase, causing the reflected signal to cycle through the maxima and minima conditions with time. Each cycle corresponds to an increase in thickness given by

$$\Delta d = \frac{\lambda}{2n\cos(\theta)} \tag{3-3}$$

and so the growth rate can be determined by dividing Δd by the period of the cycle.

LRI measurements were used at TxState to measure the growth rate of ZnTe samples on GaSb and GaAs substrates. A 5mW, 639 nm laser from Newport was modulated by an Avtech pulse generator, and the reflected signal was measured by a Si photodiode from Thorlabs connected to a Keithley AC voltmeter. Both the laser and the photodiode were mounted on a viewport located at the bottom of the chamber directed up at the substrate, making θ effectively 0°. The refractive index of ZnTe is 2.72, and thus $\Delta d \approx 105$ nm for this system. Since this technique requires a laser wavelength lower than the cut-off wavelength of the sample, this technique could not be used for LWIR $Hg_{1-x}Cd_xSe$.

3.4 Nomarski Microscopy

Differential interference contrast microscopy, also called Nomarski microscopy after its inventor, is a technique for obtaining detailed images of three dimensional sample surfaces. A beam of polarized, monochromatic light is directed into a half-mirror and reflected into a Nomarski prism, consisting of two birefringent crystal wedges sealed together at the hypotenuse. The Nomarski prism produces two beams orthogonally polarized to one another, directed so that after passing through the condenser they encounter the sample surface roughly 0.2 µm apart (this offset of the two beams is called the shear).

The two beams are then reflected by the sample, with no interference at this point due to the orthogonal polarizations. However, different elevations or other inhomogeneous features on the sample surface will produce different optical path lengths and therefore phase differences in the two beams. This creates interference when the reflected beams pass through the Nomarski prism and recombine. Thus sudden changes in elevation on the sample surface (such as pits, hillocks, or other defects) will produce a sharp contrast in the resulting image [24]. Nomarski microscopy was performed with a Leica INM 20 Microscope, with images processed using D.E. Analysis, an optical processing program. The shear and light intensity was adjusted on the LEICA to produce the sharpest contrast, and the exposure time and white balance adjusted by D.E. Analysis to produce the clearest image.

3.5 Scanning Electron Microscopy

To obtain higher resolution images of the sample surface, Scanning Electron Microscopy (SEM) was also employed. SEM focuses a beam of electrons onto the sample surface. Inelastic scattering between the incident electrons and the surface atoms produces low energy secondary electrons, which are detected via a scintillator-photomultiplier system known as an Everhart-

Thornley detector. Changes in the topography of the surface will change the active area emitting secondary electrons, and thus the signal detected. By scanning over the sample with the beam in a raster pattern, an image of the surface morphology can be produced with a resolution as far greater than any optical microscopy technique.

SEM measurements must be performed in an ultra-high vacuum to prevent the incident electron beam from dispersing. For non-conducting samples, SEM can produce a build-up of excess electrons on the sample surface, known as charging the surface [25]. This was observed when higher voltages were used to produce the electron beam. A voltage of 10 kV was found to be sufficient for producing images without charging. Samples were mounted with carbon tape and measured with a CamScan Maxim 2040 Scanning Electron Microscope.

The SEM system was also used to determine stoichiometry of certain $Hg_{1-x}Cd_xSe$ samples using energy-dispersive x-ray spectroscopy (EDX), to compare with FTIR. The electron beam generated by the SEM excites electrons in the sample atoms, creating holes in the electron shells bound to the nuclei. Electrons in higher energy levels will drop down to fill these holes, emitting x-rays with specific wavelengths that correspond to the energy levels of that particular atomic species. Thus by measuring wavelengths of the x-rays emitted when the sample is excited by the electron beam, the stoichiometry of the sample can be determined by comparing the relative signal strength at the particular wavelengths corresponding to each element [26]. Figure 3-1 shows the EDX spectrum measured from a typical $Hg_{1-x}Cd_xSe$ sample.

3.6 Fourier Transform Infrared Spectroscopy

Another technique used to determine sample composition is Fourier transform infrared spectroscopy (FTIR), which measures the absorption of IR radiation by a sample as a function of wavelength. This is accomplished by directing a polychromatic IR beam through a Michelson
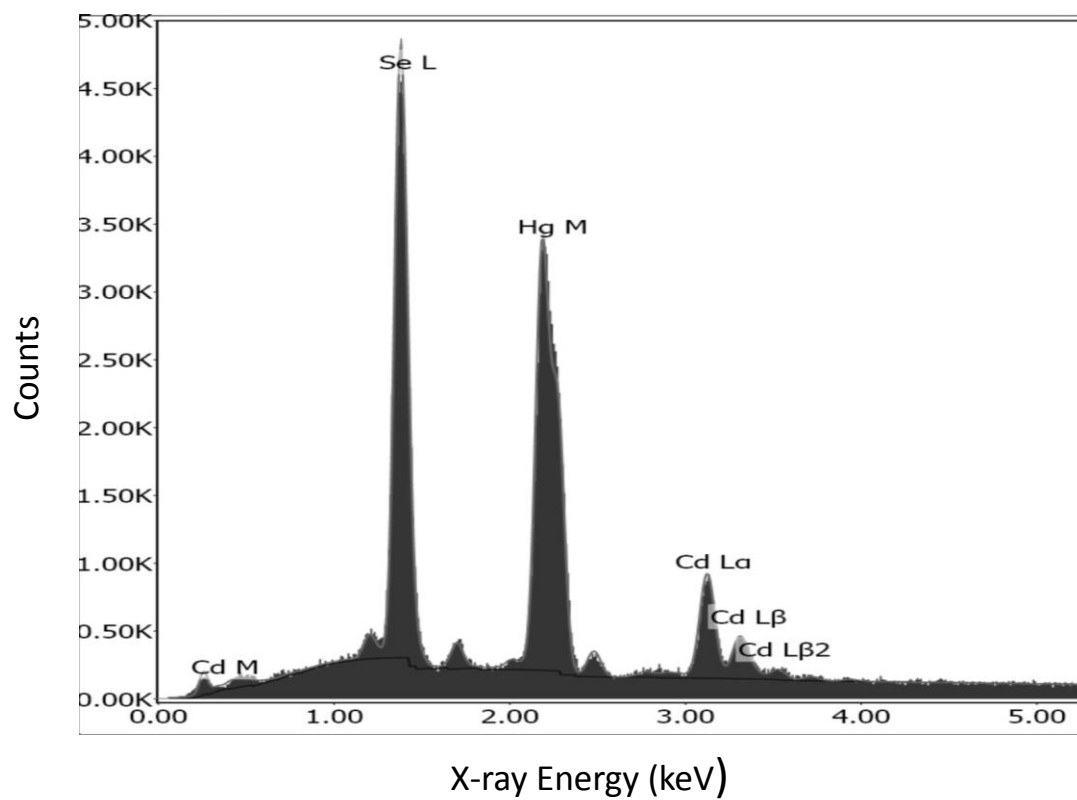
Figure 3-1: EDX spectrum of Hg$_{1-x}$Cd$_x$Se sample SZ105 showing the relative signal strength of x-rays corresponding to the Se-L, Hg-M, and Cd-L binding energies.

interferometer consisting of a beam splitter and two mirrors, one stationary and the other mobile. Moving one of mirrors changes the optical path length along that arm of the interferometer, eliminating different wavelengths in the recombined beam due to destructive interference. The recombined beam is directed through the sample and into a detector. By performing a Fourier transform on the detector signal as a function of mirror position, one can obtain the spectrum of light transmitted through the sample as a function of wavelength [27].

For thin film semiconductors, wavelengths below the cut-off will be absorbed (thus no transmission). Wavelengths above the cut-off will be transmitted, but Fabry-Perot interference from within the sample will produce fringes as seen in Figure 3-2. The cut-off wavelength is defined as the wavelength at which 50% of the maximum observed transmittance of the sample occurs. Producing material with the desired cut-off wavelength is vital for obtaining maximum device performance, and so FTIR measurements will verify that the desired cut-off wavelength is achieved. FTIR spectroscopy was measured on samples using a Nicolet 750 Magna-IR Spectrometer, with a KBr beam-splitter and a DTGS KBr detector. These measurements were performed at room temperature. Once the cut-off wavelength (and therefore the energy bandgap E_g) was measured, the x-value was determined using a model developed by Summers and Broerman [28] given by

$$
\begin{aligned}
E_G(x,T) = {} & -0.209(1-7.172x-2.174x^2) \\
& +7.37\times10^{-4}(1-1.277x-0.151x^2)T \\
& +2.00\times10^{-9}(1+23.45x-599.4x^2)T^2
\end{aligned}
\tag{3-4}
$$

where E_G is in eV and T is in Kelvin.

The x-values determined by FTIR are extrapolations from the optical properties of the sample, unlike EDX which measures the composition directly. However, while FTIR can be performed at atmosphere, EDX must be performed under vacuum to prevent the electron beam
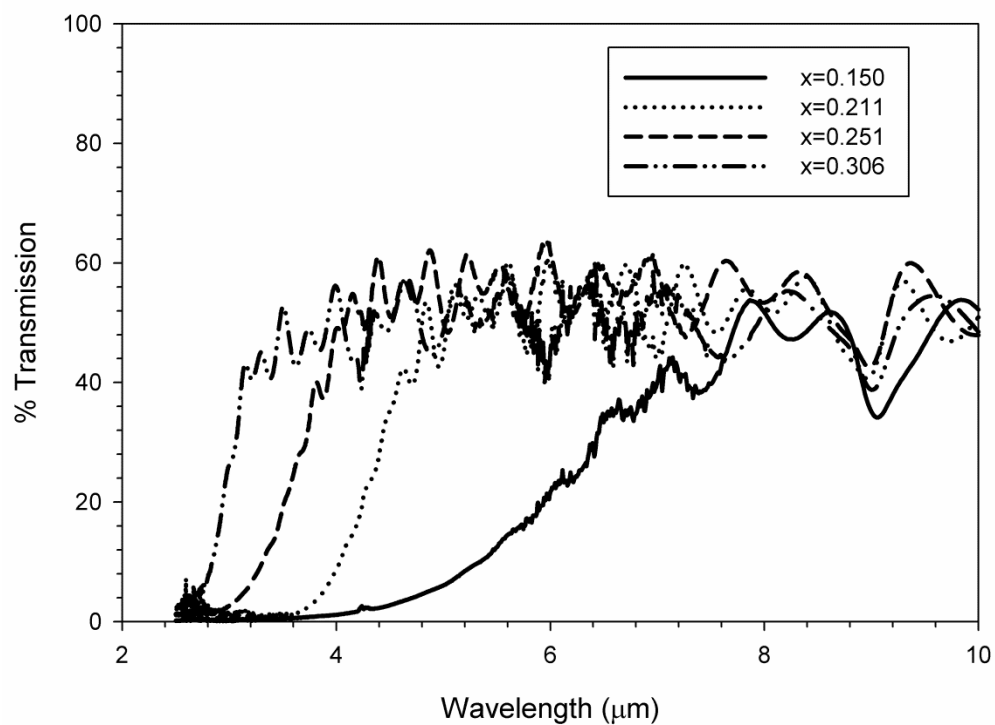
Figure 3-2: FTIR spectra of Hg$_{1-x}$Cd$_x$Se samples with different x-values.
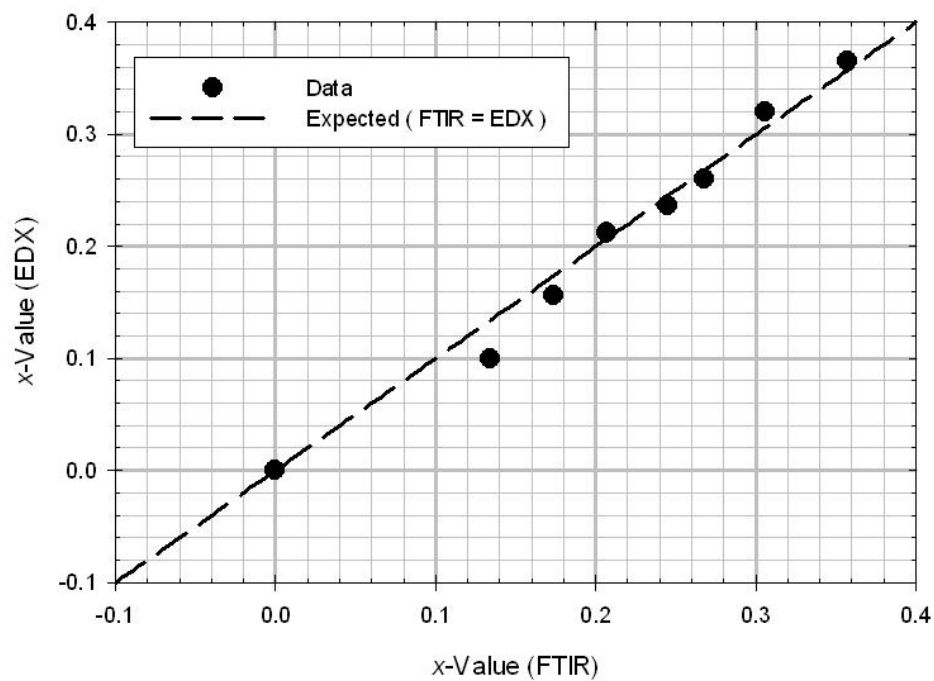
Figure 3-3: Comparison of x-values as determined by EDX and FTIR of certain Hg$_{1-x}$Cd$_x$Se samples.

from being dispersed. Thus FTIR provides a quicker measurement than EDX, and Figure 3-3 shows that the *x*-values determined by EDX and FTIR are generally in agreement. However, for samples with lower *x*-values (and thus narrower bandgaps) there cut-off is less distinct and so FTIR is less reliable.

3.7   **Atomic Force Microscopy**

Both Nomarski and SEM can only produce 2-dimensional images. To obtain a 3-dimensional profile of the sample surface, Atomic Force Microscopy (AFM) was employed. AFM consists of a cantilever with a sharp tip (typically Si) that is brought near the surface of the sample. When placed in close enough proximity, the atomic forces from the surface of the sample (particularly the van der Waals force) acting on the tip will cause deflection of the cantilever. Changes in the surface elevation will change the amount of cantilever deflection, and so by measuring the deflection across the sample a 3-dimensional profile of the surface can be obtained.

The amount of cantilever deflection is measured by reflecting a laser off the top of the cantilever and into a position sensitive photo-detector. These AFM measurements were performed with the cantilever in intermittent contact mode, or tapping mode. Unlike contact mode, in which the scan keeps the tip in constant contact with the surface, tapping mode has the cantilever oscillate just above the surface so that it periodically taps the surface of the sample. Tapping mode gives a quicker scan with less chance of damage to the cantilever and sample surface, but with less accuracy than contact mode [29]. AFM measurements were performed at TxState with two systems, one ex situ and one attached to the UHV buffer line for in situ measurements.

3.8 X-Ray Diffraction

X-ray diffraction (XRD) was used as a measure of crystal quality and to determine the lattice constant a_o of $ZnTe_{1-x}Se_x$ samples. Since the atomic spacing of a typical crystal lattice is on the same order as x-ray wavelengths (~0.1nm), a crystal structure will act as a diffraction grating to an incident beam of x-rays. X-rays scattered off of a crystal lattice will experience constructive interference when x-rays scattered off of different planes of atoms are in phase. As a result, the signal from reflected x-rays will be have peak intensities at specific angles given by

$$n\lambda = 2d \sin \theta \tag{3-5}$$

where θ is the scattering angle, d is the spacing between atomic lattice planes, λ is the wavelength of the x-rays, and n is an integer. This equation is known as Bragg's Law [30]. For a cubic crystal lattice d is given by

$$d = \frac{a_o}{\sqrt{h^2 + k^2 + l^2}} \tag{3-6}$$

Where the integers $h,k,$ and l are the are the miller indices of a lattice plane. Substituting (3-6) into Bragg's Law gives

$$\left(\frac{\lambda}{2a_o}\right)^2 = \frac{\sin^2 \theta}{h^2 + k^2 + l^2} \tag{3-7}$$

and so a_o can be determined by measuring the angle θ at which the peak of a particular lattice plane (hkl) occurs for a given x-ray wavelength λ. However, (3-7) assumes a primitive unit cell containing only one lattice site. Crystal lattices with more than one lattice site per cell will not produce diffraction peaks for certain miller indices due to the presence of additional atoms. For zinc-blende structures such as $ZnTe_{1-x}Se_x$, the (211) plane will not produce a diffraction peak, and so the (422) plane is used instead [31].

41

In XRD measurements, an x-ray beam is directed on to the sample and a detector scans for x-rays at various scattering angles. For a perfect, ideal crystal lattice, this would produce sharp peaks in the x-ray count at the angles given by Bragg's Law. However, imperfections in the lattice such as dislocations and point defects will broaden these peaks. Thus the width of a peak measured at half the maximum value (Full-Width-Half-Maximum, or FWHM) gives a quantitative measurement of the crystal quality.

3.9 Confocal Photo-Luminescence

Photoluminescence (PL) measurement is a commonly used technique to characterize semiconductor samples. In standard PL measurements, above bandgap photons are incident on the sample and are absorbed, exciting the material. The resulting excess carriers thermalize to the bandgap of the sample and recombine to give radiation, and so measuring the resulting PL yields information about the energy bands and impurities in the sample. When applied to the sample on a microscopic scale, this technique can be used to measure dislocation densities. Dislocations are non-radiative defects, and so they appear as dark spots on microscopic PL (μ-PL) images of the sample surface. Thus the dislocation density can be measured by determining the number of dark spots that correspond to dislocations and dividing by the area represented by the μ-PL image. Properly identifying μ-PL features that correspond to dislocations requires very high spatial resolution of the image, and can be difficult for μ-PL images formed using conventional microscopy.

However, spatial resolution can be greatly enhanced by modifying a conventional microscopy system with pinholes placed in the optical pathways that restrict out of focus luminescent signals from reaching the camera focal plane. By applying this confocal arrangement to a μPL imaging system, μ-PL images with very high spatial resolution were

obtained which could be used to determine dislocation densities [32]. These PL measurements, referred to as confocal PL (cPL), were performed on ZnTe and ZnTe$_{1-x}$Se$_x$ samples at TxState using an Olympus FluoView FV1000 confocal microscope. At this time the cPL system is restricted to visible wavelengths, so the dislocation density of an IR material like Hg$_{1-x}$Cd$_x$Se cannot be measured using this technique.

3.10 **Hall Measurements**

3.10.1 **Single Field Hall**

The Hall measurement is a well-established method for determining the carrier concentration of a material. When a current (I_x) is applied across a sample in the presence of a magnetic field perpendicular to the sample (B_z), the charge carriers will be deflected by the Lorentz force. In steady state under sufficiently low fields, a potential difference perpendicular to the current called the Hall Voltage (V_H) given by

$$V_H = \frac{I_x B_z}{qdn} \tag{3-8}$$

where n is the carrier concentration of the sample, d is the thickness, and q is the charge of the carrier: -1.602x10^{-19} Coulombs for electrons, +1.602x10^{-19} Coulombs for holes. Thus Hall measurements also determine whether the sample is p-type or n-type, as holes will produce a positive Hall Voltage, and electrons a negative one [33].

The resistivity (ρ) of any continuous, uniform sample (no gaps or holes) can be determined using the van der Pauw measurement technique. By measuring the resistance of the sample across two perpendicular axes (R_A and R_B), ρ can be determined numerically by

$$\exp\left(\frac{-\pi R_A}{\rho t}\right) + \exp\left(\frac{-\pi R_B}{\rho t}\right) = 1 \quad . \tag{3-9}$$

This relationship holds true regardless of the sample dimensions, and only the thickness t is required to determine resistivity [34]. Once ρ and n have been determined, the mobility of the sample can be calculated using

$$\mu = (en\rho)^{-1} \tag{3-10}$$

where e is the elementary charge of $1.602\mathrm{x}10^{-19}$ Coulombs. While the van der Pauw technique works for any shape, some shapes are more preferable [33]. Hall and van der Pauw measurements were performed on samples cleaved into squares (~5mm x 5mm). Ohmic contacts were formed using indium solder on the corners the squares. The applied current was supplied by a Keithley 230 programmable current source, voltages were measured by Hewlett-Packard 3478A voltmeter, and a Keithley 7001 switching system was used to change different contact configurations for both Hall and van der Pauw measurements. The magnetic field was produced by a GMW Magnet Systems Model 3472-50 water-cooled magnet, with field strengths of 0.1 Tesla. These measurements were taken both at room temperature (300K), and with the samples submerged in liquid nitrogen (77K).

3.10.2 Variable Field Hall

For samples with multiple types of charge carriers, Hall measurement at a single magnetic field will only give the overall average of the concentration and mobility of the sample, which depends on each carrier's contribution to the total conductivity. Samples with a single type of charge carrier with no applied magnetic field have a conductivity given by

$$\sigma = en\mu \qquad . \qquad \text{(3-11)}$$

However, in the presence of a magnetic field perpendicular to the sample, the conductivity in the plane of the semiconductor becomes a tensor given by

$$\sigma = \begin{bmatrix} \sigma_{xx} & \sigma_{xy} \\ -\sigma_{xy} & \sigma_{xx} \end{bmatrix} \qquad \text{(3-12)}$$

$$\sigma_{xx} = \frac{en\mu}{1+(\mu B)^2} \qquad \text{(3-13)}$$

$$\sigma_{xy} = \frac{en\mu^2 B}{1+(\mu B)^2} \qquad \text{(3-14)}$$

where B is the magnetic field strength. This represents the first order correction to the linear Hall effect and takes into account the "orbital" motion of charge carriers in a magnetic field. In this case, the conductivity of the sample will decrease when $(\mu B)^2 \gg 1$, a phenomenon known as magneto-resistance. For large μ, smaller B must be used to obtain accurate Hall measurements.

When multiple species of charge carriers exist in a sample each the conductivity of each species adds to the total conductivity, turning the conductivity tensor components σ_{xx} and σ_{xy} into sums given by

$$\sigma_{xx} = \sum_i \sigma_{xxi} = \sum_i \frac{en_i\mu_i}{1+(\mu_i B)^2} \qquad \text{(3-15)}$$

$$\text{(3-16)}$$
$$\sigma_{xy} = \sum_i \sigma_{xyi} = \sum_i \frac{qn_i\mu_i^2 B}{1+(\mu_i B)^2}$$

where σ_{xxi} and σ_{xyi} are the contributions of a charge carrier with concentration n_i and mobility μ_i to σ_{xx} and σ_{xy} respectively. Since the conductivity of each carrier scales with $(\mu_i B)^2$, varying B will vary the relative contribution of each carrier to the conductivity. Thus by performing Hall

measurements at a range of magnetic fields, one can determine the electrical properties of multiple charge carriers within a sample.

There are two methods of analyzing variable-field Hall measurements. The simplest is to fit the data to the two conductivity tensor components given by equations (3-15) and (3-16) as functions of B, which is known as multiple carrier fitting (MCF). However, this does requires a priori knowledge of how many of each type of carrier to fit the data to, which makes fitting to samples with relatively unknown properties difficult, and it assumes all carriers have discrete mobilities. An alternative method is quantitative mobility spectrum analysis (QMSA). Rather than treating σ_{xx} and σ_{xy} as sums of discrete values, QMSA treats them as integrals over functions of mobility given by

$$\sigma_{xx} = \int_0^\infty \frac{s^p(\mu) + s^n(\mu)}{1 + (\mu B)^2} d\mu \tag{3-17}$$

$$\sigma_{xy} = \int_0^\infty \frac{\left[s^p(\mu) - s^n(\mu)\right]\mu B}{1 + (\mu B)^2} d\mu \tag{3-18}$$

where $s^p(\mu)$ and $s^n(\mu)$ are the conductivity density functions for holes and electrons respectively. By solving equations (3-17)and (3-18) numerically for a range of magnetic fields, the conductivity as a function of the mobility spectrum can be produced without a priori knowledge of the sample [35].

3.10.3 Variable Temperature Hall

The carrier concentration can also depend on temperature, and performing Hall measurements across a range of temperatures can reveal information about electrically active defects and impurities in the crystal lattice. Defects and impurities can generate energy levels in

the normally forbidden bandgap that can typically be occupied by one or more electrons. At sufficiently high temperatures, bound electrons occupying the energy levels close to the conduction band can be excited into the conduction band, increasing the concentration of free electrons. Valence band electrons can also be excited into unoccupied defect levels near the valence band, increasing the concentration of holes. The former are referred to as donors the latter as acceptors. If the temperature is high enough, valence-band electrons can be excited directly into the conduction band. Thus the carrier concentration depends on the temperature, bandgap of the material, and the concentration and energy levels of the various defects.

Consider a semiconductor with a bandgap E_g, donor with concentration N_d and ionization energy E_d, and acceptor with concentration N_a and ionization energy E_a at a temperature T. The probability that an energy level is occupied by an electron follows Fermi-Dirac statistics, and so the energy level is less likely to be occupied as k_BT approaches E_d, where k_B is Boltzmann's constant. If $k_BT>>E_d$, then all of the donor defects are ionized. Thus if the semiconductor is n-type ($N_d>>N_a$), the total free electron concentration n is given by

$$n = N_d - N_a \qquad\qquad \textbf{(3-19)}$$

This is known as the *saturation regime*, where the electron concentration is constant. However, as the temperature is lowered, eventually free electrons from the conduction band will drop down and occupy the defect levels. If $N_d>>n>>N_a$, then

$$n = \sqrt{N_c N_d}\, \exp\left(\frac{-E_d}{2k_BT}\right) \qquad\qquad \textbf{(3-20)}$$

where N_c is the conduction band density of states. This is known as the "half-slope" *freeze-out regime*. As the temperature is lowered further so that $n<<N_a$, (3-20) becomes

$$n = \left(\frac{N_d - N_a}{N_a} \right) N_c \exp\left(\frac{-E_d}{k_B T} \right) \qquad \text{(3-21)}$$

which is the "full-slope" *freeze-out regime.* If the temperature is raised high enough electrons from the valence band can be excited into the conduction band creating intrinsic electrons. When the concentration of intrinsic electrons (n_{int}) exceeds the defect electrons ($n_{int} >> N_d\text{-}N_a$), the concentration is given by

$$n = n_{\text{int}} = \sqrt{N_v N_c} \exp\left(\frac{-E_g}{2k_b T} \right) \qquad \text{(3-22)}$$

and this condition is referred to as the *intrinsic regime*.

Thus by plotting log(n) vs. $1/T$, also referred as an Arrhenius plot, E_g can be determined from the slope of the intrinsic regime, E_d can be determined by the slope of the freeze-out regime, and $N_d\text{-}N_a$ can be determined by the concentration in the saturation regime [36]. Some defects can have E_d located within the conducton band, such as indium (In) impurities in $Hg_{1-x}Cd_xTe$ [3]. In this case no freeze-out regime will be observed, and the saturation regime will extend to zero Kelvin. Variable temperature and variable field measurements were performed on $Hg_{1-x}Cd_xSe$ samples at TxState using a Physical Properties Measurements System (PPMS) purchased from Quantum Design. The PPMS was capable of performing measurements with B ranging from 0 to 9 Tesla, T ranging from 4 to 300 Kelvin.

3.11 Secondary Ion Mass Spectroscopy

SIMS measurements were performed on certain samples by the Charles Evans Analytical Group (Sunnyvale, CA). A high energy ion beam, typically composed of cesium, is directed at the sample. The beam sputters a crater in the sample, expelling atoms from the sample as the ion beam drills into it. This expelled material is analyzed by mass spectrometry in order to determine

the chemical composition of the material, yielding a depth profile of the concentrations of various elements in the sample. SIMS is commonly used in order to determine the incorporation and position of both intentional and unintentional impurities in a semiconductor. Scans were performed for carbon (C), silicon (Si), oxygen (O), bromine (Br), chlorine (Cl), fluorine (F), and sulfur (S).

3.12 **Positron Annihilation Spectroscopy**

In order to investigate the possibility of vacancies in the lattice, positron annihilation spectroscopy (PAS) was used. PAS has previously confirmed the existence of p-type mercury vacancies in $Hg_{1-x}Cd_xTe$ [37]. Samples are placed in a high vacuum chamber and subjected a beam of positrons with an energy ranging from 0-70 keV [38]. The mean penetration depth of the positrons into the solid (Z) in angstroms is given by

$$Z = \frac{400}{\rho_m} E^n \qquad \text{(3-23)}$$

Where ρ_m is the mass density of the solid in gcm^{-3}, E is the positron beam energy in keV, and $n\approx1.6$ for positrons incident on most materials [39]. Once the positrons enter the solid, they quickly reach thermal equilibrium before encountering an electron. When an electron and positron at equilibrium annihilate, they produce two gamma photons at 511 keV moving in opposite directions to conserve momentum. However, the finite momentum of the electron-positron pair prior to annihilation will produce a Doppler shift in the photon energy (ΔE) in the laboratory frame given by

$$\gamma = (511 keV \pm \Delta E)$$

$$\text{(3-22)}$$

$$\Delta E = \frac{cp_{-L}}{2} \tag{3-23}$$

where p_{-L} is the component of electron momentum parallel to the incident positron beam. The range of p_{-L} within a sample results in a Gaussian distribution in photon energy around 511 keV, the analysis of which is referred to as Doppler Broadening Spectroscopy (DBS) [38].

The potential well produced by a neutral or negatively charged vacancy in the lattice site can act as a trap for positrons. Positrons trapped in a vacancy tend to annihilate with the surrounding lower-momentum valence electrons, resulting in a higher count near the center of the Gaussian at 511 keV. Thus shape parameter S, given by

$$S = \frac{A_s}{A_o} \tag{3-24}$$

where A_s is the count area within the detector limit at 511 keV and A_o is the total count area, corresponds to the vacancy concentration. An increase in S corresponds to an increase in vacancies, and vice versa. The potential of a vacancy is a combination of a square well produced by the missing ion and the Coulombic potential if the vacancy itself is ionized. Thus neutral and negatively charged vacancies will trap positrons, but positively charged vacancies will repel them [40]. This presents a problem, because if Se vacancies are producing the electrons in $Hg_{1-x}Cd_xSe$, then they will be positively charged and thus normally invisible to DBS.

3.13 **Rutherford Backscattering Spectroscopy**

The atomic nucleus was discovered in the Rutherford experiment, in which positively charged alpha particles were backscattered off of positively charged atomic nuclei. When a beam of projectile particles with a mass of M_1 of energy E_o is directed at a target atom with mass M_2, the projectile particles will be scattered at an angle θ with energy E_1. If the incident energy E_o is large enough for the beam to avoid electron screening effects, but small enough that the beam

does not penetrate the nucleus and cause nuclear interactions (~ 1 MeV), then the collision is elastic and the scattered energy E_1 is given by

$$E_1 = KE_o = \left[\frac{(M_2^2 - M_1^2 \sin^2 \theta)^{1/2} + M_1 \cos \theta}{M_1 + M_2} \right]^2 E_o \qquad \textbf{(3-25)}$$

where K is referred to as the kinematic factor.

The collision can cause the target atom to recoil with energy E_2 at angle φ, but if $M_1 \ll M_2$ the recoil effects are negligible. Thus by directing a beam of smaller-mass particles (typically protons or alpha particles) of mass M_1 and energy E_o at a target sample, the atomic masses of the different elements composing that sample can be determined from the energies of the backscattered particles detected at a fixed angle θ. This technique is referred to as Rutherford backscattering spectroscopy (RBS), and provides a non-destructive way to measure the composition of a target sample. Increasing the incident beam energy of the alpha particles will also increase the penetration depth of the beam into the sample, and thus a depth profile of the composition can be obtained for up to 2 μm from the surface [41]. Attempts were made to detect interstitials using RBS, but these efforts were ultimately inconclusive.

4 ZnTe$_{1-x}$Se$_x$ Buffer Layers

4.1 Overview

Growing Hg$_{1-x}$Cd$_x$Se layers directly on GaSb substrates has several challenges in addition to the previously described advantages. While Hg$_{1-x}$Cd$_x$Se is a II-VI material, GaSb is III-V. Depositing II-VI material on a III-V surface can create a mixed-phase at the interface, as was reported for CdTe growth on InSb and ZnSe on GaAs [42], [43]. Additionally, Ga from the substrate could diffuse into the Hg$_{1-x}$Cd$_x$Se layer during a post-growth anneal and act as a donor impurity. Such anneals are typically required for IR materials to control vacancies and activate dopants, and thus Ga diffusion could easily contaminate the Hg$_{1-x}$Cd$_x$Se device layers. Another problem is that GaSb substrates are conductive, and so the GaSb substrate and the Hg$_{1-x}$Cd$_x$Se device layers will need to be electrically isolated. A solution to controlling both these problems is to add an insulating II-VI buffer layer between the GaSb substrate and the Hg$_{1-x}$Cd$_x$Se device layer. One possible lattice-matched buffer layers is ZnTe$_{1-x}$Se$_x$.

ZnTe belongs to the same 6.1 Å family of materials as Hg$_{1-x}$Cd$_x$Se and GaSb, and ZnTe can form a ternary alloy with ZnSe. The lattice parameter of a ZnTe$_{1-x}$Se$_x$ can be tuned by adjusting the molar fraction of ZnSe (x) according to Vegard's law. Vegard's law states that the lattice parameter of a ternary alloy a_o composed of two compounds is determined by

$$a_o = a_A(1-x) + a_B(x) \qquad \textbf{(4-1)}$$

where a_A and a_B are the lattice parameters of the two compounds and x is the molar fraction of compound B [44]. The lattice parameters of ZnTe and ZnSe are 6.104 Å and 5.668 Å respectively. Thus the lattice parameter of ZnTe$_{1-x}$Se$_x$ can be tuned to match that of either GaSb or Hg$_{1-x}$Cd$_x$Se, as shown in Figure 4-1. While the primary focus of this research was performed
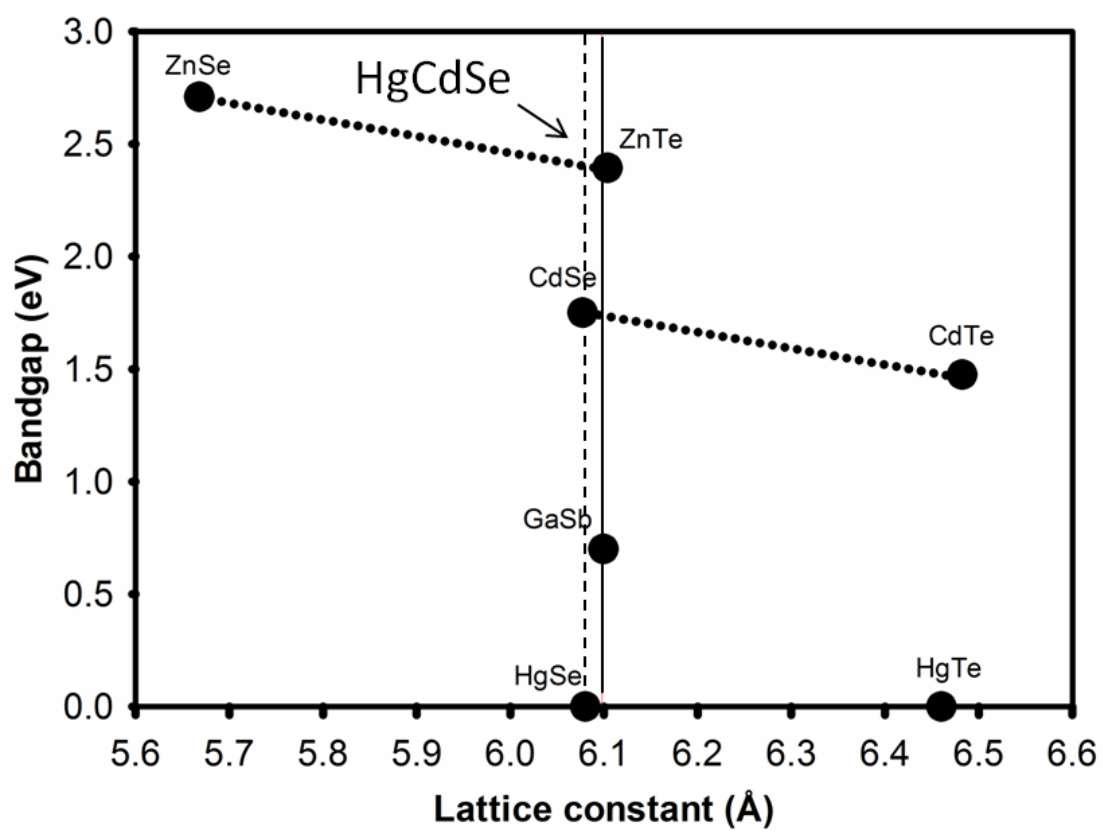
Figure 4-1: Bandgap energy vs. lattice constant for selected materials.

on $ZnTe_{1-x}Se_x$, another potential buffer layer to consider is the ternary alloy $CdSe_{1-x}Te_x$ [11].

The growth of $ZnTe_{1-x}Se_x$ layers on GaSb substrates via MBE was investigated at Texas State University. The first step in this investigation was to examine the preparation of GaSb surfaces for epitaxial growth.

4.2   GaSb Substrate Preparation

4.2.1   Oxide Desorption

In order to produce a crystalline starting surface and to eliminate oxygen contamination of the epixatial layer, any surface oxides that formed on the substrate must be removed prior to growth. For most substrates this involves heating the substrate *in situ* to a certain temperature at which the various oxide layers will desorb from the substrate surface. Different oxides form on GaSb that will desorb at different temperatures. Two predominant surface oxides on GaSb are Sb_2O_5 and Ga_2O_3. As GaSb is heated, Sb_2O_5 decomposes according to

$$2Sb_2O_5 \rightarrow Sb_4 + 5O_2 \qquad \text{(4-2)}$$
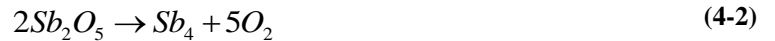
releasing both O and Sb_4 from the surface. The O released in this reaction has the potential to form more Ga_2O_3 according to

$$4GaSb + 3O_2 \rightarrow 2Ga_2O_3 + Sb_4 \qquad . \qquad \text{(4-3)}$$
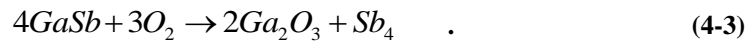
Since Ga_2O_3 decomposes at 550 °C, the substrate must be thermally annealed up to this temperature in order to remove all the gallium oxide. However, up to this temperature the O released in reaction (4-2) can interact with the surface at this temperature, turning (4-3) into a parasitic etching reaction. Thus heating GaSb to ≥550 °C will etch the substrate, leaving a rough,

Ga-rich surface. To replenish the desorbed Sb_4 and prevent etching, GaSb is typically annealed under an Sb overpressure which drives reaction (4-3) to the left side of the equation.

In order to avoid significant Group V Sb contamination of the subsequent II-VI MBE growth, anneals under Group V Sb should be performed in a different chamber. Ideally, a separate chamber would be used to thermally anneal the GaSb substrate under Sb and then deposit a smooth homoepitaxial GaSb layer before transferring it *in situ* to the II-VI growth chamber. Since TxState has such a system, as shown in Figure 2-2, GaSb samples in both the (100) and (211)B orientations were annealed at 550 °C under an Sb BEP of 5×10^{-6} torr in a separate chamber designated for antimonide compounds. Homoepitaxial GaSb layers were then deposited on some of these substrates, producing oxide-free stoichiometric surfaces that could then be transferred in situ to the II-VI chamber for subsequent MBE growths. However, many other laboratories (including ARL) do not have access to a separate III-V chamber as mutli-chamber systems are more expensive for production. Thus alternative methods of GaSb substrate preparation were explored.

One alternative method is to heat under atomic hydrogen, a process referred to as atomic hydrogen cleaning (AHC). Atomic hydrogen (H) reacts with Ga_2O_3 to form

$$Ga_2O_3 + 4H \rightarrow Ga_2O + 2H_2O \qquad \text{(4-4)}$$

where both products are more volatile. Ga_2O desorbs from the surface at 400 °C, over a hundred degrees lower than Ga_2O_3, thus reducing the surface damage caused by the parasitic oxygen reaction given in (4-3) which produces a more Ga-rich surface stoichiometry. Additionally, the H overpressure can suppress the additional parasitic etching reaction caused by the decomposition of Sb_2O_5, turning equation (4-2) into

$$2Sb_2O_5 + 20H \rightarrow Sb_4 + 10H_2O \tag{4-5}$$

and thus reducing the parasitic Ga_2O_3 formed from the reaction (4-3) [18].

The preparation of GaSb substrates in both the (100) and (211)B orientations via AHC was investigated at TxState. GaSb samples were mounted with indium on to silicon wafers in molybdenum holders. AHC was performed in a separate UHV chamber containing only an atomic hydrogen cracker designed by Veeco Inc. The cracker contained a tungsten filament heated to 2000 °C, to produce a cracking efficiency of approximately 6%. Surface composition was monitored via XPS as described in Section 3.2, in a separate UHV chamber connected to the atomic hydrogen chamber via a UHV transfer line as shown in Figure 2-2.

Figure 4-2 shows high resolution XPS scans performed for binding energies corresponding to the Ga 2p, Sb 3d, Ga 3d, and Sb 4d energy levels. Neighboring oxide peaks for both Sb and Ga were reduced after 30 minutes at 400 °C under an atomic H overpressure of 2×10^{-6} Torr. When annealed under vacuum, Sb-oxide peaks were reduced but Ga-oxide peaks increased, which is consistent with Ga_2O_3 being formed according to (4-2) and (4-3), and not desorbing from surface because 400 °C is too low. The formation of excess Ga_2O_3 is suppressed by AHC, scavenging the release of O_2 from Sb-oxide decomposition as described in (4-5) and converting Ga_2O_3 to Ga_2O as described in (4-4). While Ga_2O_3 decomposes to $Ga_2O + O_2$ at 550 °C, Ga_2O desorbs at 400 °C, and so oxides can be removed from GaSb at over 100 °C lower with AHC.

The sample temperature was varied in order to find the lowest possible temperature to remove all oxides from GaSb with AHC. Initially, oxides appeared to be removed with AHC temperatures as low as 250 °C according to the XPS scans shown in Figure 4-3. However, the RHEED patterns of samples cleaned at 250 °C shown in Figure 4-4 were dim and hazy, lacking the sharp streaks and bright patterns of samples cleaned at 400 °C. These initial XPS
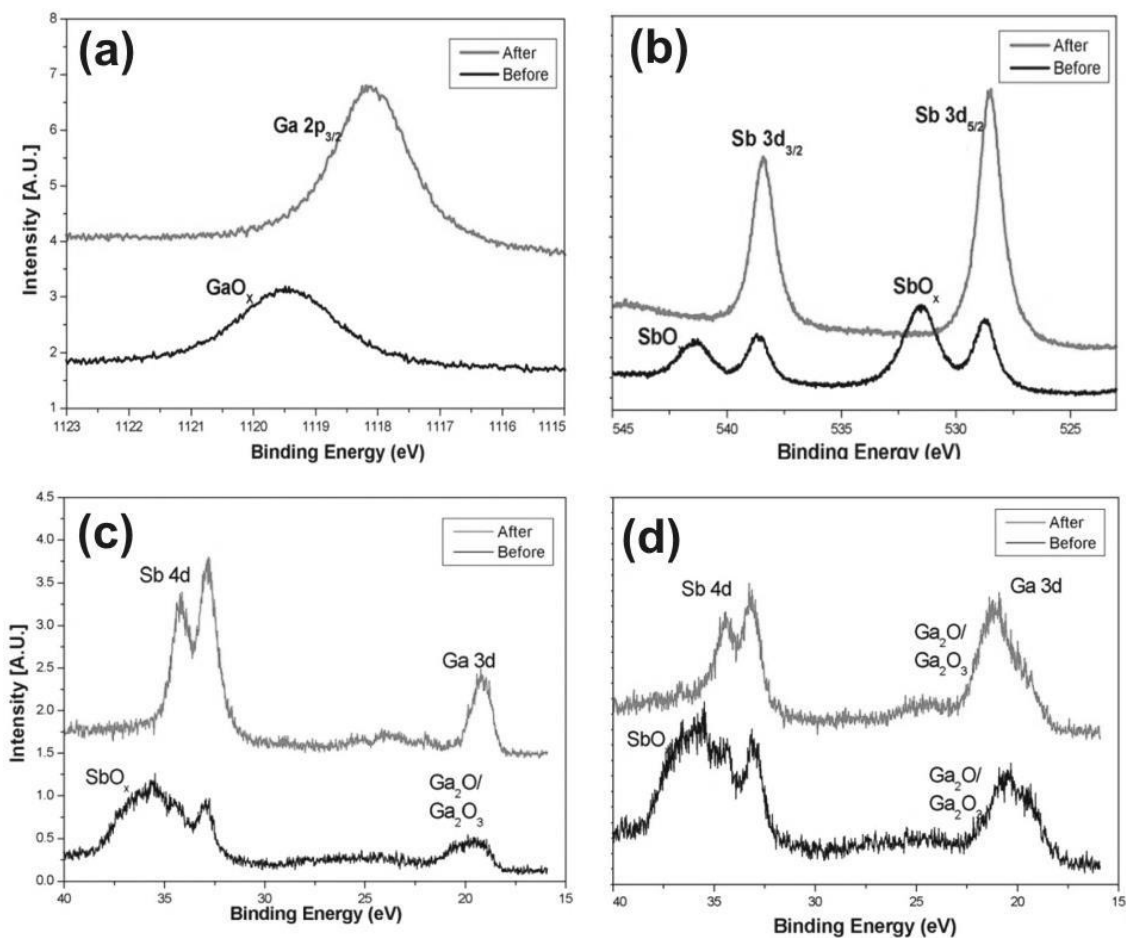
Figure 4-2: high resolution scans before and after cleaning GaSb (211)B at 400 ºC for 30 minutes under a $2x10^{-6}$ torr atomic hydrogen overpressue, focused on regions of (a) Ga 2p, (b) Sb 3d, (c) Sb 4d and Ga 3d, and (d) after annealing without atomic hydrogen (under vacuum) at 400 °C for 30 minutes in vacuum. X-ray beam was at normal incidence.
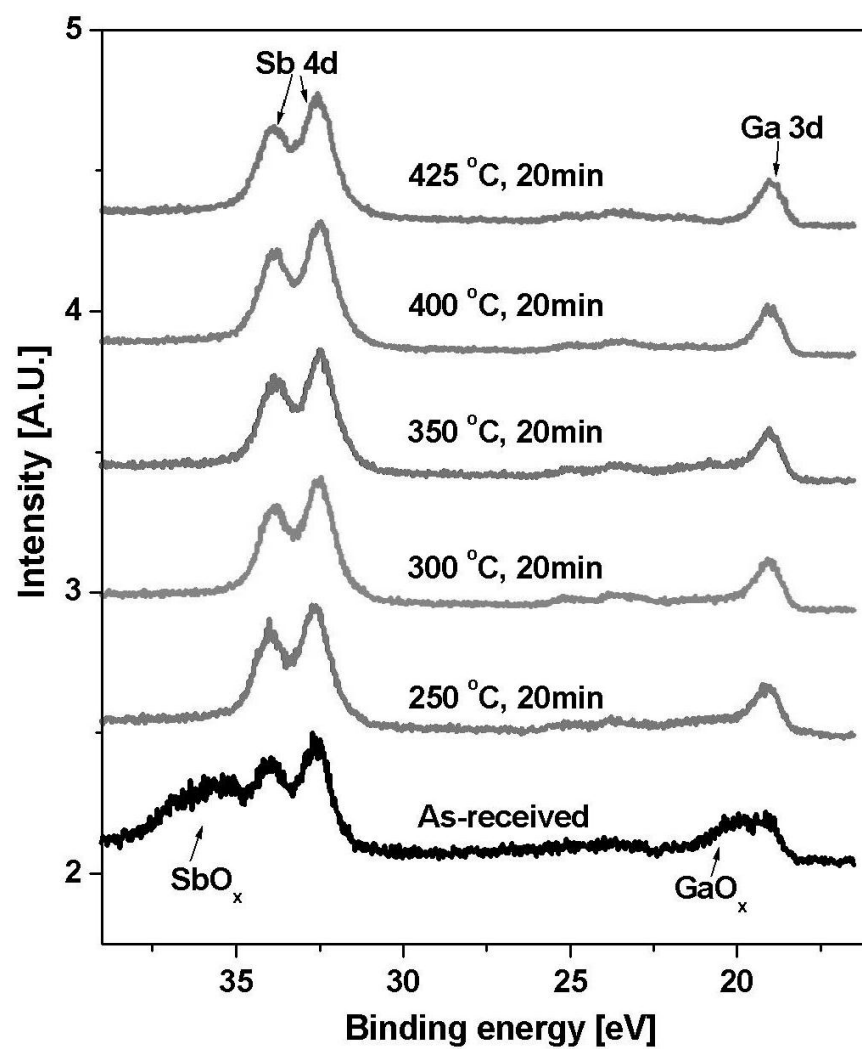
Figure 4-3: High resolution XPS scans of the Sb 4d and Ga 3d regions after AHC at various temperatures.
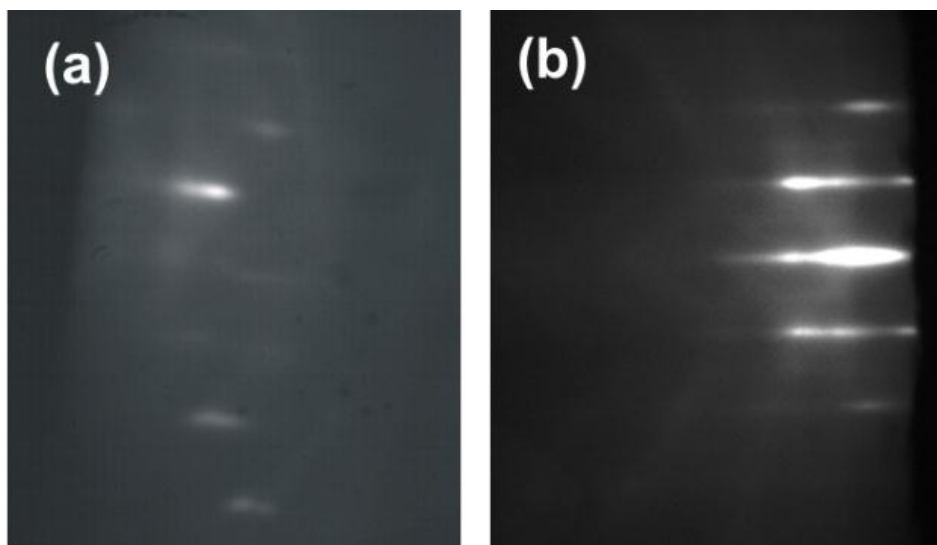
Figure 4-4: RHEED patterns for (100) GaSb AHC for 30 minutes at (a) 250 °C and (b) 400 °C.
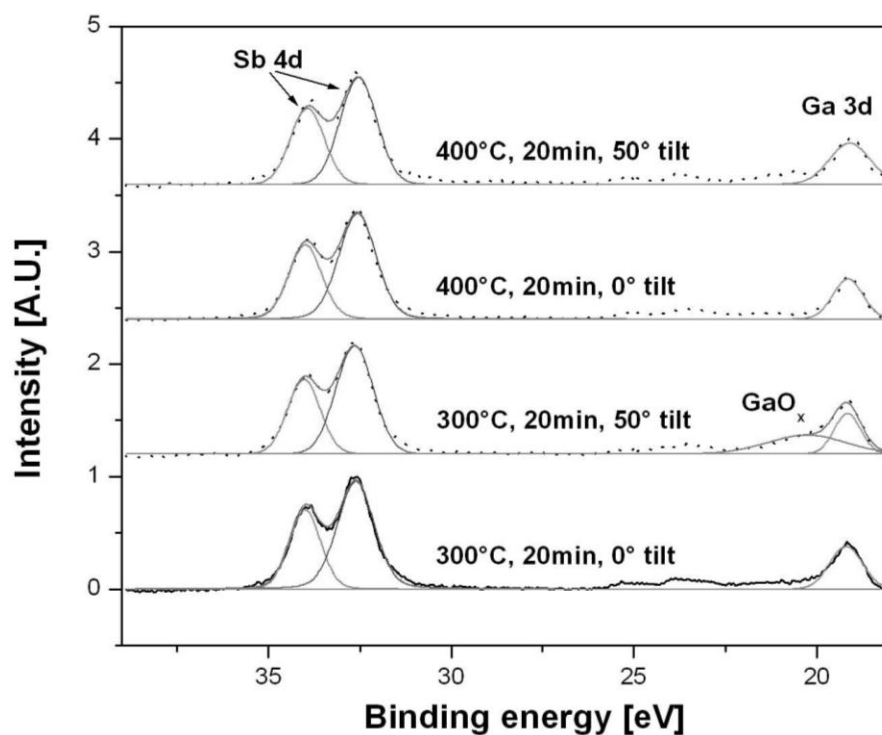
Figure 4-5: High resolution XPS scans of the Sb 4d and Ga 3d regions after AHC with the x-ray beam tilted at 0° and 50°.

measurements had been performed with the x-ray beam perpendicular to the sample surface (0° tilt) causing the x-rays to penetrate deeper into the sample and interact less with the surface. To make the measurement more sensitive to the surface, the m was set at the maximum grazing angle (50° tilt) of the system. While the 0° tilt measurements suggested all oxides removed at 250 °C, the 50° tilt measurements given in Figure 4-5 suggest that some Ga-oxide was left after cleaning at 300 °C. Thus 400 °C is required to completely remove the Ga-oxides with AHC, similar to what has been observed by AHC of GaAs [45]. For both GaSb and GaAs, the fundamental temperature limit is the thermal activation of Ga-oxide desorption.

Another issue to consider is the stoichiometry of the GaSb surface after H-cleaning. As stated previously, thermal annealing of GaSb produces an undesirable Ga-rich surface. Ideally the substrate surface should be stoichiometric, or slightly Sb-rich prior to growth to suppress the second phase formation. The surface stoichiometry for various cleaning methods, given in Table 4-1, was determined by measuring the ratio of the area under the Ga 3d to the area under the Sb 4d XPS peaks for GaSb samples normalized to the ratio obtained from a homoepitaxial GaSb layer. Since the GaSb epilayer was terminated under an Sb-overpressure, it could be a slightly Sb-rich. Nonetheless, this is the best comparator for surface stoichiometry for subsequent II-VI growth.

Thermal desorption under an Sb overpressure produces an Sb-rich surface, while thermal desorption under vacuum produces a surface that is heavily Ga-rich. Two AHC methods were compared: heating the sample to the desired temperature first and then applying the atomic hydrogen overpressure (T, then H), and applying the atomic hydrogen overpressure first and then heating to the desired temperature (H, then T). Greater stoichiometry was achieved with the latter, since it suppresses the parasitic etch reaction as the sample was heated from room temperature to 400 °C. Thus applying an H-overpressure of 2×10^{-6} Torr and then annealing GaSb

Orientation	Method	Temperature (°C)	Normalized Ga/Sb
(100)	Thermal, Sb-Overpressure	560	0.72
(100)	MBE GaSb films	560	1.00
(211)B	Thermal only	400	4.79
(211)B	T, then H 30min	400	0.97
(211)B	T, then H 60min	400	1.35
(211)B	T, then H 30min	250	1.43
(211)B	H, then T 30min	400	1.02
(211)B	H, then T 60min	400	1.03

Table 4-1: Normalized ratio of the area under the Ga 3d and Sb 4d peaks for various preparation procedures of GaSb substrates.

stoichiometry comparable to a homoepitaxial MBE layer. The next consideration when evaluating AHC of GaSb is the roughness of the resulting surface.

4.2.2 Surface Roughness

High quality MBE growth requires that the substrate surface be smooth as well as crystalline and oxide-free. Unfortunately, at this time commercially available GaSb wafers have rough surfaces which contain a large density of pits, typically in the mid-10^9 cm^{-2} range as measured via AFM as shown in Figure 4-6. The origin of these pits is currently unknown. Defect etching (as described in Section 8.2.1) gives a typical dislocation etch pit density $\leq 10^4$ cm^{-2} for these wafers, and XRD measurements of the GaSb substrates give FWHMs of 20-30 arcseconds. Both of these results are inconsistent with dislocation densities in the mid-10^9 cm^{-2} range, so the observed surface pits are most likely unrelated to dislocations in the bulk material.

Surface roughness increased after the initial oxide desorption processes. The pits increased in size after 30 minutes at 400 °C under vacuum according to *ex situ* AFM measurements, and after AHC for 30 minutes at 400 °C (and surface oxides were removed) the pits appeared to take a roughly triangular shape on a (211)B sample according to *in situ* AFM measurements given in Figure 4-7. The pit depth was roughly 6 nm, though the depth measurement could have been limited by the lateral size of the in situ AFM probe tip. The increase in the pit-size with annealing under vacuum could be due to the parasitic etch reaction of (4-2) and (4-3) suggesting the formation of the pits are related to etching.

One possibility is that the GaSb wafers contain nanoprecipitates of different stoichiometry that etch faster in the solution used for chemomechanical polishing (CMP).
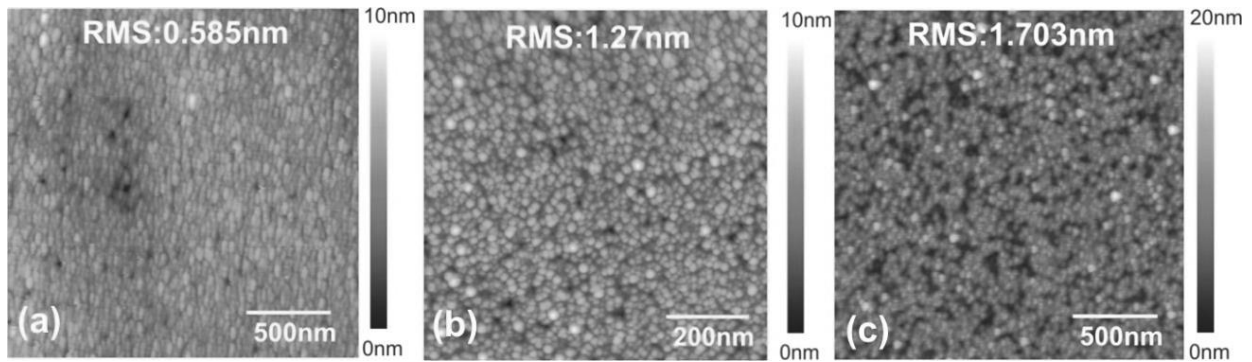
Figure 4-6: AFM surface morphologies of as-received (a) GaSb (211)B from Galaxy, (b) GaSb (111)B repolished by Intelligent Epitaxy , and (c) GaSb (100) from WaferTech.
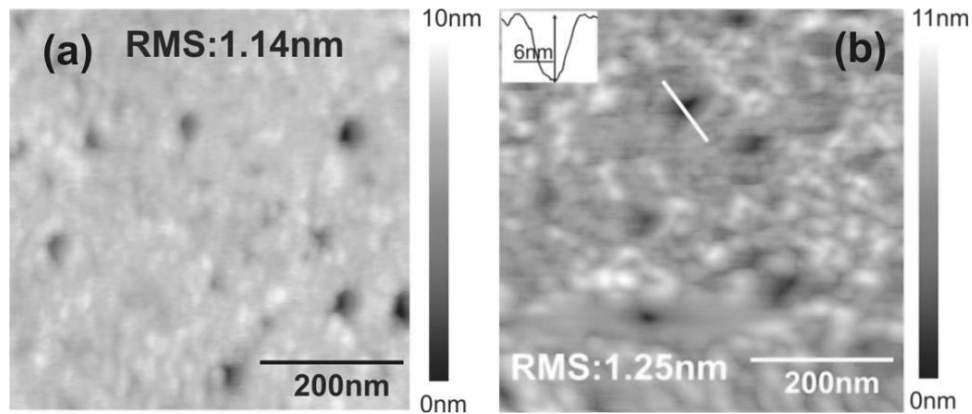
Figure 4-7: AFM surface morphologies of GaSb (211) B with (a) *ex-situ* **measurement after thermal annealing at 400 °C for 30 minutes under vacuum and (b)** *in-situ* **measurement after atomic hydrogen cleaning at 400 °C for 30 minutes.**
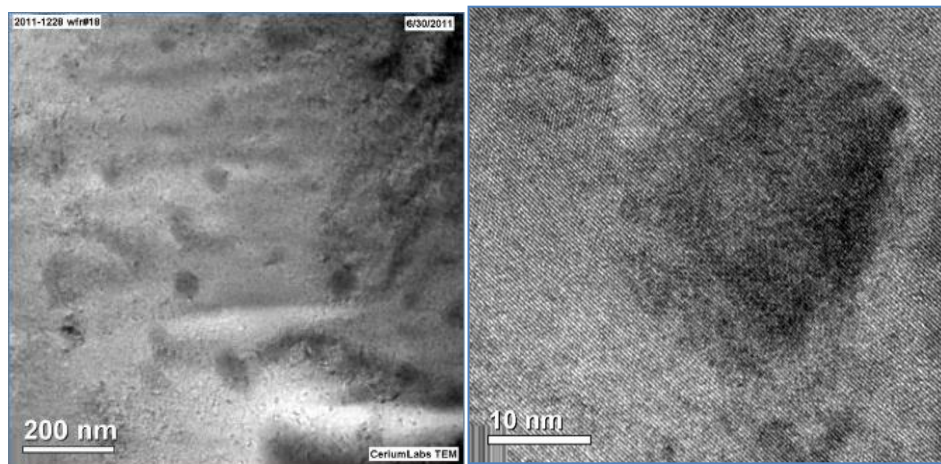
Figure 4-8: TEM images of nanoprecipitates in GaSb (100) sample supplied by Wafertech. TEM performed by Cerium Labs at (Left) 200 nm scale and (Right) 10 nm scale.

Figure 4-8 shows transmission electron microscopy (TEM) measurements performed by Cerium Labs which suggest the presence of nanoscale domains with almost but not quite the same lattice constant, likely a slightly Sb-rich or Ga-rich phase in the material. No other elements were detected. If the CMP solution etches these domains at a faster rate than the rest of the material, then pits would form at these domains on the surface of the sample during CMP. At this time, no CMP process has been found that eliminates the formation of these pits, and consequently all GaSb substrates possess rough starting surfaces.

The density of pits did not significantly change after AHC—indicating that the pits are not related to surface re-oxidation or inhomogeneous oxide removal. However, while the density of the pits did not change after AHC the size of the pits did increase with temperature, resulting in an overall rougher surface as shown in Figure 4-9. Although the GaSb surfaces were still rough after AHC, they were still smoother than GaSb samples thermally annealed under an Sb-overpressure as shown in Figure 4-10. Growing a homoepitaxial GaSb layer on the GaSb substrate produced a smoother surface, but it is not clear that the layers are free from the effects of the pits.

Figure 4-11 and Figure 4-12 show the atomically smooth AFM surface morphologies and long streaky RHEED patterns were observed for (100) and (211)B homoepitaxial GaSb films, which suggest that homoepitaxial GaSb is the preferred method to prepare smooth GaSb substrate surfaces. While homoepitaxial GaSb had atomically smooth surfaces and best RHEED patterns, this does not necessarily mean that they had low dislocation densities. A GaSb layer deposited on a (100) GaAs substrate also produced a smooth pattern shown in Figure 4-13, which is suggestive of step-flow growth. However, the XRD FWHM of this sample was ~150 arcseconds suggests a high dislocation density. Smooth AFM surfaces and streaky RHEED patterns are necessary, but not sufficient indications of low dislocation density epilayers.

64
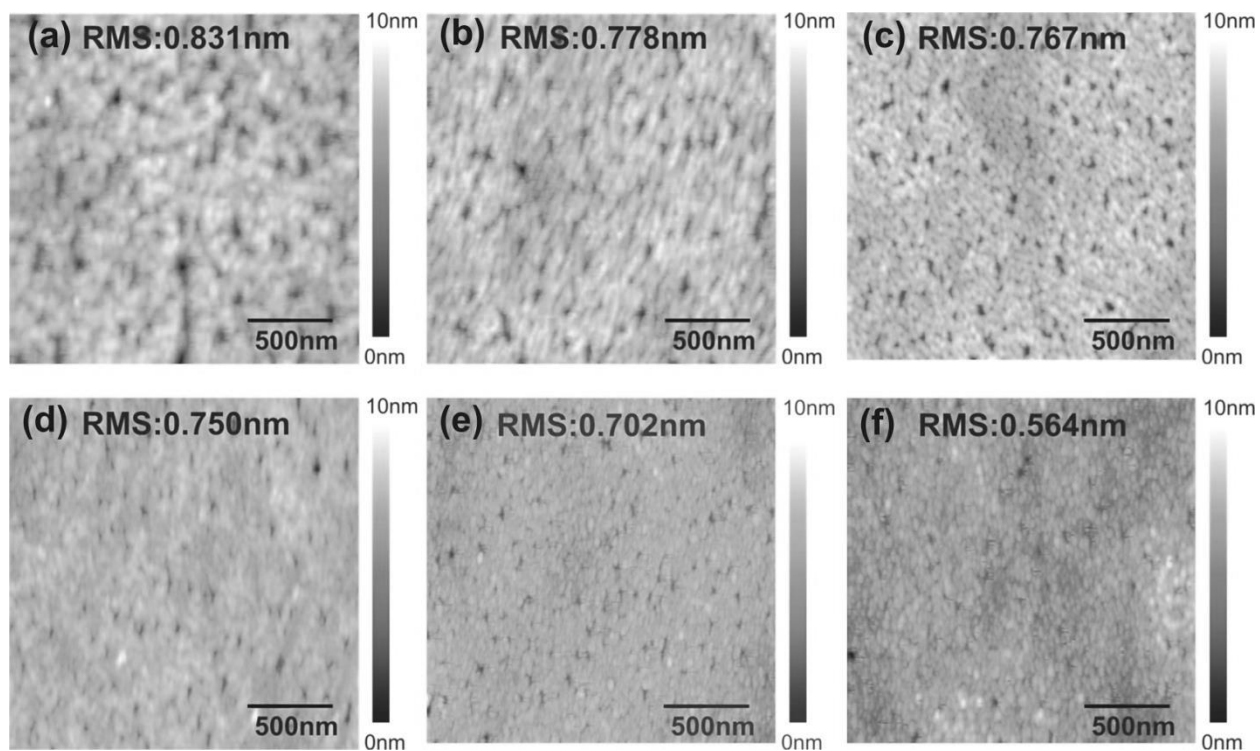
Figure 4-9: AFM surface morphologies of GaSb (211)B with a progression of atomic hydrogen cleaning at (a) 400 °C for 1 hour, (b) 400 °C for 30 minutes, (c) 350 °C for 30 minutes, (d) 300 °C for 30 minutes, (e) 250 °C for 30 minutes, and (f) 150 °C for 30 minutes.
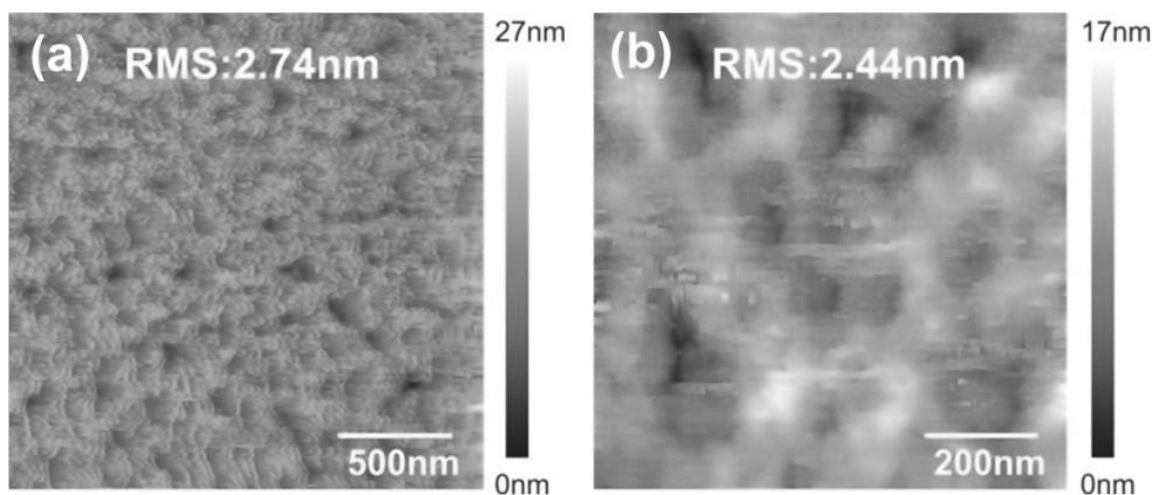
Figure 4-10: *in-situ* AFM surface morphologies of GaSb (100) cleaned by thermal desorption at 500 °C under an Sb-overpressure.
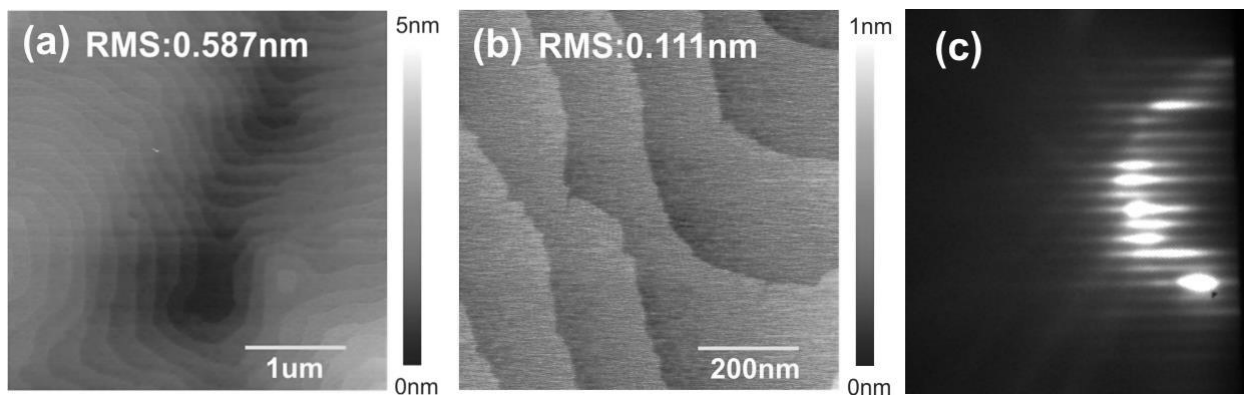
Figure 4-11: Images of homoepitxial GaSb (100) (Sample 7-1666)taken by AFM (a), (b) and RHEED (c).
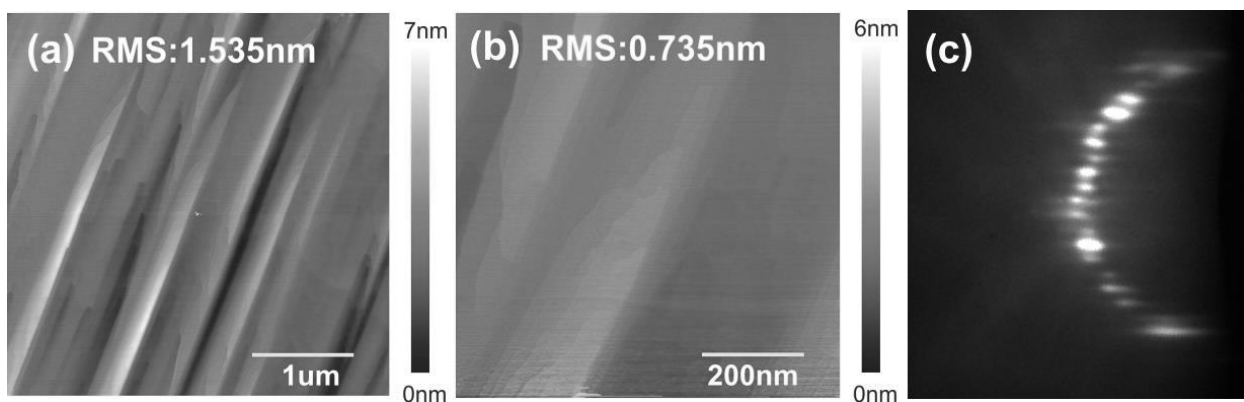
Figure 4-12: Images of homoeptixial GaSb (211)B (Sample 7-168) taken byAFM (a),(b) and RHEED (c
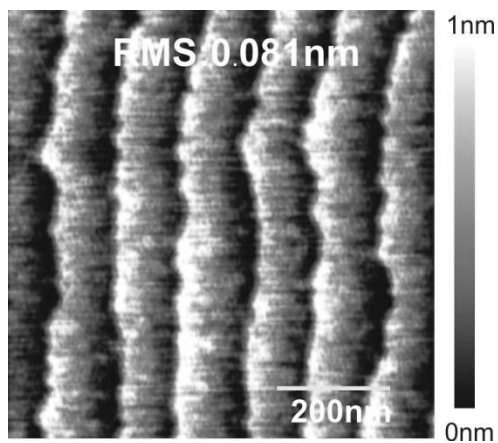
Figure 4-13: *in-situ* AFM of GaSb grown via MBE on (100) GaAs. RMS = 0.081nm

66

4.2.3 Atomic Hydrogen Cleaning Procedure

The pits observed on all GaSb surfaces are a significant problem. A better CMP technique for GaSb substrates and/or better control of compositional fluctuations during GaSb growth needs to be developed. Since no such technique currently exists, and depositing homoepitaxial GaSb layers is impractical for most II-VI MBE systems, the effect of these surface pits on ZnTe and ZnTeSe MBE growth needed to be determined and controlled. Based on the surface stoichiometry and roughness after growth, a standard AHC procedure was established for GaSb substrates:

1) Transfer the GaSb substrate in to the H-cleaning station

2) Slowly warm up the hydrogen cracker filament to 2000 °C

3) Apply an atomic hydrogen overpressure of $2\mathrm{x}10^{-6}$ torr at room temperature

4) Heat the substrate to 400 °C, and hold at this temperature and pressure for 20 minutes

5) After 20 minutes, terminate the hydrogen overpressure. Cool the substrate and hydrogen cracker to room temperature.

6) Transfer the GaSb substrate to the II-VI MBE chamber for growth.

4.3 ZnTe MBE Growth

Prior to investigating $ZnTe_{1-x}Se_x$ growth, ZnTe layers were grown on GaSb substrates to establish a baseline. ZnTe layers were grown on both (100) and (211)B substrates. Additionally, some flux calibration growths were performed on GaAs substrates.

4.3.1 Growth Process

Prior to loading the substrate in the II-VI chamber, the temperature of Zn and Te cells and the valve position of the latter) necessary to produce the desired growth conditions was determined using the BFM. Unless noted otherwise, the substrates were prepared using AHC

according to the procedure given in Section 4.2.3 prior to growth. Once loaded into the II-VI growth chamber, the substrates were heated to the growth temperature (295 °C to 335 °C). Unless the growth was for calibration as described in Section 4.3.2, the substrate was rotated by 10°/min throughout the subsequent growth process. After the substrate had stabilized at the desired temperature, the Zn shutter was opened and the substrate was exposed to Zn for 60 seconds. This was to produce a Zn-stable surface, and minimize the interaction of Te with the GaSb surface. A similar process was used to initiate the growth of ZnSe on GaAs, and was found to suppress the formation of Ga_2Se_3 at the ZnSe/GaAs interface, which can act as nucleation sites for stacking faults [45]. Other groups used a similar Zn pre-treatment for ZnTe/GaSb growth for similar reasons [46].

After this 60 seconds had passed, the Te shutter was opened for 5 seconds and then closed, followed by another 60 seconds with only the Zn shutter open. This technique, similar to migration enhanced epitaxy (MEE), allows the impinging atoms more time to migrate across the sample surface before being incorporated in the epilayer [7]. Increasing the surface migration time of the atoms allows them to reach an optimal position in the crystal lattice, leading to a smoother surface as the sample transitions from GaSb to ZnTe. After this cycle of 5 seconds of Zn and Te exposure followed by 60 seconds of only Zn exposure was repeated for ten periods, the Te shutter was left open and the layer growth took place. Once the layer had reached the desired thickness, the Zn and Te shutters were closed simultaneously and the sample was cooled to 100 °C then removed from the chamber.

Once the sample had been removed the flux from both cells was measured with the BFM to ensure that the flux had not drifted during growth, after which the cells were cooled to their idling temperature.

4.3.2 Growth Rate and Stoichiometry

The growth rates for ZnTe and ZnTe$_{1-x}$Se$_x$ samples were determined by LRI measurements as described in Section 3.3. The Te BEP could be adjusted quickly by adjusting the valve position rather than adjusting the cell temperature which takes a longer time to stabilize. Since LRI can measure the growth rate in real time, and the Te BEP can be rapidly adjusted, growth rate calibration runs were performed in which the Zn BEP and substrate temperature were kept constant while the growth rate was measured for different Te BEPs. These calibration growths were performed on both GaAs and GaSb substrates, and during these runs the samples were not rotated to reduce noise in the LRI signal.

Figure 4-14 shows two such calibration runs performed on a GaAs and a GaSb substrate where the Zn BEP was fixed at $2.3\text{x}10^{-7}$ Torr. The growth rate was found to increase linearly with Te BEP up until ~$4.2\text{x}10^{-7}$ Torr (Zn/Te~0.5), when the slope of the curve decreases and the growth rate starts to level off. This drop in slop, or "knee," observed at the Zn/Te BEP ratio of 0.5 represents the transition point from Zn-rich to Te-rich growth conditions, and so growths performed at Zn/Te=0.5 are considered stoichiometric.

4.3.3 ZnTe Surface

The ZnTe surface was monitored during growth by RHEED, and then measured after growth by AFM and SEM. Figure 4-15 compares the surfaces of two ZnTe layers, Z49 which was grown under stoichiometric conditions, and Z51 which was grown under slightly Zn-rich conditions. Both had bright, streaky RHEED patterns and RMS surface roughnesses of ~0.16 nm, but slightly Zn-rich samples also had more uniform surfaces when observed under SEM. In general, the best quality ZnTe surfaces were obtained by growing under slightly Zn-rich
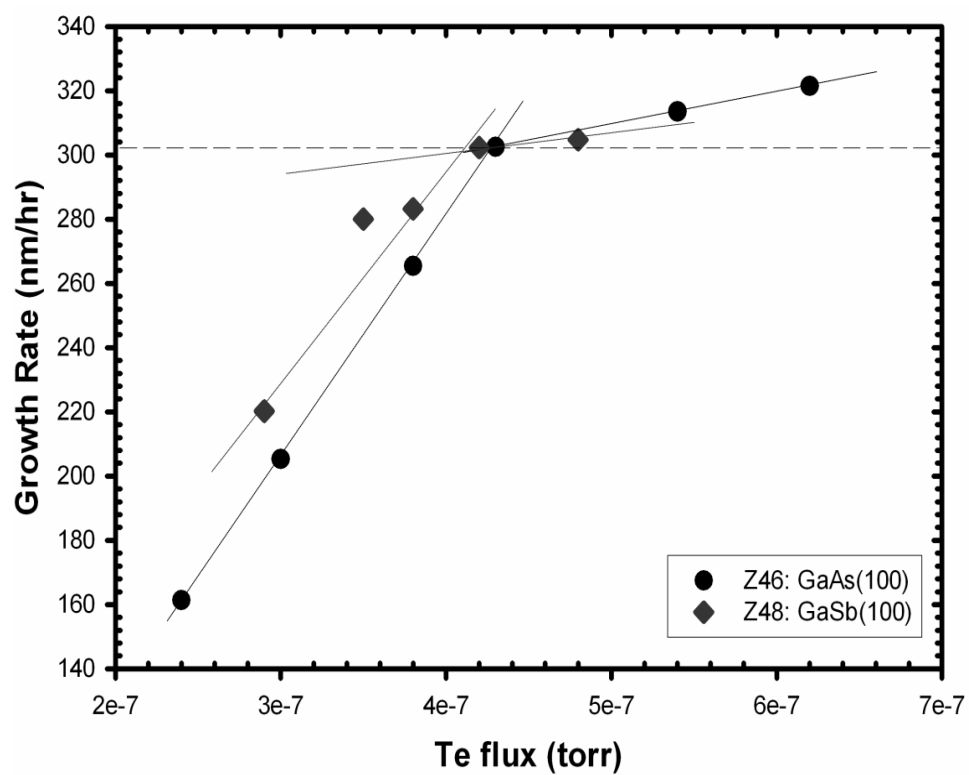
Figure 4-14: Growth rate vs. Te flux for GaAs(100) and GaSb (100) substrates, T_{sub} fixed at 345 °C and Zn flux fixed at $2.3x10^{-7}$ Torr.
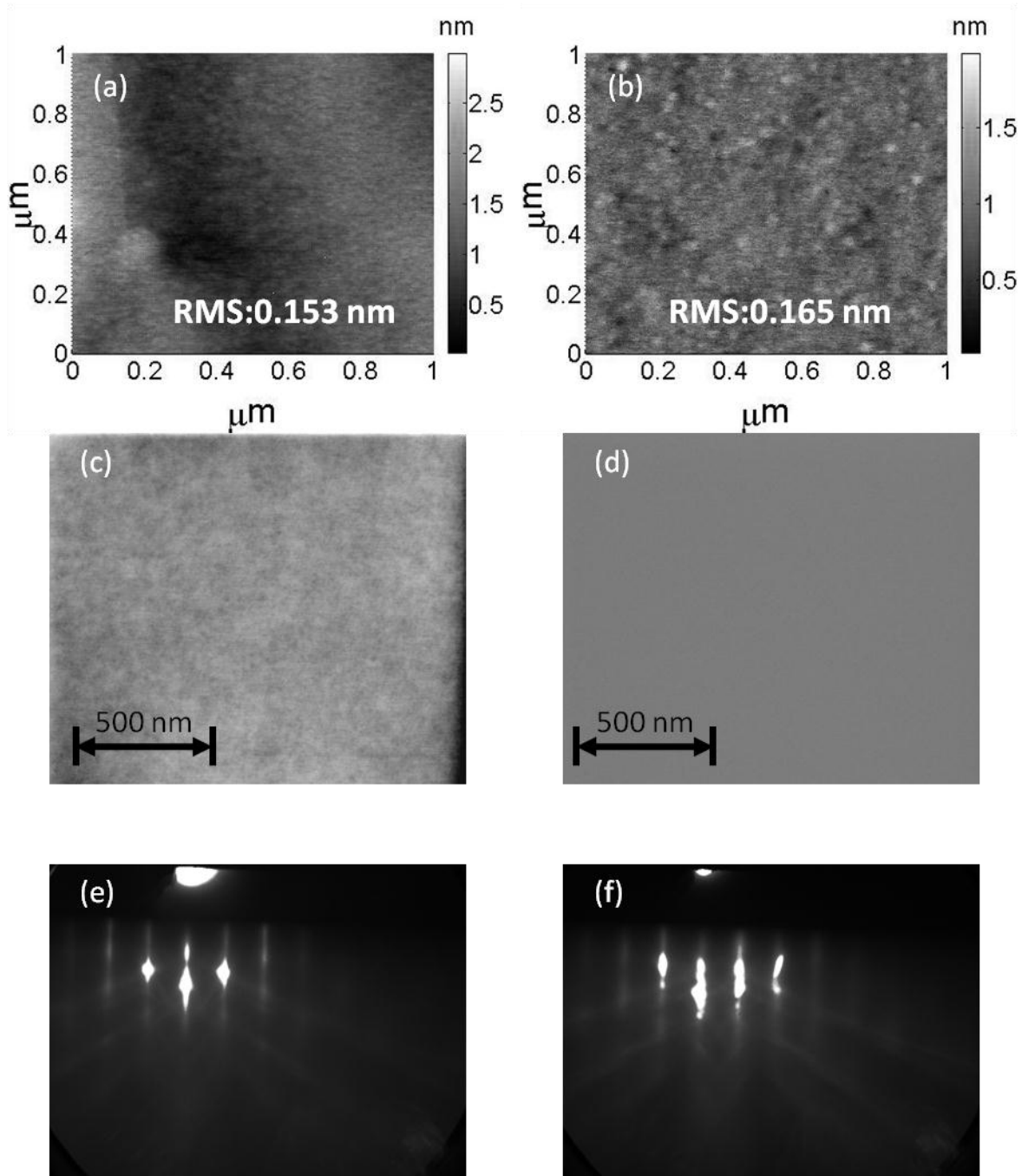
Figure 4-15: Images of stoichiometric ZnTe (Z49) and Zn-rich ZnTe (Z51) grown on (100) GaSb—(a) Z49 AFM, (b) Z51 AFM, (c) Z49 SEM, (d) Z51 SEM, (e) Z49 RHEED, and (f) Z51 RHEED.

conditions.

4.3.4 ZnTe XRD

The FWHM of the ZnTe layers was typically larger than that of the GaSb substrates. GaSb substrates had FWHMs ranging from 20 to 30 arcseconds, while thick ZnTe epilayers had a typical FWHM of ~40 arcseconds as shown in Figure 4-16. In general, the higher FWHM in thicker ZnTe epilayers was due to misfit dislocations created by the slight lattice-mismatch between ZnTe and GaSb. This should be eliminated with $ZnTe_{1-x}Se_x$ layers lattice-matched to the GaSb substrate.

4.3.5 ZnTe Dislocation Density

Figure 4-17 shows images of dislocations in ZnTe layers with various thicknesses on GaSb substrates. These images were obtained using the cPL technique described in Section 3.9. For ZnTe layers with thicknesses less than 100 nm, relatively few dark spots were observed indicating relatively few dislocations. As the ZnTe thickness increases above 150 nm, dark spots begin to appear in large concentrations, indicating an increase in dislocation density. This suggests a critical thickness of 150 nm for ZnTe on GaSb, with misfit dislocations forming as the ZnTe thickness is increased above 150 nm. Furthermore, the relative lack of dislocations observed below 150 nm suggests that few dislocations are formed from the rough GaSb substrate surface after oxides are removed. This indicates that the pits still present on GaSb surfaces after AHC do not contribute significantly to the dislocation density of the ZnTe film, indicating that AHC produces acceptable GaSb surfaces for ZnTe growth.
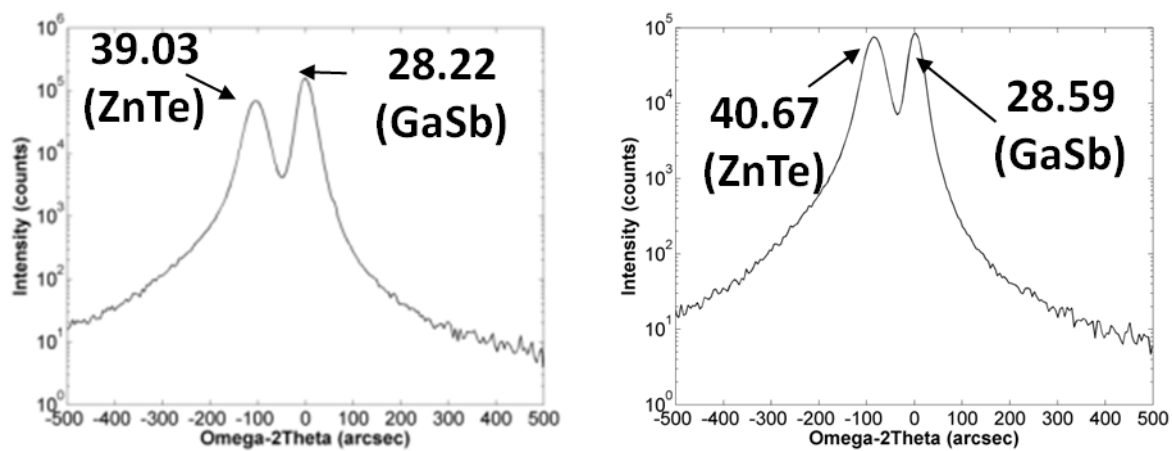
Figure 4-16: XRD scans of 2 μm thick ZnTe grown on (100) GaSb under stoichiometric (Z49, Left) and Zn-rich (Z59, Right) conditions. The FWHM of each peak is given, and the GaSb peak angle is set to zero.
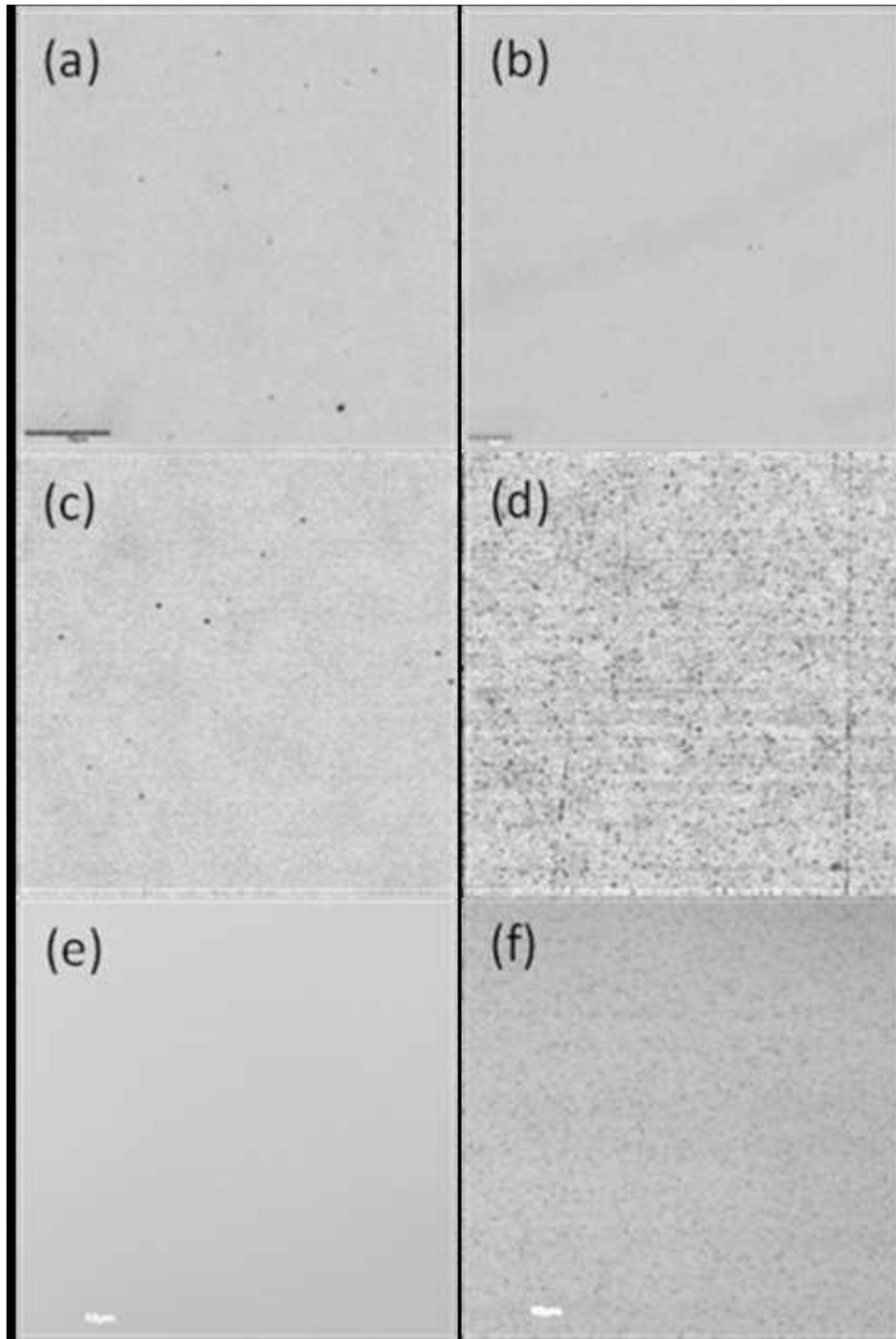
Figure 4-17: Confocal photoluminescence images of ZnTe/GaSb (211)B films grown for (a) 50 nm,(b) 100 nm, (c) 150 nm, (d) 200 nm, and ZnTe/GaSb (100) films grown for (e) 145 nm and (f) 257 nm

4.4   ZnTe$_{1-x}$Se$_x$

Since the lattice parameter of the ternary ZnTe$_{1-x}$Se$_x$ alloy can be adjusted by altering the relative concentrations of Te and Se, the lattice parameter of ZnTe$_{1-x}$Se$_x$ films can be controlled by adjusting the Se/Te BEP ratio. A series of ZnTe$_{1-x}$Se$_x$ layers were grown on (100) and (211)B GaSb substrates in order determine the effect of the Se/Te ratio on lattice constant. Using Vegard's law, the ZnTe$_{1-x}$Se$_x$ alloy should be lattice-matched to GaSb when x=0.01, Se composition of 1% [11].

4.4.1   Growth Procedure

Since lattice-matching ZnTe$_{1-x}$Se$_x$ to GaSb requires such a small amount of Se, the growth characteristics are nearly identical to that of ZnTe on GaSb substrates. The substrate preparation procedure and ZnTe MEE technique described in Section 4.3.1 were used to initiate the growth. Initially the Se shutter would be opened (starting the ZnTe$_{1-x}$Se$_x$ layer growth) once the ZnTe MEE cycle had been completed, but adding a ZnTe buffer was found to improve the quality of the epilayer. The standard procedure adopted for ZnTe$_{1-x}$Se$_x$ growth was to perform the MEE cycle described in Section 4.3.1, and then grow ZnTe for 30 minutes. This produces a ZnTe buffer layer that is roughly 150 nm thick, slightly below the critical thickness. The Se shutter is then opened, initiating growth of the ZnTe$_{1-x}$Se$_x$ layer. ZnTe$_{1-x}$Se$_x$ films were typically grown between 1-2 μm thick.

4.4.2   Lattice-Matching

The lattice constants of the ZnTe$_{1-x}$Se$_x$ films were measured by XRD. Previously, the ZnTe epilayer and GaSb substrate showed up as two distinct peaks in XRD measurements with a fixed separation, as expected due to their slight lattice-mismatch. Figure 4-18 illustrates the
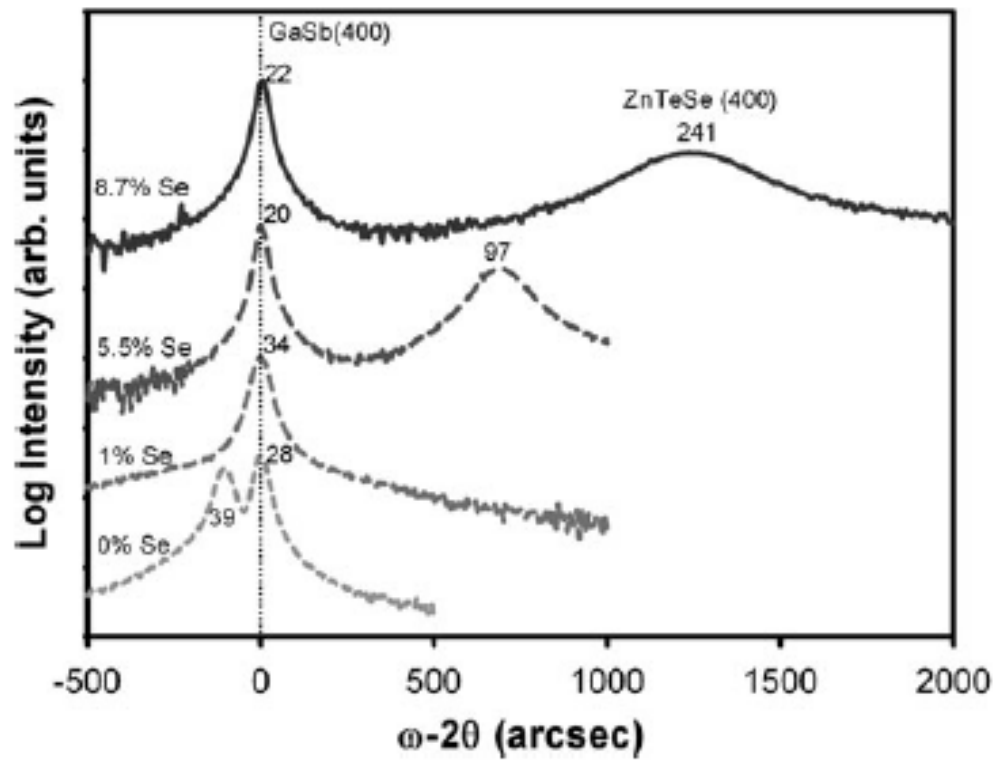
Figure 4-18: XRD scans of ZnTe$_{1-x}$Se$_x$ layers grown on GaSb for several Se compositions. Numbers indicate the FWHM of each peak. The angle of the GaSb peak was set to zero.

effect of adding Se. XRD scans of $ZnTe_{1-x}Se_x$ films grown with an Se/Te BEP ratio of 1% (x=0.01) only had one peak, indicating that the epilayer and substrate peaks overlap and thus have the same lattice constant. Thus $ZnTe_{0.99}Se_{0.01}$ films are lattice-matched to GaSb, as expected, and such films can be grown by using a Se/Te BEP ratio of 1%. The FWHM of $ZnTe_{0.99}Se_{0.01}$ films was ~34 arcseconds, lower than the ~40 arcseconds observed in ZnTe films, but still higher than the 20-30 arcseconds observed in the GaSb substrates. As the Se/Te ratio was further increased, the FWHM $ZnTe_{1-x}Se_x$ peak quickly broadened, indicating a rapid deterioration of the epilayer quality as it deviates from the $ZnTe_{0.99}Se_{0.01}$ lattice-matching condition.

4.4.3 Surface Roughness

Surfaces of $ZnTe_{1-x}Se_x$ epilayers were rougher than those of ZnTe. Figure 4-19 gives the *ex situ* AFM surface morphologies and RHEED patterns of $ZnTe_{0.99}Se_{0.01}$/GaSb samples grown at various substrate temperatures, both of which were improved by growing at higher temperatures. However, while increasing the substrate temperature produced an overall smoother surface, the higher-temperature samples also appeared to have a larger number of features resembling surface pits. The lowest RMS roughness observed was 1.1 nm on a $ZnTe_{0.99}Se_{0.01}$ layer grown at 335 °C, but this sample also had a pit density of approximately 2.5×10^9 cm^{-2}. Given that the pits observed on the GaSb substrates had similar densities, increasing the substrate temperature could be causing the substrate pits to reemerge even though it produces an otherwise smoother surface. Like ZnTe, the smoothest surfaces were produced by growing under slightly Zn-rich conditions.
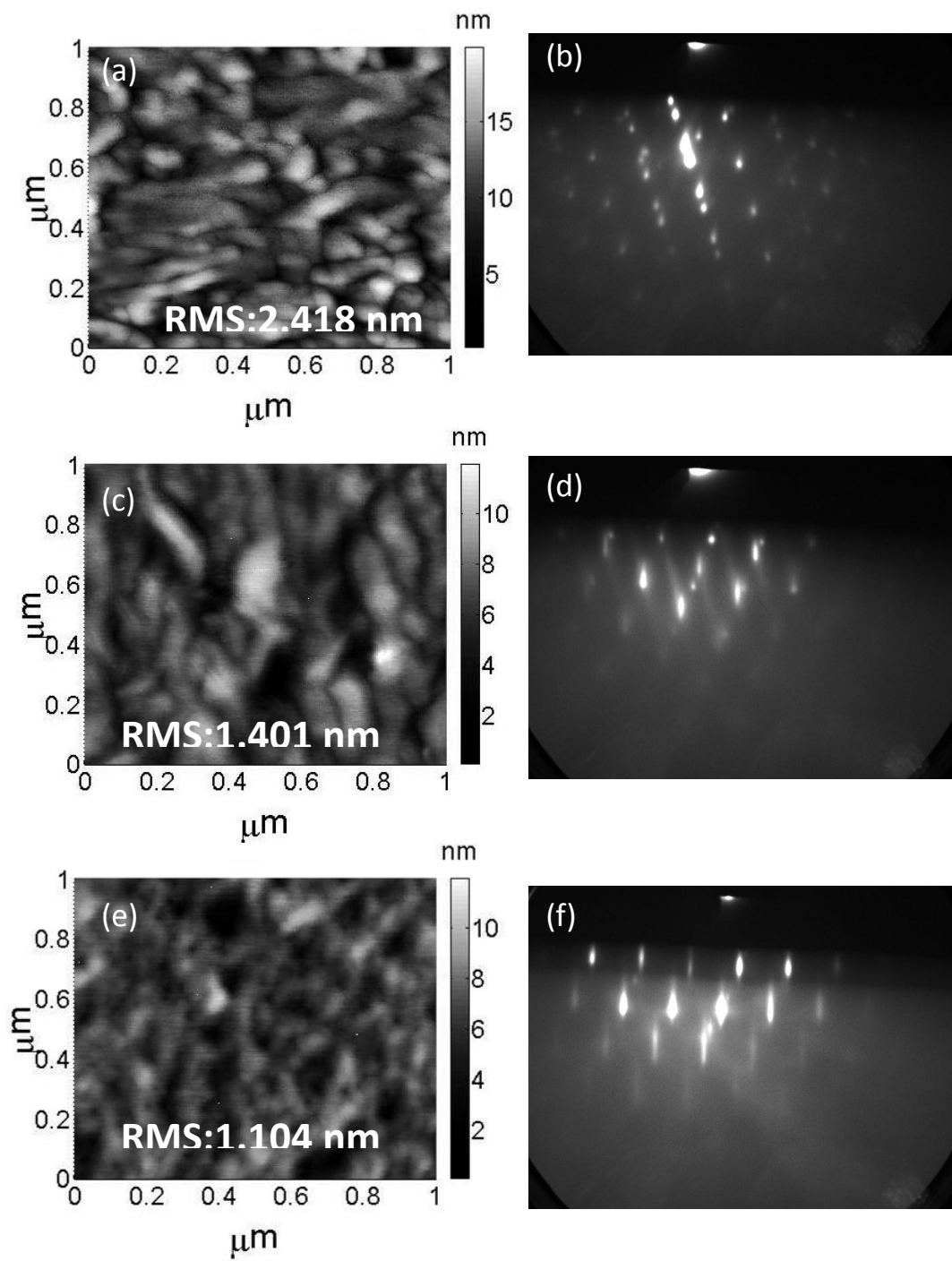
Figure 4-19: Images of ZnTe$_{0.99}$Se$_{0.01}$ samples grown on (211)B GaSb with ZnTe buffer layers at various substrate temperatures: Z74 ,T=305 °C (a) AFM, (b) RHEED); Z75, T=320 °C (c) AFM, (d) RHEED; Z76, T=335 °C (e) AFM, (f) RHEED.

4.4.4 Dislocation Density

The ultimate figure of merit for the $ZnTe_{1-x}Se_x$ buffer layer is the dislocation density. The dislocation density of an epitaxial layer grown on a lattice-matched substrate is still limited by the substrate's dislocation density. Therefore it is of utmost importance that the $ZnTe_{1-x}Se_x$ buffer layer introduces as few dislocations as possible, since they will only add to the dislocations in the $Hg_{1-x}Cd_xSe$ device layers. At this time there is no reliable defect etch for EPD measurements (Section 8.2.1) of $ZnTe_{1-x}Se_x$/GaSb. The Benson etch [47] which is currently used for EPD measurements of ZnTe/Si and other tellurium-based compounds, was found to be ineffective on the $ZnTe_{1-x}Se_x$/GaSb samples. Whether this is due to the different chemistries of selenide compounds or the GaSb substrate (or both) has yet to be determined.

EPD measurements of the GaSb substrates provided by the vendor indicate a dislocation density of $\sim 10^4$ cm^{-2} [11]. As stated in Section 4.3.5, dislocations in the ZnTe were imaged by cPL measurements. ZnTe layers with thicknesses larger than the critical thickness of 150 nm had dislocation densities $\sim 3 \times 10^7$ cm^{-2} according to cPL. However, the cPL measurements given in Figure 4-20 show that the dislocation density of lattice-matched $ZnTe_{0.99}Se_{0.01}$ films with similar thicknesses was only $\sim 7 \times 10^4$ cm^{-2}. This suggests that $ZnTe_{0.99}Se_{0.01}$ films on GaSb substrates do not form misfit dislocations because $ZnTe_{0.99}Se_{0.01}$ is lattice-matched to GaSb, unlike ZnTe. Furthermore, the pits still present on GaSb substrate surfaces after AHC also do not contribute significantly to the dislocation density. Thick $ZnTe_{0.99}Se_{0.01}$ buffer layers can be grown on GaSb substrates with dislocation densities lower than 10^5 cm^{-2}, the same order of magnitude as the GaSb substrate. Thus $ZnTe_{0.99}Se_{0.01}$ buffer layers on GaSb substrates can provide a low dislocation density II-VI surface for MBE growth of $Hg_{1-x}Cd_xSe$.
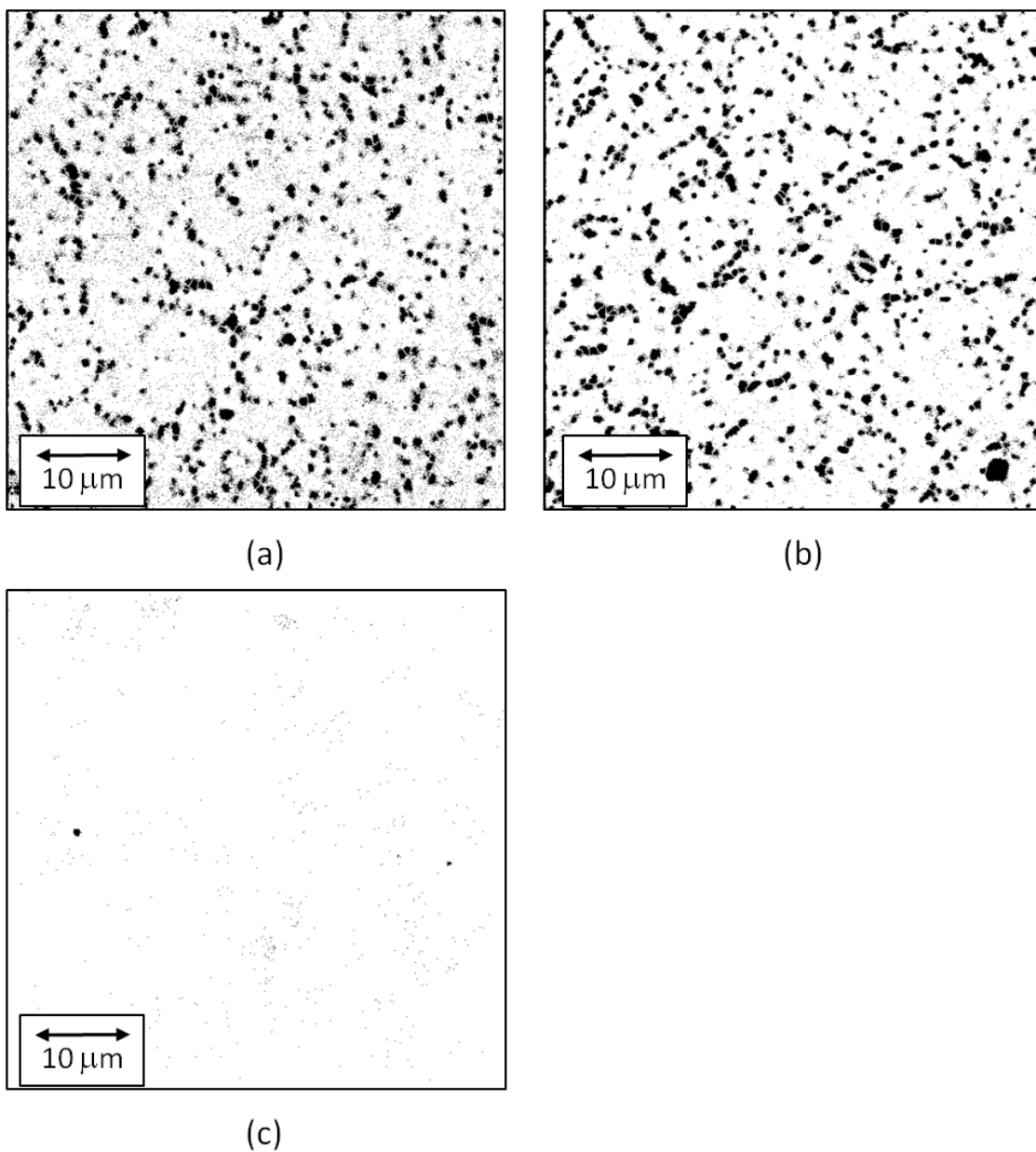
Figure 4-20: cPL images of (a)Z49, 2 µm-thick ZnTe/GaSb (211)B; (b) Z140, 2 µm-thick ZnTe/GaSb (100); and (c) Z74, 1.2 µm-thick ZnTe$_{0.99}$Se$_{0.01}$/GaSb (211)B. Each image represents an area of 54 µm x 54 µm.

4.5 **Summary**

A large density of pits (mid-10^9 cm^{-2}) was observed on the surface of all GaSb substrates, which are believed to be the result of the CMP process preferentially etching nanoscale regions of inhomogeneous stoichiometry. Annealing GaSb substrates under an Sb overpressure and growing homoepitaxial GaSb layers produced atomically smooth surfaces but this method would create contamination problems in a II-VI system and thus would require a separate MBE chamber. AHC was established as a viable alternative for desorbing oxides from GaSb that produces smooth and stoichiometric surfaces comparable to annealing under an Sb-overpressure, and suitable for subsequent high quality II-VI epilayer growth.

ZnTe and ZnTe$_{1-x}$Se$_x$ layers were grown on (100) and (211)B GaSb substrates prepared by AHC. The smoothest surfaces (RMS=1.1 nm) were obtained by growing at higher temperatures (~335 °C) and under slightly Zn-rich conditions, but surface features were visible at these higher temperatures that suggest the surface replicates the surface pits observed on the GaSb substrates. XRD confirmed that the composition of ZnTe$_{1-x}$Se$_x$ can be controlled by adjusting the Se/Te BEP ratio, and that ZnTe$_{0.99}$Se$_{0.01}$ is lattice-matched to GaSb. The FWHM of the ZnTe$_{1-x}$Se$_x$ peak increases when the x-value deviates from the lattice-matching condition of x=0.01, indicating a deterioration in quality most likely due to misfit locations. However, cPL measurement indicated that ZnTe$_{0.99}$Se$_{0.01}$/GaSb has a dislocation density of ~7x10^7 cm^{-2} indicating very little misfit dislocations and that ZnTe$_{0.99}$Se$_{0.01}$ buffer layers on GaSb substrates can provide a low dislocation density II-VI surface for MBE growth of Hg$_{1-x}$Cd$_x$Se.

4.6 **Graded ZnTe$_{1-x}$Se$_x$ Buffer Layers**

Even if no dislocations are formed due to lattice-mismatch, the dislocation density of an epitaxial layer is limited by the dislocation density of the substrate. Cd$_{1-x}$Zn$_x$Te substrates lattice-

matched to $Hg_{1-x}Cd_xTe$ have dislocation densities of $\sim10^5$ cm^{-2}. As a result, even the highest quality $Hg_{1-x}Cd_xTe$ layers will have the dislocation densities $\geq10^5$ cm^{-2}. $ZnTe_{0.99}Se_{0.01}$/GaSb has a lower dislocation density than Cd_{1-x} Zn_xTe, but the slight lattice mismatch between $Hg_{1-x}Cd_xSe$ and GaSb will produce misfit dislocations in the $Hg_{1-x}Cd_xSe$ device layer. $ZnTe_{1-x}Se_x$ can also be tuned to match the lattice constant of $Hg_{1-x}Cd_xSe$. This can be achieved by setting the Se composition of $ZnTe_{1-x}Se_x$ to $x = 0.04$. If a $ZnTe_{0.96}Se_{0.04}$ buffer layer could be produced that preserves the low dislocation density of the GaSb substrate, then $Hg_{1-x}Cd_xSe$ could conceivably be produced with lower dislocation densities than the highest quality $Hg_{1-x}Cd_xTe$. However, as stated in Section 4.4.2, the quality of the $ZnTe_{1-x}Se_x$ layer quickly deteriorates when x in uniform layers deviates from 0.01.

One possible solution to this problem is a graded $ZnTe_{1-x}Se_x$ buffer layer. If the selenium source has a programmable valve, then the Se flux (and therefore the x-value of the $ZnTe_{1-x}Se_x$ layer) can be adjusted during growth. A $ZnTe_{1-x}Se_x$ layer could be deposited on a GaSb substrate with an initial composition of $ZnTe_{0.99}Se_{0.01}$ (lattice-matched to GaSb), but as the growth progressed the Se BEP could be increased, gradually shifting the composition to $ZnTe_{0.96}Se_{0.04}$ (lattice-matched to $Hg_{1-x}Cd_xSe$). This would provide a lattice-matched II-VI surface for $Hg_{1-x}Cd_xSe$ growth that preserves the low dislocation density of GaSb. Such a line of research is currently being considered. Alternately, Te could be added to form the quaternary alloy $Hg_{1-x}Cd_xSe_{1-y}Te_y$. This would allow both the bandgap to be tuned to match the desired spectrum and the lattice-constant to be matched to the $ZnTe_{0.99}Se_{0.01}$/GaSb substrate.

5 Mercury Cadmium Selenide

5.1 MBE growth of Mercury Cadmium Telluride

The difficulties of $Hg_{1-x}Cd_xTe$ growth stem from the low sticking coefficient of Hg at the $Hg_{1-x}Cd_xTe$ surface. As a result, $Hg_{1-x}Cd_xTe$ must be grown at lower substrate temperatures and high Hg background overpressures, but will still typically have large concentrations of Hg vacancies (V_{Hg}). One advantage of growing $Hg_{1-x}Cd_xTe$ by MBE is that growth can be performed at a lower temperature compared to other methods, leading to fewer native defects. The optimal MBE growth temperature for $Hg_{1-x}Cd_xTe$ is typically ~185 °C. However, this temperature requires a large Hg overpressure and still results in a significant concentration of V_{Hg}. These V_{Hg} can be removed by performing post-growth anneals under Hg overpressures.

$Hg_{1-x}Cd_xTe$ growth in the (100) crystallographic orientation was found be particularly vulnerable to the formation of hillock defects, which negatively impact photodiode performance. Growing in the (111)B crystallographic orientation not only reduces the formation of hillocks, it also results in significantly less Hg consumption than (100) $Hg_{1-x}Cd_xTe$ growth. Since the (111)A orientation is a Hg terminated, the surface was found to be more volatile due to the higher vapor pressure of Hg and so the (111)B orientation is preferred. However, the (111)B orientation is prone to forming twin defects in the lattice, with only a few groups reporting the successful growth of twin-free (111)B $Hg_{1-x}Cd_xTe$. Fortunately this propensity for twin formation is reduced by growing in a closely related orientation such as the (211)B or (311)B orientation. As a result, (211)B has been adopted as the standard orientation for $Hg_{1-x}Cd_xTe$ growth [48].

Due to its similarities with $Hg_{1-x}Cd_xTe$, the growth of $Hg_{1-x}Cd_xSe$ via MBE was expected to be similar to that of $Hg_{1-x}Cd_xTe$. Growth of $Hg_{1-x}Cd_xSe$ via MBE was investigated at ARL.

5.2 Growth Procedures

5.2.1 Substrates

As stated in Section 1.5, the optimal substrate for $Hg_{1-x}Cd_xSe$ is expected to be $ZnTe_{1-x}Se_x$/GaSb. However, at the inception of this program these composite substrates were still under development at TxState, and so a cheaper, readily available alternative substrate, ZnTe/Si, was used to investigate the fundamental $Hg_{1-x}Cd_xSe$ growth processes as discussed in Section 1.7. These ZnTe/Si substrates were developed and supplied by ARL [15].

MBE growth of $Hg_{1-x}Cd_xSe$ was first reported in the 1993 by Lansari *et. al.* on ZnTe and $Cd_{0.96}Zn_{0.04}Te$ bulk crystals in both the (100) and (211)B orientations. Much like $Hg_{1-x}Cd_xTe$, $Hg_{1-x}Cd_xSe$ grown in the (100) orientation had a large concentration of hillocks ($\geq 10^6$ cm^{-2}), while (211)B $Hg_{1-x}Cd_xSe$ was hillock-free [14]. For this reason, the ZnTe/Si substrates used in this research were grown in the (211)B crystallographic orientation. The (211)B ZnTe/Si substrates were grown on 3 inch diameter Si wafers. To increase the number of $Hg_{1-x}Cd_xSe$ growth experiments, these wafers were cleaved into 2 cm x 2 cm pieces. Prior to growth, the substrates were etched in a solution of Br and methanol, with a 0.2% Br concentration by volume for 30 seconds to remove the top ~300 nm of the substrate. This was followed by several methanol rinses, then etching for 10 seconds in 10% HCl to remove oxides and trace metals and produce a hydrophobic surface. After HCl, the substrates were rinsed in an overflowing beaker of de-ionized water for 60 seconds, and then mounted onto a molybdenum block using colloidal graphite (DAG). The substrate was secured on the block using clips.

Once mounted, the block was placed in a load-lock and pumped down with a scroll pump to $\leq 10^{-3}$ Torr. The load-lock was then switched from the scroll pump to a sorption pump cooled with liquid nitrogen, as a resistive heater in the load-lock was set to 100 °C for 1 hour to drive

out remaining water vapor. After 1 hour, the heater was turned off and the load lock was pumped down with a second sorption pump cooled with liquid nitrogen for an additional hour before the block was moved into the buffer line and loaded into the growth chamber.

The substrate was then loaded into the growth chamber, and heated to ~300 °C in order to remove any remaining surface oxides. At ~250 °C, a Te overpressure of 2×10^{-6} Torr was applied to the substrate in order prevent Te desorption from the substrate surface. The substrate was kept at ~300 °C under Te for 5 minutes before set to the desired growth temperature, with the Te overpressure terminated when the substrate temperature fell below ~215 °C. This desorption process was determined by monitoring the RHEED pattern, selecting the temperatures which gave the best possible substrate RHEED immediately prior to growth.

5.2.2   Standard Growth Process

Once the substrates stabilized at the desired temperature, the Hg overpressure was applied. Like with $Hg_{1-x}Cd_xTe$, a large Hg overpressure is needed due to Hg's high vapor pressure, and as a result all samples were grown under large Hg overpressures. The standard Hg BEP determined by the BFM was 2.5×10^{-4} Torr and the overall system pressure during growth is raised from the background level of $\sim 10^{-9}$ Torr to $\sim 5 \times 10^{-7}$ Torr. When the Hg overpressure was stabilized, the Se source valve was opened and HgSe growth was started. After 1 minute of HgSe growth, the Cd source shutter was opened and the $Hg_{1-x}Cd_xSe$ layer was grown over several hours to achieve the desired thickness.

$Hg_{1-x}Cd_xSe$ samples were initially grown with a Se effusion cell which produced a $\sim Se_6$ flux, and then a cracker which produced a $\sim Se_2$ flux as described in Section 2.2.2.2. Some of the $Hg_{1-x}Cd_xSe$ layers included cap layers, but most samples consisted of a single layer of

$Hg_{1-x}Cd_xSe$. Growth was terminated by closing the Cd and Se sources simultaneously, and then cooling the $Hg_{1-x}Cd_xSe$ layer to under Hg to prevent desorption from the surface.

5.2.3 Growth Parameters

5.2.3.1 Substrate Temperature

Samples were grown at a range of substrate temperatures from ~90 °C to ~200 °C. More Hg is desorbed from the sample surface at higher temperatures, leading to less Hg incorporation and an overall lower growth rate. Figure 5-1 shows the growth rate of $Hg_{1-x}Cd_xSe$ samples for a fixed set of source BEPs. Growth rate began to decrease when the substrate temperature went above ~140 °C for growths with the $\sim Se_6$ flux and ~ 160 °C for growths with the $\sim Se_2$. Under similar growth fluxes, the optimal growth temperature for $Hg_{1-x}Cd_xTe$ would be ~185 °C. Thus $Hg_{1-x}Cd_xSe$ must be grown at lower temperatures than $Hg_{1-x}Cd_xTe$, most likely due to the higher vapor pressure of Se compared to Te as shown in Figure 2-5. The growth rate did not vary significantly at lower temperatures, but rougher surfaces were observed on samples grown below 90 °C with the Se effusion cell and 140 °C with the Se cracker. Substrate temperature was found to be a significant parameter in determining the surface morphology.

5.2.3.2 Growth Rate

Since all $Hg_{1-x}Cd_xSe$ sample growths have to be performed under a large Hg overpressure, the growth rate at a fixed substrate temperature is limited by the Se and Cd flux. For a fixed Cd and Se fluxes, growth rate was found to vary linearly with Se BEP for both Se sources. Samples grown with an $\sim Se_2$ flux appeared to have a higher growth rate for the same Se BEP as the effusion cell, which initially suggested better incorporation of $\sim Se_2$ fluxes. However, as described in Section 2.2.2.2, the different ionization efficiencies of the Se polyatomic species affect the BEP measured by the BFM. As a result, the BEP measured for an equivalent $\sim Se_2$ flux
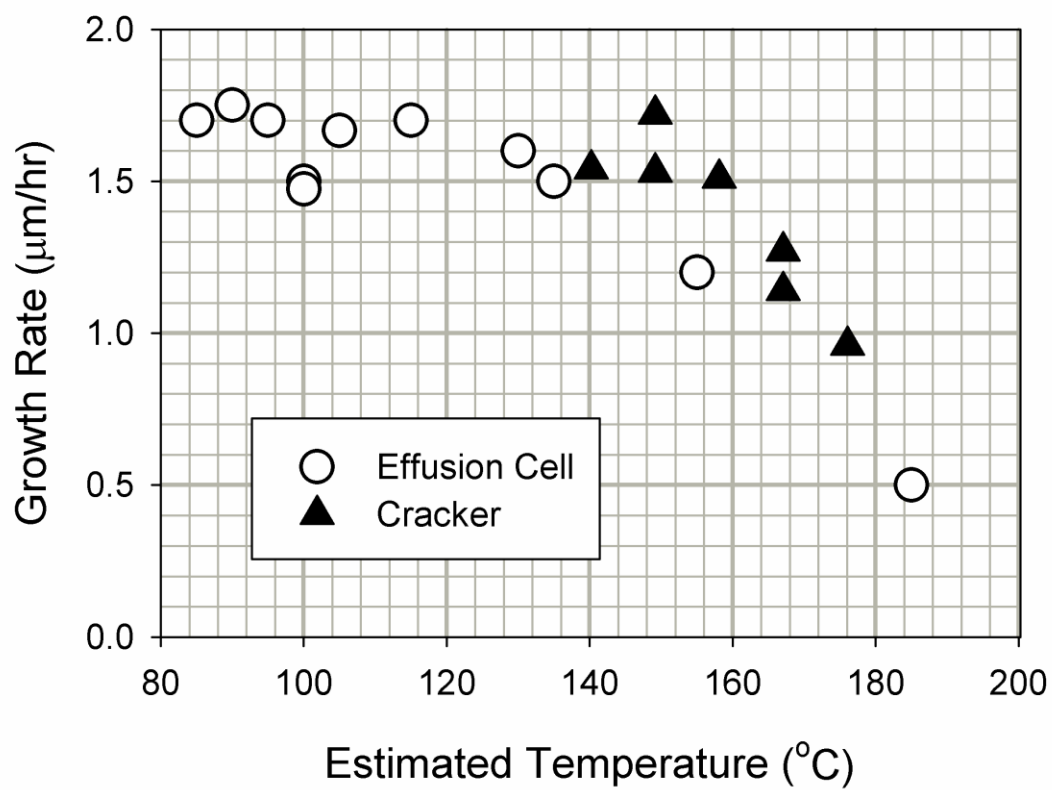
Figure 5-1: Growth Rate vs. estimated substrate temperature for both Se sources, with a fixed set of source BEPs.

is lower than the BEP measured for a ~Se_6 flux roughly by a factor of two. When the cracked Se flux is corrected by this factor of approximately two, the linear curve from the cracker appears roughly match that of the effusion cell as shown in Figure 5-2.

5.2.3.3 *x-value*

The *x*-value of each sample was determined by FTIR as described in Section 3.6. A set of $Hg_{1-x}Cd_xSe$ samples were grown at the substrate temperature, Hg BEP, and Se BEP fixed while the Cd BEP was varied. Figure 5-3 shows that the *x*-value of the $Hg_{1-x}Cd_xSe$ layers (and therefore the cutoff wavelength of detectors made from these layers) varied linearly with the ratio of Cd BEP and Se BEP ratio. When the correction factor was applied to the cracked Se BEP reading, a higher *x*-value (and therefore greater Cd-composition) was achieved for the same Cd/Se BEP ratio. This suggests greater incorporation of Cd with ~Se_2 fluxes than ~Se_6 fluxes.

5.2.4   RHEED Patterns

RHEED measurements were performed during growth as described in Section 3.1, and a set of typical RHEED patterns is shown in Figure 5-4. In general, the RHEED pattern did not vary significantly with the growth parameters used. Desorbing the oxides from the ZnTe substrates left a spotty RHEED pattern, indicating a rougher ZnTe surface. When HgSe growth was initiated the RHEED pattern became streaky, and remained streaky during the $Hg_{1-x}Cd_xSe$ growth. At the end of the growth, when the samples were cooled under Hg, the RHEED patterns consisted of long uniform streaks, indicating a relatively smooth surface. Since Hg and Se are relatively volatile materials, they will tend to migrate across the sample surface and smooth it out before bonding in the epilayer. However, while the RHEED pattern indicated a generally smooth surface, certain features were still observed on the sample surfaces after growth.
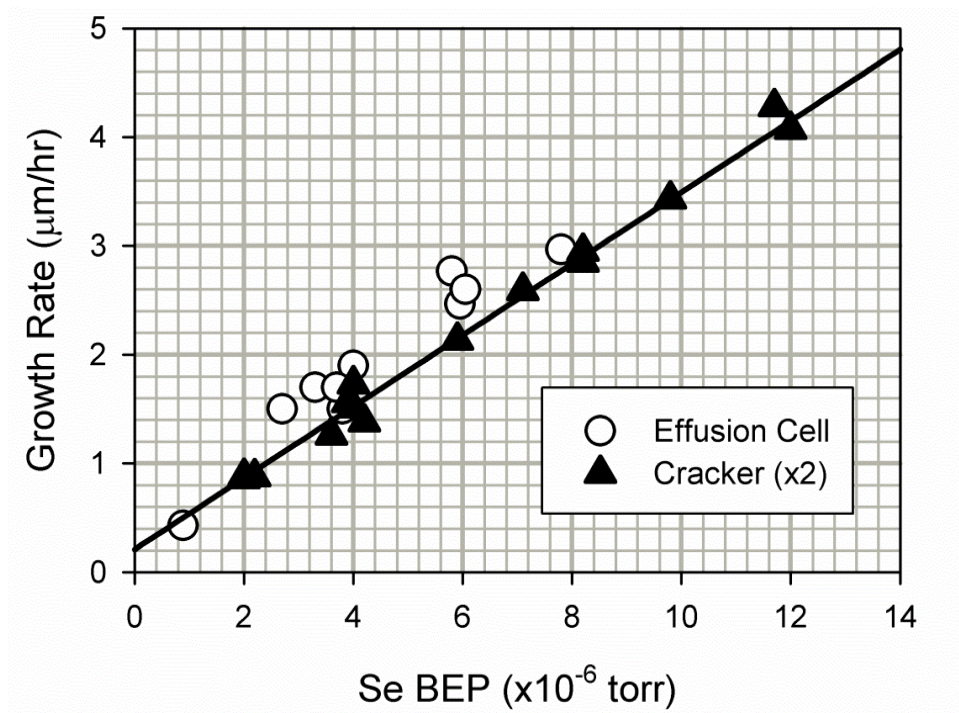
Figure 5-2: Growth Rate vs. Se BEP for Hg$_{1-x}$Cd$_x$Se samples grown with the Se effusion cell (~Se$_6$) and the Se cracker (~Se$_2$) with an x2 correction factor.
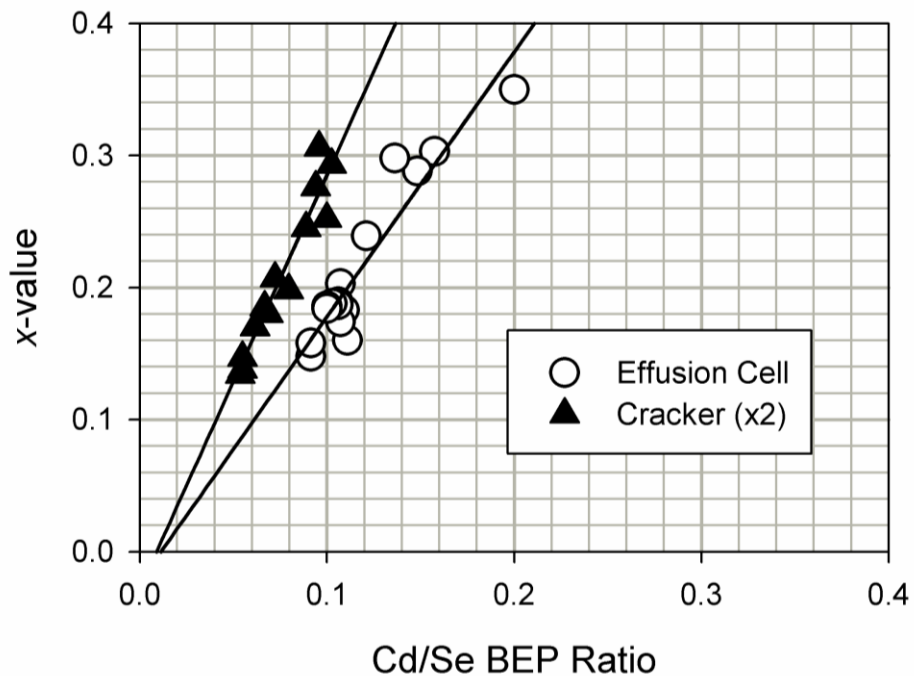
Figure 5-3: x-value vs. Cd/Se BEP ratio for a fixed temperature, Hg BEP, and Se BEP for Hg$_{1-x}$Cd$_x$Se samples grown with the Se effusion cell and the Se cracker as measured by the BFM, and with a correction factor of two to adjust for comparison.
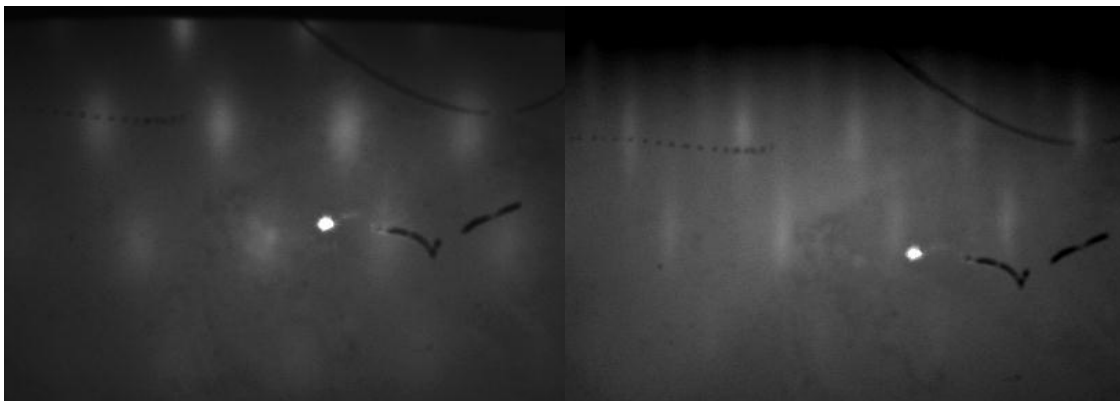
(a)   (b)
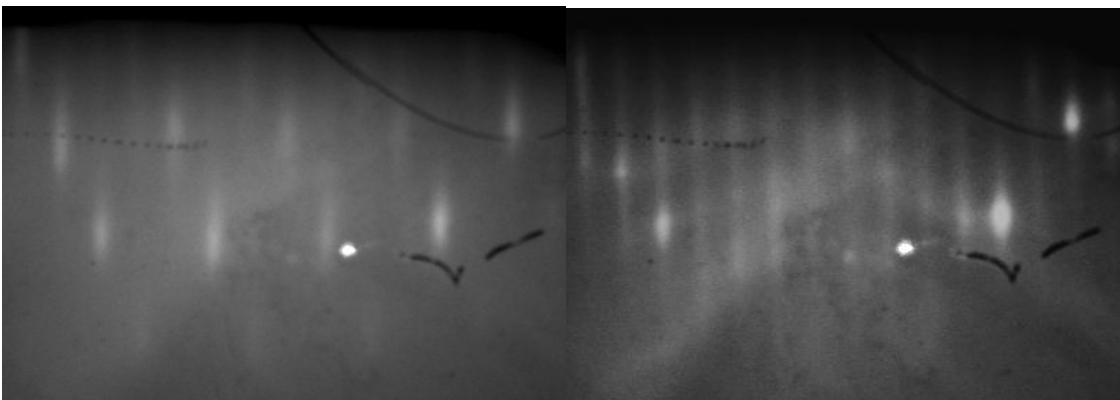
(c)   (d)

Figure 5-4: RHEED pattern observed during of (a) the ZnTe substrate surface prior to growth, (b) sample surface after 1 minute growth of HgSe, (c) sample surface after 1 minute Hg$_{1-x}$Cd$_x$Se growth, and (d) sample surface after growth. Taken from Reference [10].
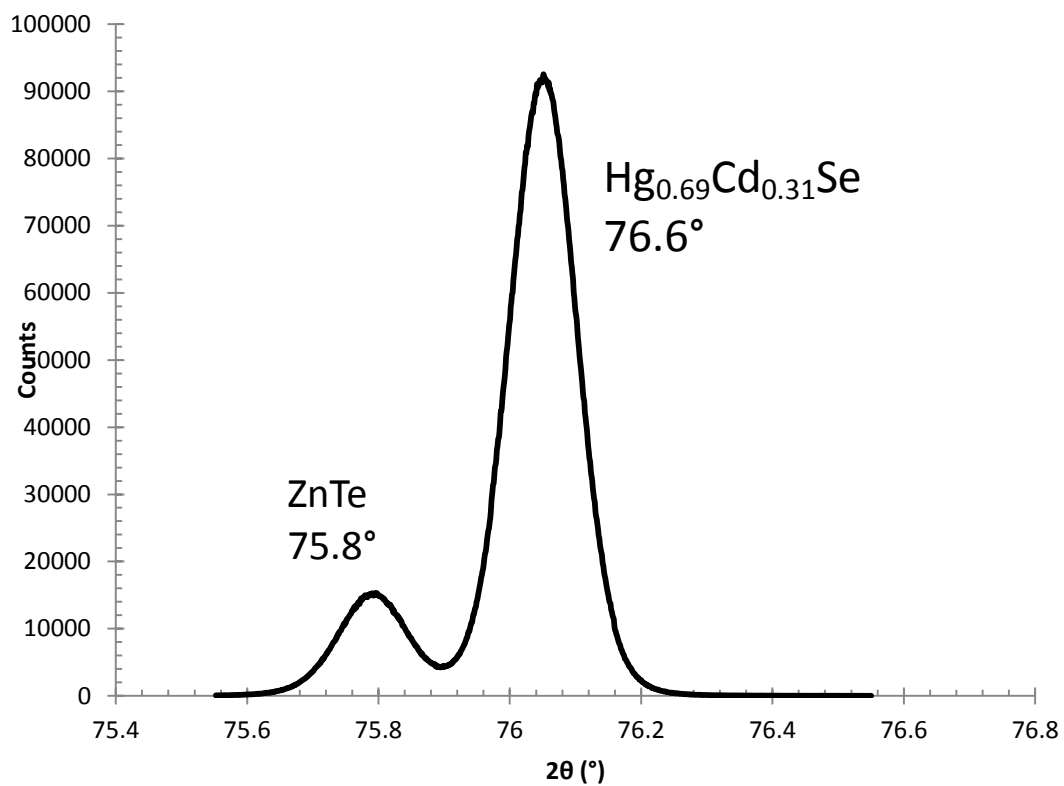
Figure 5-5: X-ray diffraction ω-2θ scan of the 422 peaks of sample SZ110 (x = 0.31) and ZnTe buffer layer of the substrate.

5.2.5   X-ray Diffraction Measurements

While the ZnTe/Si substrates had XRD FHWM's of ~80 arc seconds, the FWHM of the Hg$_{1-x}$Cd$_x$Se layers ranged from 180-300 arc seconds, as shown in F**Error! Reference source not found.**. A higher FWHM is to be expected in the Hg$_{1-x}$Cd$_x$Se layer due to the lattice mismatch between ZnTe and Hg$_{1-x}$Cd$_x$Se. The Hg$_{1-x}$Cd$_x$Se FWHM should be greatly improved when grown on a lattice-matched ZnTe$_{1-x}$Se$_x$/GaSb substrate, as described in Section 4.

5.2.6   Surface Features

One indication of the quality of an epitaxial layer is the morphology of the sample surface. Certain defects introduced in the crystal lattice during growth will produce visible features on the sample surface, some of which (such as hillocks) are detrimental to device performance. A particularly egregious defect occurs where a portion of the crystal undergoes a rotational twinning, bringing a different crystal orientation with a faster growth rate of that portion of the crystal to the surface producing hillocks. Other defects produce a slower growth rate in portions of the crystal, producing pits and voids. Thus the growth parameters should be selected to produce the smoothest surfaces with the fewest possible features. Hg$_{1-x}$Cd$_x$Se sample surface features were characterized using Nomarski microscopy, AFM, and SEM.

5.2.6.1   Needle Defects

One of the most prominent surface features observed were needle defects, as shown in Figure 5-6. Needle defects have been observed in Hg$_{1-x}$Cd$_x$Te and are typically considered the result of dislocation defects looping together, causing strain that is partially relieved by forming a needle-like defect on the surface [49]. From SEM micrographs, the needle defects appear to have a length of ~2μm and from AFM measurements the depth of the needle defects appears to

be ~100 nm. Needle defects were typically observed in greater densities on samples grown at higher temperatures, suggesting that growing $Hg_{1-x}Cd_xSe$ under Hg-deficient conditions leads to more dislocations. Further XRD measurements are required to determine if the needle defects in $Hg_{1-x}Cd_xSe$ are related to twin defects.

5.2.6.2   *Void Defects*

A common problem found in $Hg_{1-x}Cd_xTe$ samples are void defects as seen in Figure 5-7. Void defects are commonly formed by precipitates of Te disrupting the $Hg_{1-x}Cd_xTe$ lattice, forming craters on the surface. Void defects are typically more prevalent at lower Hg overpressures and higher substrate growth temperatures. $Hg_{1-x}Cd_xTe$ samples with large concentrations of void defects typically have shorter excess carrier lifetimes, and thus poorer device performance [49]. Of significance, void defects were not observed at any growth temperature on any $Hg_{1-x}Cd_xSe$ samples. This suggests that Se does not form precipitates in $Hg_{1-x}Cd_xSe$ the same way that Te does in $Hg_{1-x}Cd_xTe$.

5.2.6.3   *"Diamond" Defects*

Another notable surface feature observed on the $Hg_{1-x}Cd_xSe$ sample surfaces were "diamond" shaped defects like those shown in **Error! Reference source not found.**. These defects appear at higher growth temperatures and lower Hg overpressures, thus Hg-deficient conditions. Defects of this particular shape have not been reported on $Hg_{1-x}Cd_xTe$, and at this time their exact cause is unclear. However, they could be related to elongated hillock defects, which would indicate twinning. Further research is required to determine this.

5.2.6.4   *Cross-hatch Patterns*

High quality $Hg_{1-x}Cd_xTe$ grown in the (211)B orientation will often display a pattern of crossed lines at 44-45 degree angles to each other visible under Nomarski microscopy. This is
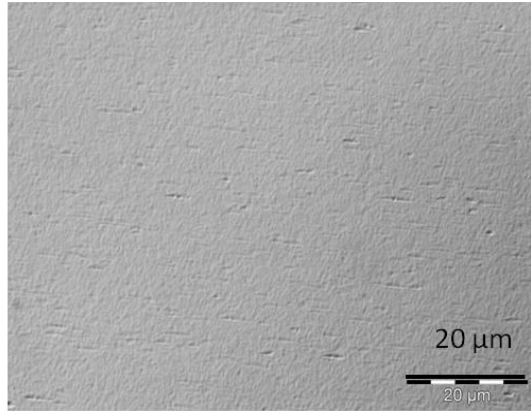
(a)
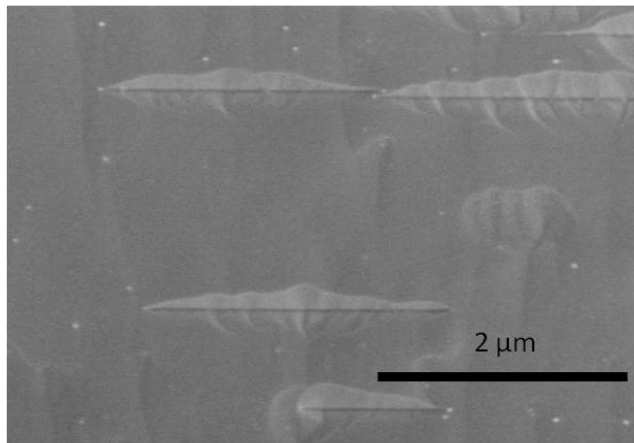
(b)

Figure 5-6: Needle defects in sample SZ100 imaged by (a) Nomarski x100 and (b) SEM x25,000.

Figure 5-7: Void defects observed on a Hg$_{1-x}$Cd$_x$Te imaged by Nomarski x100. Taken from Reference [10].

94
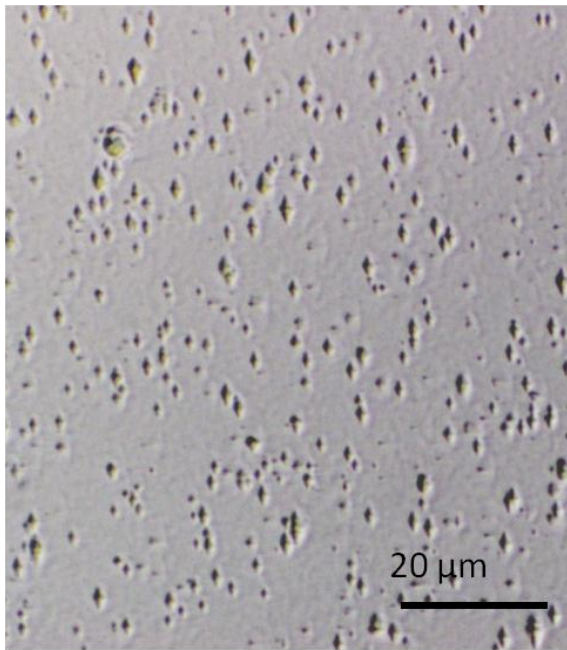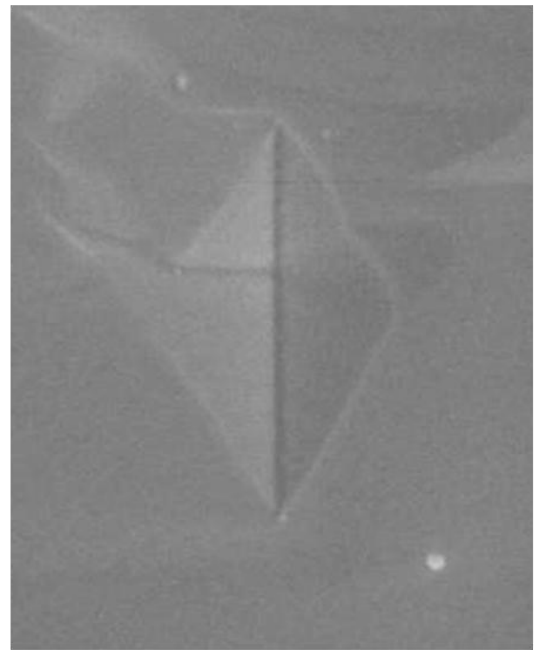
(a)   (b)

Figure 5-8: "Diamond" defects on the surface of sample SZ97 imaged by (a) Nomarksi x100 and (b) SEM x 25,000.
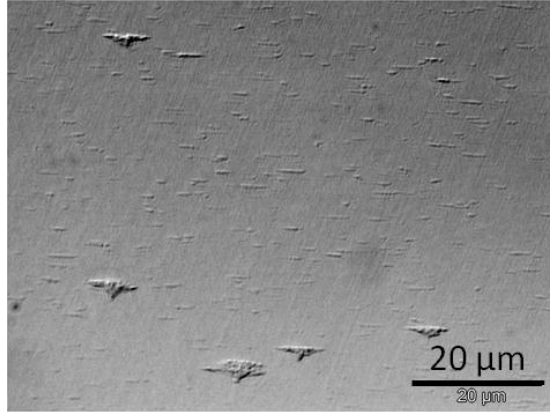
(a)
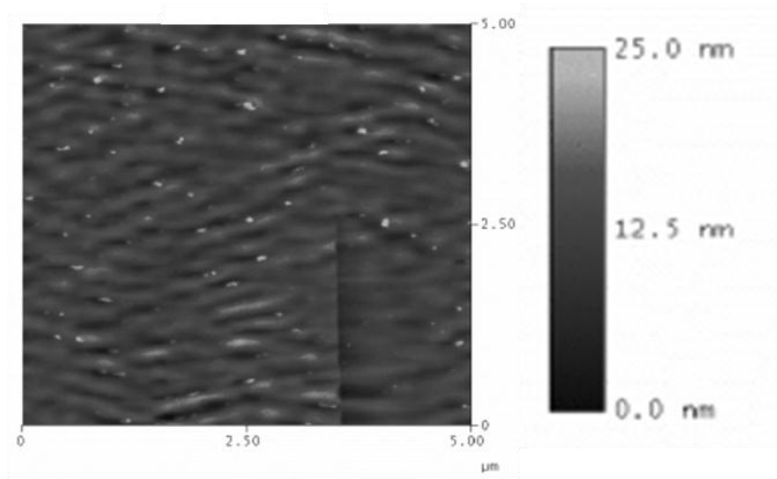
(b)
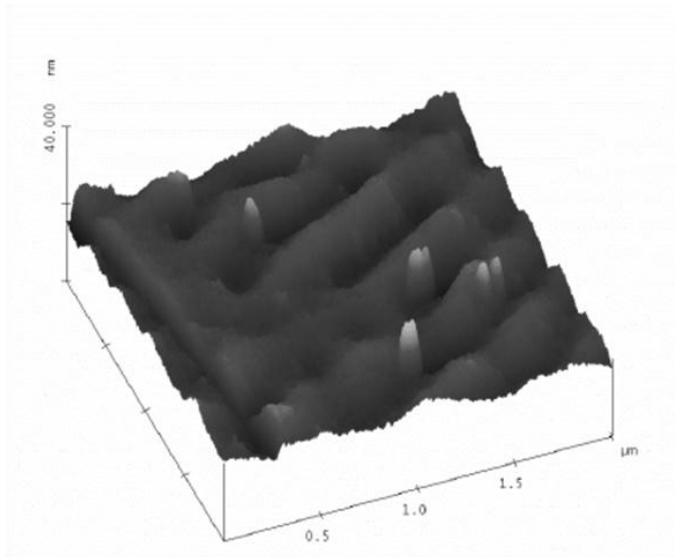
(c)

Figure 5-9: Crosshatch pattern on the surface of sample SZ48 imaged by (a) Nomarski x100 and (b),(c) AFM.

referred to as a crosshatch pattern, and is associated to slippage of certain crystal planes due to misfit dislocation formation or surface strain relief. However, the dislocation defects that produce a crosshatch pattern have not been found to negatively affect device performance, and are usually found on samples with smaller densities of other defects. Thus a visible cross-hatch pattern on a $Hg_{1-x}Cd_xTe$ surface is a sign of high quality growth [49]. Cross-hatch patterns were only observed on a few $Hg_{1-x}Cd_xSe$ samples, all of which were grown with a ~Se_6 flux using the effusion cell as shown in Figure 5-9. AFM measurements also indicated the presence of tiny bumps on the sample surface. The source of these bumps is unclear at this time.

5.2.7   Optimal Growth Conditions

As is the case with $Hg_{1-x}Cd_xTe$, the optimal growth of $Hg_{1-x}Cd_xSe$ appears to largely depend on Hg-incorporation, which results in a balancing act between the substrate temperature and the Hg BEP. Higher substrate temperatures and lower Hg BEPs will result in Hg-deficient growths marked by needle defects and diamond defects (though not void defects like $Hg_{1-x}Cd_xTe$), while lower substrate temperatures and higher Hg BEPs will produce a rougher sample surface. Thus the general approach for determining $Hg_{1-x}Cd_xSe$ MBE growth parameters should be to first optimize the surface morphology by adjusting the substrate temperature and Hg BEP. Once a substrate temperature and Hg BEP that produce smooth surfaces with minimal defects has been selected, the growth rate can be controlled by the Se BEP and the composition by the Cd/SE BEP ratio as described in Section 5.2.3.

The optimal substrate temperature appears to be lower for $Hg_{1-x}Cd_xSe$ than $Hg_{1-x}Cd_xTe$, most likely due to the higher vapor pressure of Se than Te. The optimal substrate temperature window appears to be 90-110 °C for an Hg and Se BEP of 2.5×10^{-4} and 4.0×10^{-6} Torr respectively. Lower temperatures produced a rough surface, and at 110 °C needle defects started

to appear, with needle and diamond defects becoming more prevelant as temperature was further increased. However, in the 90-110 °C window the surface morphology of the $Hg_{1-x}Cd_xSe$ sample mimicked that of the substrate. For the ZnTe/Si substrates, this produced an "orange-peel" surface, but when $Hg_{1-x}Cd_xSe$ was deposited directly onto a GaSb substrate (with a homoepitaxial GaSb layer prepared in another chamber), the smoother GaSb surface morphology produced a smooth surface under these conditions as shown in Figure 5-10. Outside this the 90-110 °C window, $Hg_{1-x}Cd_xSe$ samples grown on both ZnTe/Si and GaSb exhibited the same surface features discussed in Section 5.2.6 [10]. Though samples grown at temperatures between 90 and 110 °C were smoother, only a few had visible cross-hatch patterns.

Unfortunately, the window of optimal growth parameters was not firmly established for $Hg_{1-x}Cd_xSe$ samples grown with the ~Se_2 flux. Prior studies of ZnSe growth with a Se cracker observed that the window of optimal growth parameters was narrower with a cracked Se beam, possibly due to the greater volatility of Se_2 [50]. Only a small number of samples were grown with and ~Se_6 flux using the cracker, none of which were grown under the optimal conditions found with the effusion cell. Further growth will be required to determine the optimal growth window for $Hg_{1-x}Cd_xSe$ grown with ~Se_2 and ~Se_6 using the cracker.
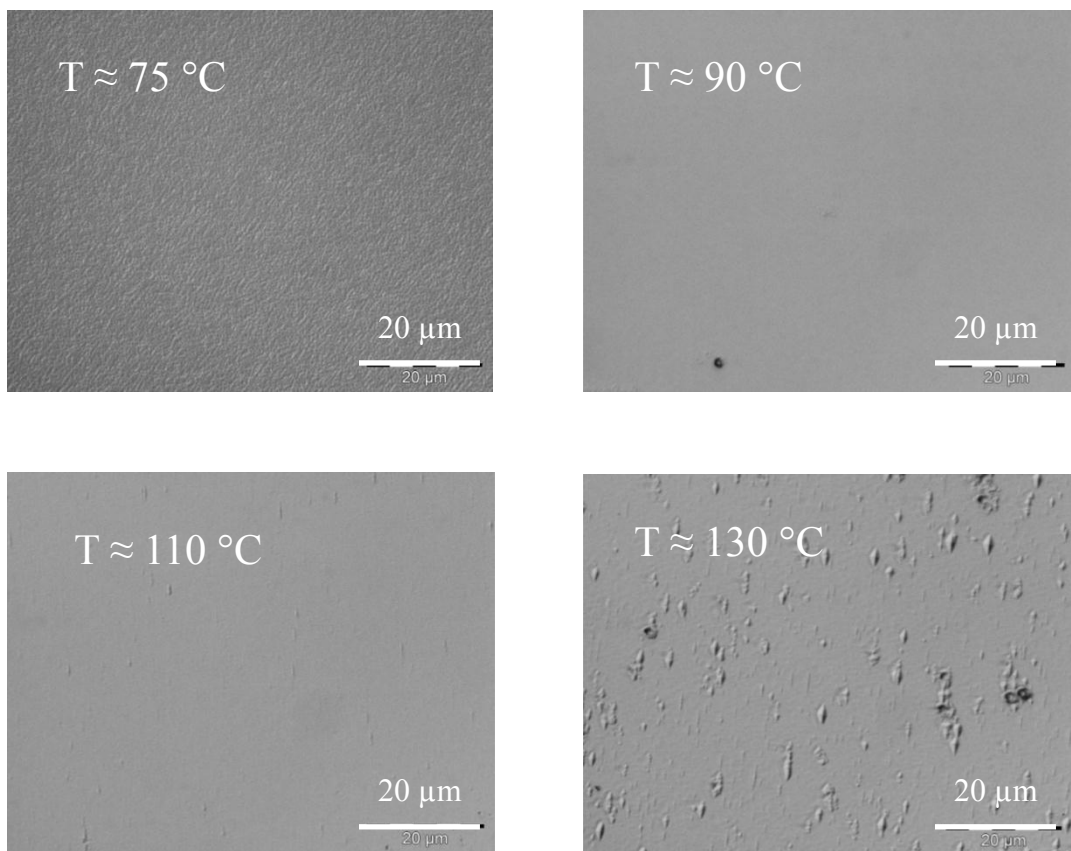
Figure 5-10: Nomarski x100 images of Hg$_{1-x}$Cd$_x$Se samples grown on GaSb substrates various substrate temperatures, with Hg and Se BEP fixed at 2.5x10^{-4} Torr and 4.0x10^{-6} Torr respectively. Taken from Reference [10].

5.3   Electrical Characterization

5.3.1   Background Electron Concentration

The primary obstacle that limited utilization of $Hg_{1-x}Cd_xSe$ in IR devices is the large background electron concentration (n). Previous studies of nominally undoped $Hg_{1-x}Cd_xSe$ grown by the Bridgeman technique [12] and by MBE [14] reported n ranging from 10^{17}-10^{18} cm^{-3}, with no evidence of carrier freeze out for temperatures as low as 4K. Use of $Hg_{1-x}Cd_xSe$ for IR devices will require n to be lowered by at least two orders of magnitude, as well as the development of an effective p-type doping process. At this time, p-type $Hg_{1-x}Cd_xSe$ has not been reported. Prior annealing studies found that the electron concentration of $Hg_{1-x}Cd_xSe$ increased when annealed under Hg overpressures, and decreased under Se overpressures, suggesting that native defects could be generating at least some of the background electrons [12]. A previous study of annealed HgSe samples suggested the possibility of n-type Hg interstitials (Hg_i), n-type Se vacancies (V_{Se}) and p-type Hg vacancies (V_{Hg}) [51].

5.3.2   Charge Carrier Gradients

VFH measurements and QMSA (as described in Section 3.10.2) were performed on some of the $Hg_{1-x}Cd_xSe$ samples to determine if part of the conductivity was due to surface or interfacial charge accumulation layers. Ideally, QMSA of homogeneous n-type samples with specific concentrations and mobilities should display a sharp, narrow peak corresponding to the bulk electrons, plus additional peaks which could represent accumulation layers. Conductivity and carrier concentration vs. mobility as determined by QMSA for a typical $Hg_{1-x}Cd_xSe$ sample, SZ99, are given in Figure 5-11 (a) and Figure 5-11 (b) respectively. While QMSA indicated that the conductivity for the $Hg_{1-x}Cd_xSe$ samples is dominated by a single electron peak, the width of

the primary peak and the presence of secondary peaks are consistent with a gradient in electron mobility and concentration. This would suggest that the electron concentration of the $Hg_{1-x}Cd_xSe$ samples is inhomogeneous, possibly due to gradients of impurities and native defects formed during growth.

MCF was performed on the conductivity tensor components (3-15) and (3-16) as a function of magnetic field as described in Section 3.10.2. This method assumes the charge carriers have discrete mobilities, but QMSA suggests there are actually distributions in both electron mobility and concentration in these samples and so exact fits could not be obtained. Relatively close fits could be obtained assuming two electrons, rewriting (3-15) and (3-16) as

$$\sigma_{xx}(B) = \frac{en_1\mu_1}{1+(\mu_1 B)^2} + \frac{en_2\mu_2}{1+(\mu_2 B)^2} + \sigma_o \qquad (5\text{-}1)$$

$$\sigma_{xy}(B) = -\frac{en_1\mu_1^2 B}{1+(\mu_1 B)^2} - \frac{en_2\mu_2^2 B}{1+(\mu_2 B)^2} \qquad (5\text{-}2)$$

where n_1 and n_2 represent the concentrations of electrons with mobilites of μ_1 and μ_2 respectively. At zero magnetic field ($B = 0$), these electrons would have conductivities of $\sigma_1 = en_1\mu_1$ and $\sigma_2 = en_2\mu_2$. The parameter σ_o represents the conductivity of charge carriers with mobilities too low to determine, as may be expected from interfacial or surface conduction. Figure 5-11 (c) and (d) show MCF of σ_{xx} and σ_{xy} vs B respectively for SZ99, with fitting parameters n_1, n_2, μ_1, μ_2, and σ_o given in Table 5-1. Note that, in this case, σ_o does not play a prominent role.
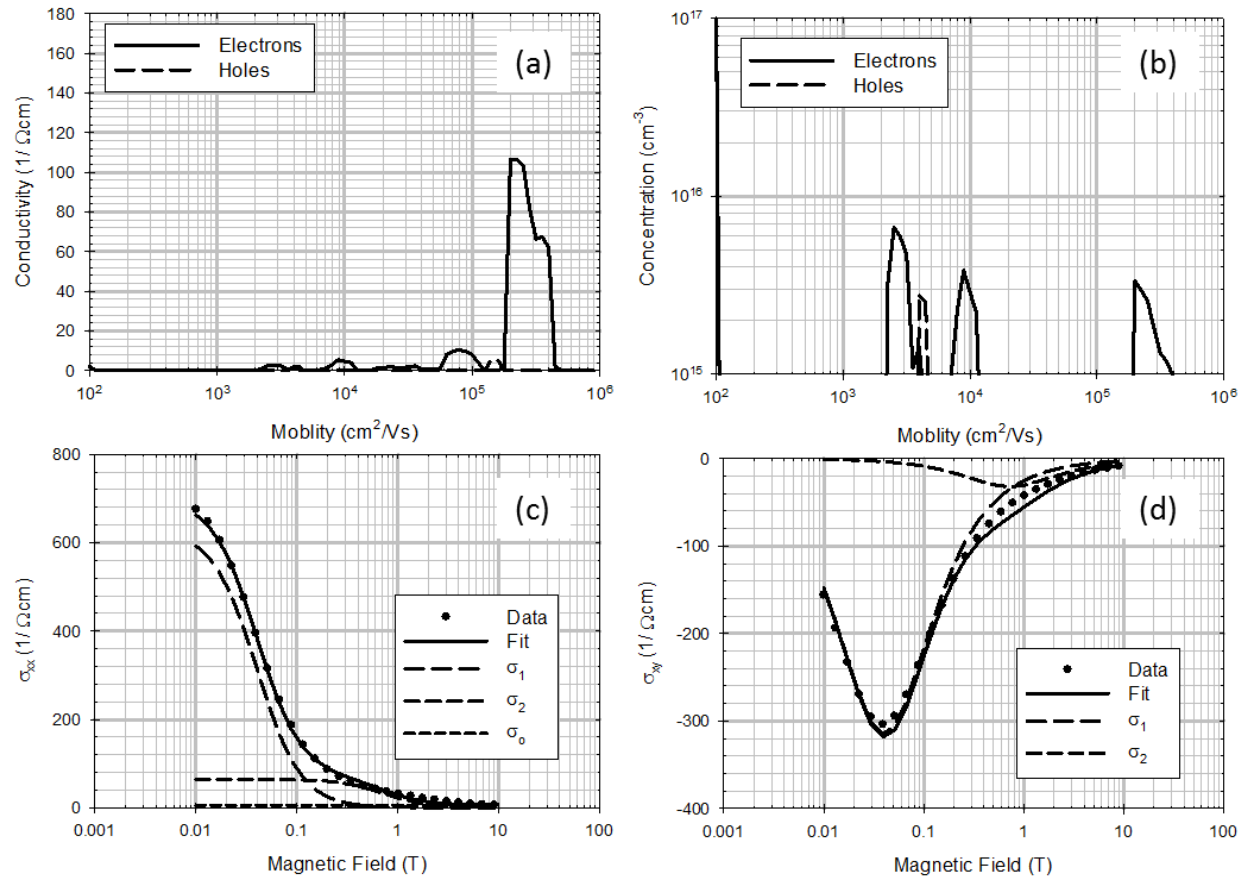
Figure 5-11: Variable field Hall analysis of SZ99 (x=0.138) at 12K: (a) QMSA conductivity vs. mobility, (b) QMSA concentration vs. mobility, (c) MCF σ_{xx} vs. magnetic field using equation (5-1), and (d) MCF σ_{xy} vs. magnetic field using equation (5-2).

i	n_i (x10^{16} cm^{-3})	μ_i (cm^2/ Vs)	σ_i (Ωcm)$^{-1}$
1	1.53	254,401	623.53
2	1.91	20,745	63.52
o	--	--	5.75

Table 5-1: Hall parameters obtained through MCF to σ_{xx} and σ_{xy} vs. magnetic field using equations (5-1) and (5-2) respectively for SZ99 at 12K.

5.3.3 As-Grown Hall Measurements

Single field Hall measurements were performed on all samples with a magnetic field of 0.1 Tesla to determine average electron concentration n and mobility μ. However, for samples with low x-values (and thus narrow bandgaps) the mobility is so large that the conductivity varies significantly with magnetic field around 0.1 T as seen in Figure 5-11 (c). As a result, the Hall coefficient is not linear at 0.1 T for samples with low x-values, and so a single-field measurement is insufficient to determine n. For samples with $x<0.18$, MCF to VFH measurements were performed as described in Section 5.3.2, and the overall concentration was taken to be the sum of the concentrations of the two carriers ($n = n_1 + n_2$).

Figure 5-12 shows n vs. bandgap for $Hg_{1-x}Cd_xSe$ samples grown with the two different Se sources. Initially, the $Hg_{1-x}Cd_xSe$ samples grown with the 5N Se effusion cell had similar n to that previously reported by other groups, with no clear relationship to any of the growth parameters. However, when the 6N Se cracker was employed, a significant decrease was immediately observed in the as-grown concentration to $n \sim 7 \times 10^{16}$ cm^{-3} at 77K, again with little clear relationship to growth parameters. There was little variation in n-type carrier concentration with x-value. Mobility, given in Figure 5-13, showed a trend similar to that expected for $Hg_{1-x}Cd_xTe$ with similar composition and doping, although a factor of ~5 lower than that expected for low-doped $Hg_{1-x}Cd_xTe$.

The predicted $Hg_{1-x}Cd_xTe$ mobility given in Figure 5-13 was determined by using Matheson's principle to combine the Rosbeck model for low-doped $Hg_{1-x}Cd_xTe$ [52] and the Brooks-herring model for ionized impurity scatting [44]. The 77K electron mobility for the $Hg_{1-x}Cd_xSe$ samples appeared to correspond to the predicted mobility for $Hg_{1-x}Cd_xTe$ with $n = 7 \times 10^{16}$ cm^{-3} and an ionized impurity density (N_i) of 1.7×10^{17} cm^{-3}. Measurements down to 12K
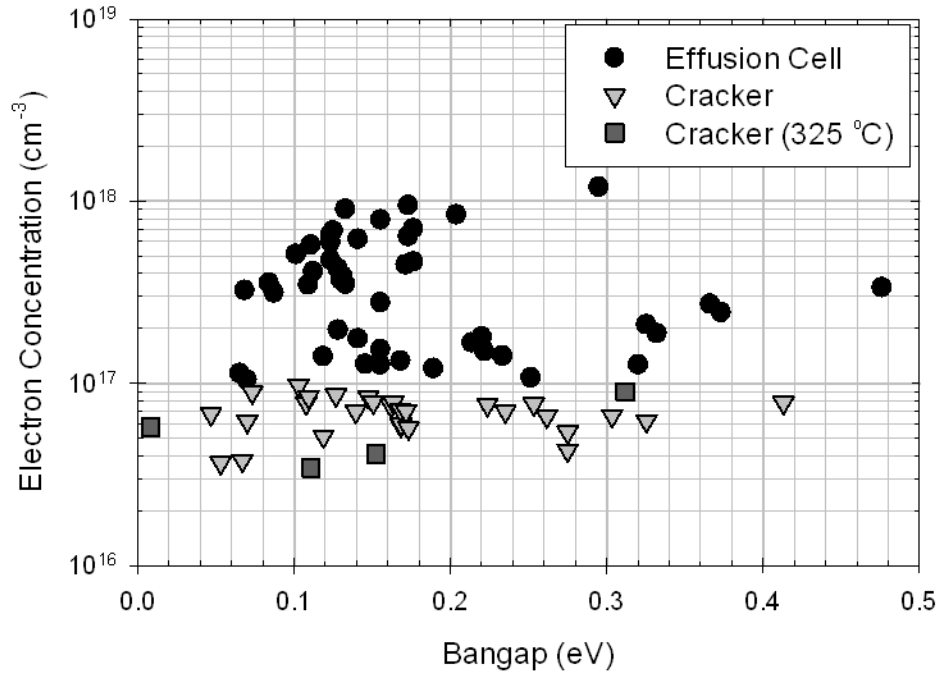
Figure 5-12: As-grown electron concentration vs. energy bandgap at 77K for Hg$_{1-x}$Cd$_x$Se samples grown with the effusion cell (5N ~Se$_6$), the cracker (6N ~Se$_2$) and the cracker with the cracking zone lowered to 325 °C (6N ~Se$_6$).
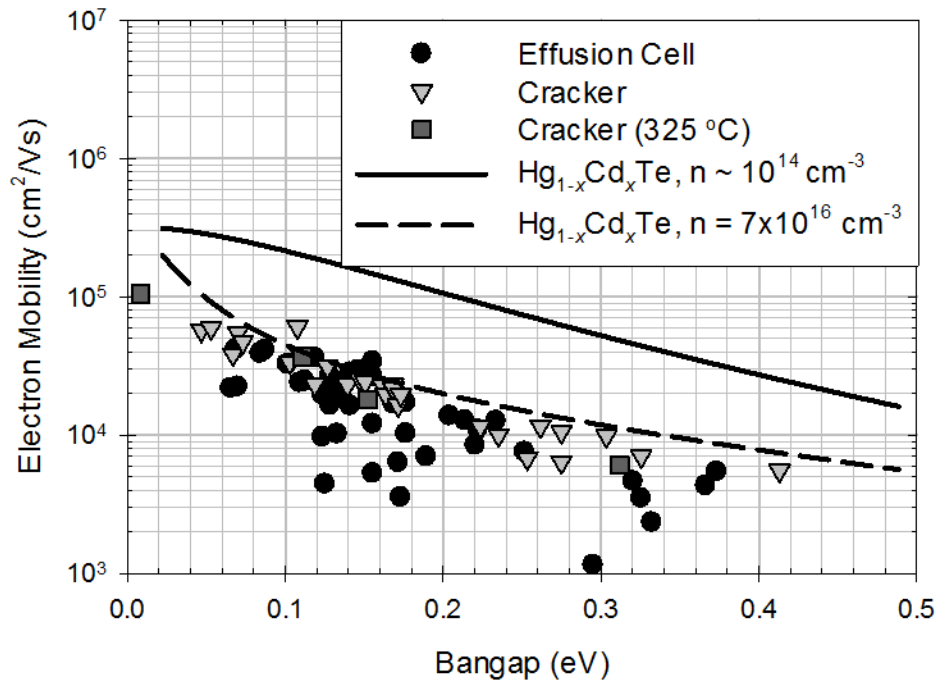
Figure 5-13: As-grown electron mobility vs. energy bandgap at 77K for Hg$_{1-x}$Cd$_x$Se samples grown with the effusion cell (5N ~Se$_6$), the cracker (6N ~Se$_2$) and the cracker with the cracking zone lowered to 325 °C (6N ~Se$_6$). Also included is the predicted 77K Hg$_{1-x}$Cd$_x$Te mobility for both low doping (n~10^{14} cm^{-3}), and for n = 7x10^{16} cm^{-3}, N_i = 1.7x10^{17} cm^{-3}.

104
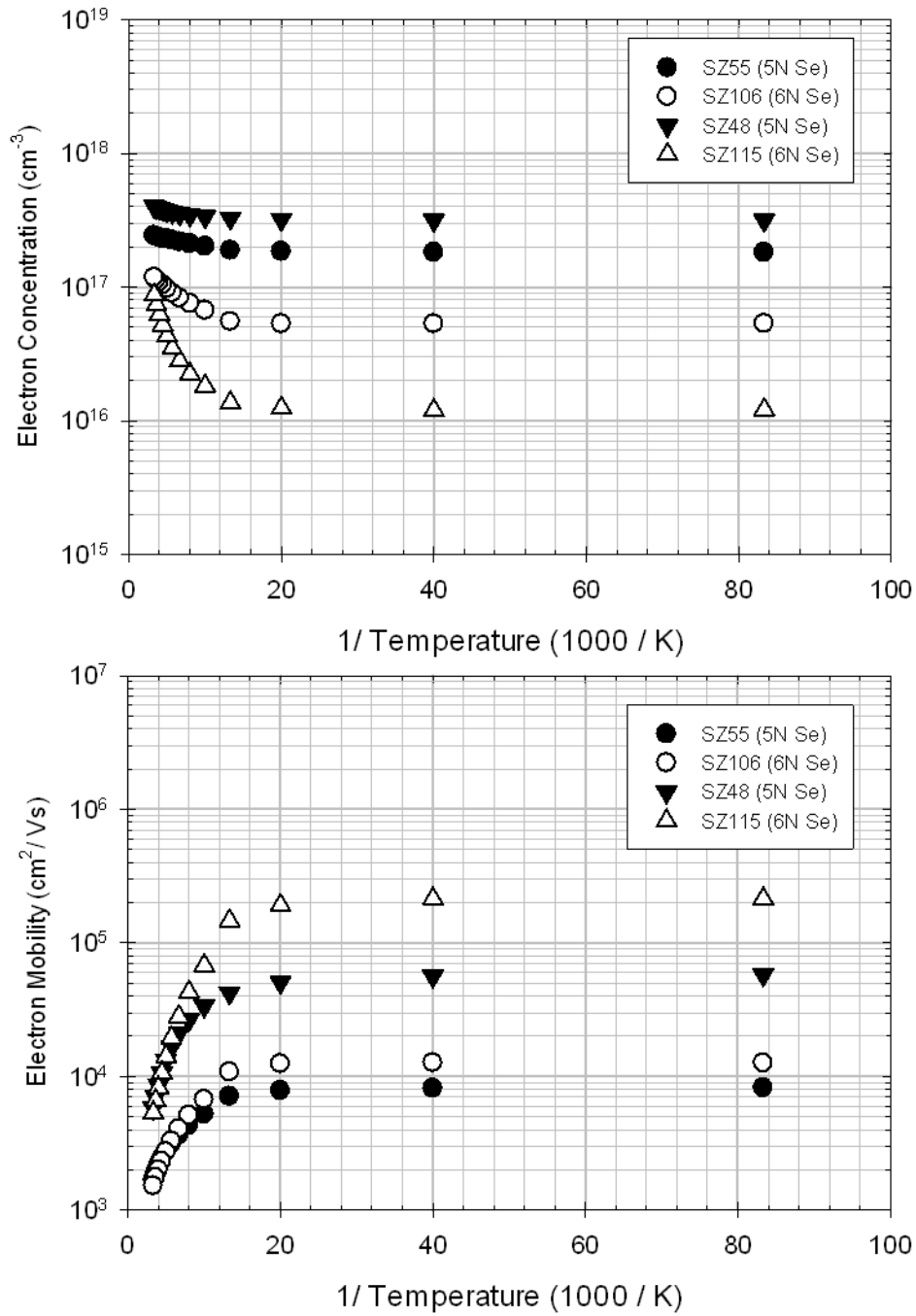
Figure 5-14: As-grown electron concentration (Top) and mobility (Bottom) vs. inverse temperature for samples grown with 5N Se (SZ55 *x* = 0.33, SZ48 *x* = 0.16), and 6N Se (SZ106 *x* = 0.28, SZ115 *x* = 0.15).

saw a continuing reduction of n, in some cases by an order of magnitude, as shown in Figure 5-14. Two possible explanations were proposed to explain this change: either the ~Se_2 flux was producing fewer native donor defects in the as-grown material than the ~Se_6 flux from the effusion cell, or the 6N Se material loaded into the cracker was introducing fewer impurities than the 5N Se material loaded into the effusion cell.

In order to determine whether this reduction in n was due to the 6N material or the ~Se_2 flux, the cracking zone temperature was lowered to 325 °C. 325 °C is the same temperature as the hot zone of the effusion cell as measured by a thermocouple, and BFM measurements suggest that this temperature produces a predominantly Se_2 beam as explained in Section 2.2.2.2. When the cracking zone temperature was lowered to 325 °C, the concentration remained equally low, strongly suggesting the reduction in n was due to the lower impurity content in the 6N source material.

5.3.4   Impurities

The reduction in n observed by switching from 5N to 6N Se both under cracking and non-cracking conditions indicates that impurities from the Se source material are a significant source of the high background concentration. Two other possible sources of impurities considered were contaminants in the Hg and Cd source material. However, $Hg_{1-x}Cd_xTe$ samples are also grown in the II-VI deposition chamber at ARL using the same Hg source. These $Hg_{1-x}Cd_xTe$ samples do not have the same electron background doping problems, and so contaminants in the Hg source material do not appear to be a significant source of impurities. The Cd source material was considered a more likely source of impurities, as it has the same 5N purity as the Se material in the effusion cell. To determine the concentration of electrons generated by Cd material contaminants, an $Hg_{0.69}Cd_{0.31}Te$ sample (TC136) was grown using the

same Cd source to determine the concentration of electrons generated by Cd material contaminants.

After annealing TC136 under Hg to remove V_{Hg}, the sample had an electron concentration of 5.4×10^{14} cm^{-3} at low temperatures, as shown in the Arrhenius plot given in Figure 5-15. This electron concentration is nearly two orders of magnitude lower than typically found in the $Hg_{1-x}Cd_xSe$ samples even after annealing under Hg, then Se (as discussed in Section 5.3.5), which would suggest that the Cd source material is not a significant source of background impurities. SIMS measurements, as described in Section 3.11, were performed on sample TC136 and certain as-grown $Hg_{1-x}Cd_xSe$ samples in order to identify any impurities. These SIMS measurements are given in Figure 5-16 (sample TC136), Figure 5-17 (sample SZ80, $x = 0$, grown with 5N Se), Figure 5-18 (sample SZ43, $x = 0.183$, grown with 5N Se), and Figure 5-19 (sample SZ119, $x = 0.211$, grown with 6N Se).

All samples revealed the presence of carbon (C), oxygen (O), bromine (Br), and chlorine (Cl) concentrated at the interface with the ZnTe buffer layer. Br and Cl could be introduced during the chemical etching process performed on substrates immediately prior to loading into the UHV buffer line, and the C and O could be a sign that some CO_2 is still present on the substrate surface after the oxide desorption process. Curiously, C and O, and Si were also observed in the top ~1.5 μm from the surface of SZ80, SZ43, and SZ119. S was observed in all samples. At this time, neither the origin of these elements nor their electrical activity is known. The C and O could possibly be in-diffusing from the atmosphere after growth, as has been observed in other materials. If so, cap layers may be needed to protect the samples from in-diffusion of atmospheric contaminants.
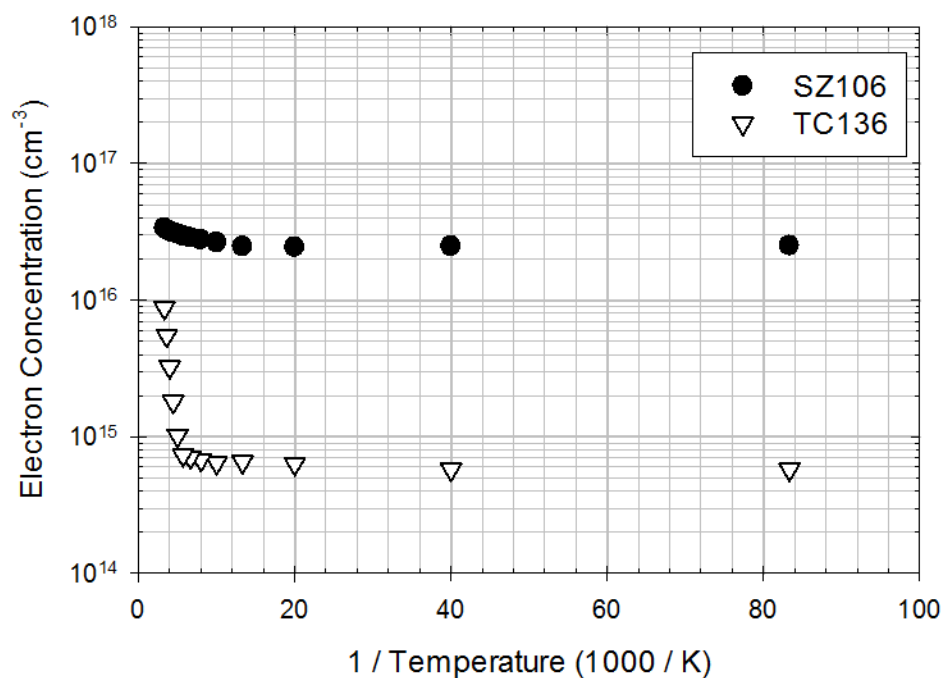
Figure 5-15: Electron concentration vs. inverse temperature for SZ106 ($Hg_{0.72}Cd_{0.28}Se$) after annealing for 24 hours at 250 °C under Hg, then Se and TC136 ($Hg_{0.69}Cd_{0.31}Te$) after annealing under Hg for 24 hours at 250 °C.
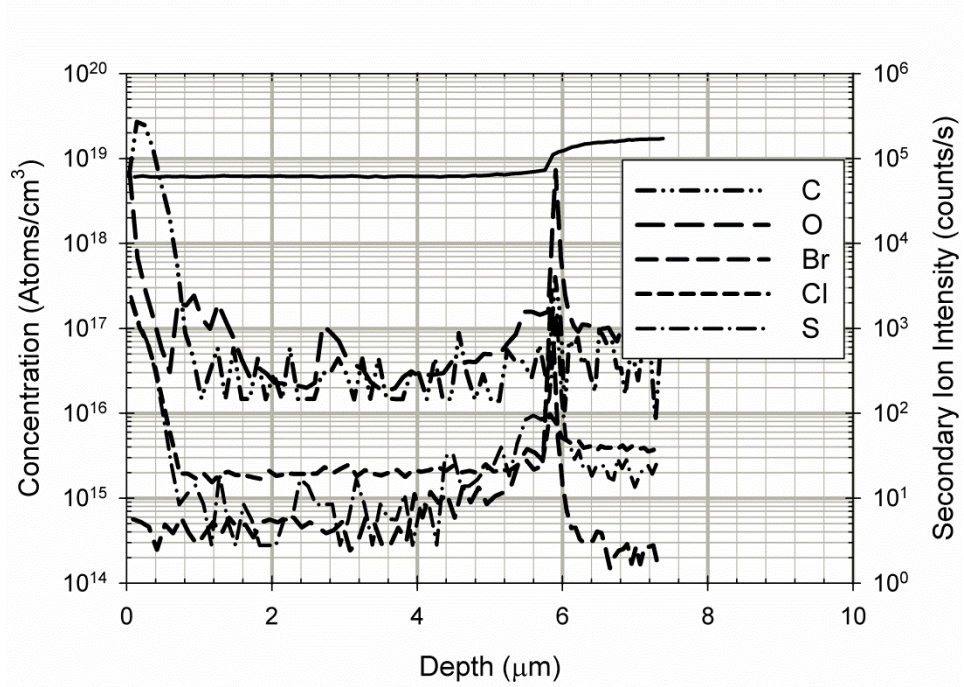
Figure 5-16: SIMS measurement of TC136 (Hg$_{0.69}$Cd$_{0.31}$Te sample grown with 5N Cd source).
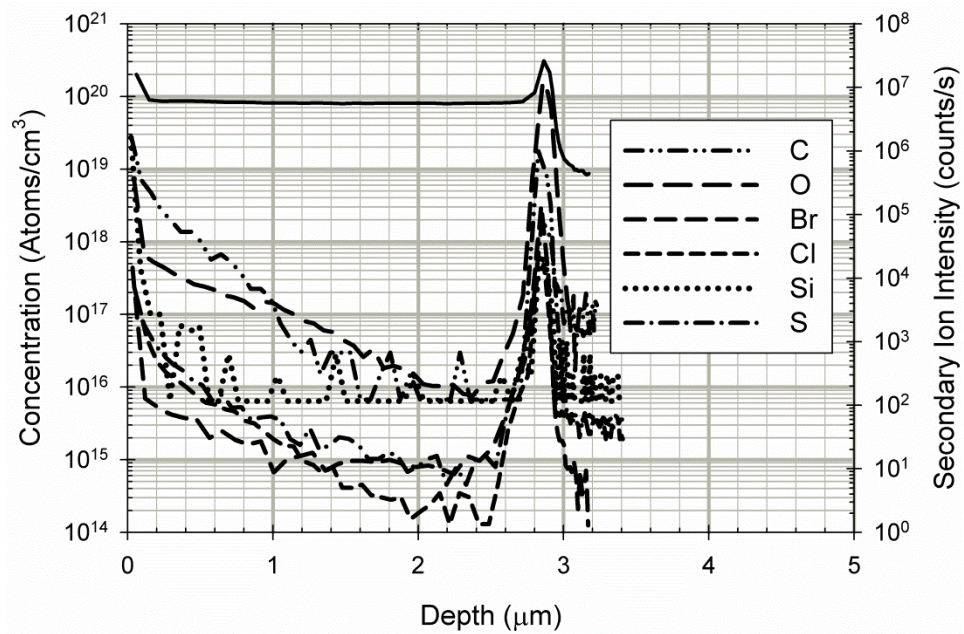
Figure 5-17: SIMS measurement of SZ80 (HgSe sample grown with 5N Se).
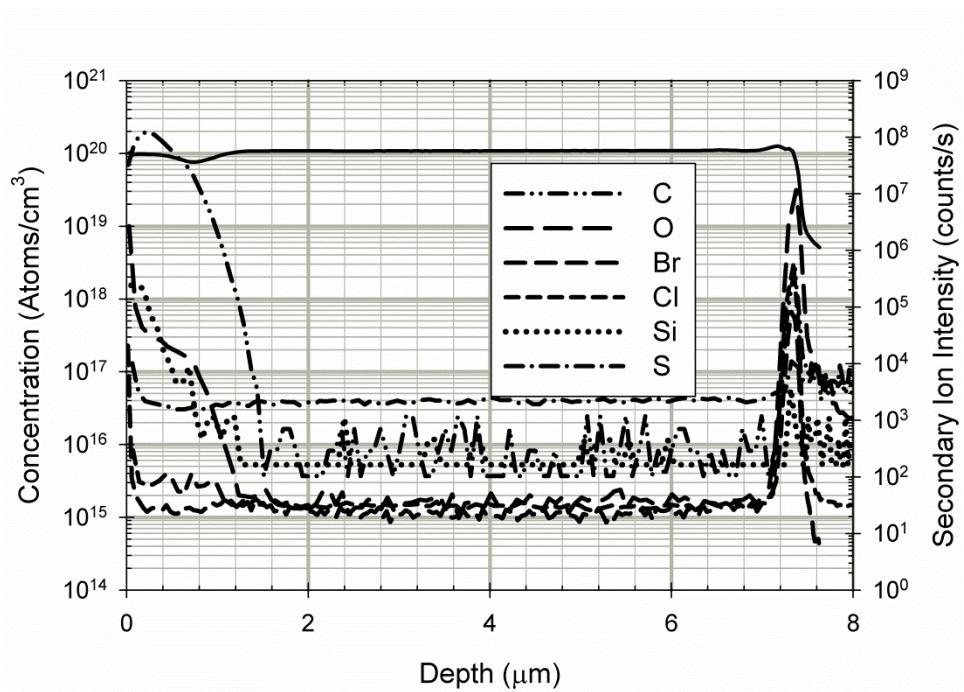
Figure 5-18: SIMS measurement of SZ43 (Hg$_{0.82}$Cd$_{0.18}$Se grown with 5N Se).
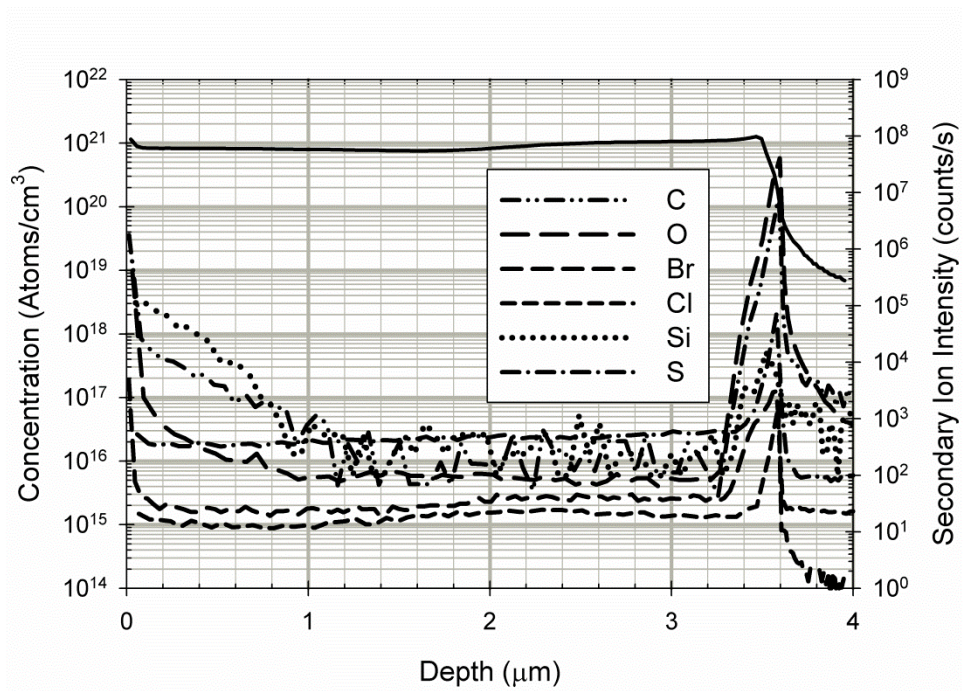
Figure 5-19: SIMS measurement of SZ119 (Hg$_{0.79}$Cd$_{0.21}$Se grown with 6N Se).

5.3.5 Annealing

Anneals were performed in quartz ampoules. Prior to the anneal, the quartz ampoules were etched in HF, pumped out to a vacuum of $\sim 10^{-5}$ Torr with a series of scroll and sorption pumps, and heated under a low flame to remove remaining water vapor. The samples and material were then loaded into the ampoule which was sealed with a blow torch. The surfaces of each sample were cleaned with an acetone spray, after which the sample was briefly submerged in acetone and isopropanol and then dried with N_2 gas before being loaded. Once sealed, the ampoule was placed in a furnace made by Lindberg. Most anneals were performed over 24 hours at 250 °C, followed by a 3 hour cool-down to room temperature as a baseline. While a few samples were annealed at different temperatures for different durations, all anneals ended with a 3 hour cool-down to room temperature.

5.3.6 Native Defects

The presence of V_{Hg} in as-grown $Hg_{1-x}Cd_xTe$ is well established. As described in Section 5.1, the high vapor pressure of Hg makes stoichiometric growth of Hg-based compounds difficult, and $Hg_{1-x}Cd_xTe$ samples typically possess a large number of V_{Hg} as a result. These V_{Hg} act as acceptors, and so a post-growth anneal under an Hg overpressure is typically employed to fill the V_{Hg} in order to achieve n-type $Hg_{1-x}Cd_xTe$ [3]. Previously PAS measurements (as described Section 3.12) have been used to detect V_{Hg} in $Hg_{1-x}Cd_xTe$ [37]. PAS measurements were performed in collaboration with Washington State University—Pullman. While these measurements could not give absolute vacancy concentrations, changes in the relative vacancy concentrations were determined by comparing the PAS shape parameter (S) between as-grown and annealed samples.

Figure 5-20 shows the PAS measurement of a test sample of In-doped $Hg_{1-x}Cd_xTe$, which saw a clear reduction in S after annealing under Hg that corresponds to the increase in n measured by Hall at 77K. This suggests reduction in V_{Hg} as expected. Similar measurements of an $Hg_{1-x}Cd_xSe$ sample given in Figure 5-21 also indicated a reduction in V_{Hg} after Hg-annealing, strongly suggesting the presence of p-type V_{Hg} in $Hg_{1-x}Cd_xSe$. Unfortunately, this technique is not sensitive to n-type vacancies, and so no firm conclusions could be drawn about the presence of V_{Se}. Access to the PAS system was limited, and so only a handful of samples could be measured.

$Hg_{1-x}Cd_xSe$ samples annealed under Hg for 24 hours at 250 °C showed an increase in n, which is consistent with previous studies [12], and PAS suggests that a part (but not all) of this increase is due to V_{Hg} being filled during the anneal. The typical increase in n, however, was much larger than expected and may also be due to V_{Se} formation. Figure 5-22 gives the n and μ vs. bandgap for samples annealed under Hg and Cd overpressures. Annealing under Hg and Cd both increased n and decreased μ, with a larger change observed for samples with lower x-values (and therefore bandgaps). While PAS indicates a decrease in p-type vacancies after Hg-annealing, no observable change was observed in PAS after Cd-annealing as shown in Figure 5-23. However, RBS measurements as described in Section 3.13 of thin (~1800 Å) $Hg_{1-x}Cd_xSe$ samples (SZ126 and SZ128) given in Figure 5-24 indicated a significant increase in surface x-value (and therefore Cd-composition) after Cd-annealing.

RBS measurements given in Table 5-2 after other anneals besides Cd saw no significant change in composition. EDX measurements of SZ103 (3.8 μm thick) and SZ116 (5.1 μm thick) given in Table 5-3 saw no significant change in x-value after Cd-annealing, suggesting that Cd-annealing only increases the x-value within ~2000 Å from the surface. While no change was observed in surface x-value for any other anneal, RBS did indicate some inter-diffusion of Zn
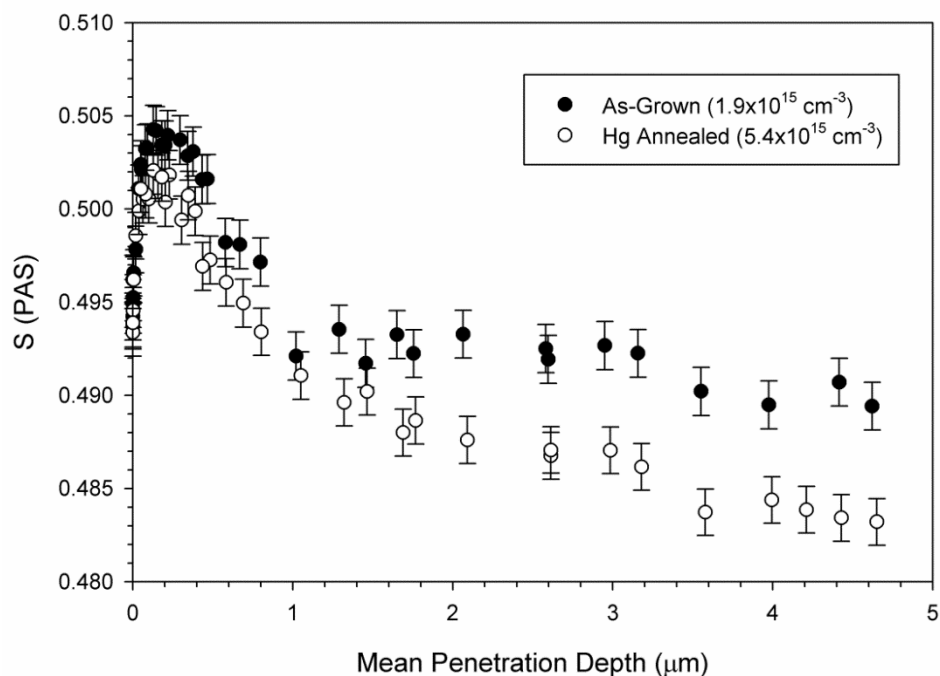
Figure 5-20: PAS measurement of MC51 (Hg$_{0.56}$Cd$_{0.44}$Te grown by ARL) both as-grown and after annealing under Hg, with the corresponding 77K electron concentration. Anneal was for 24 hours at 250 °C.
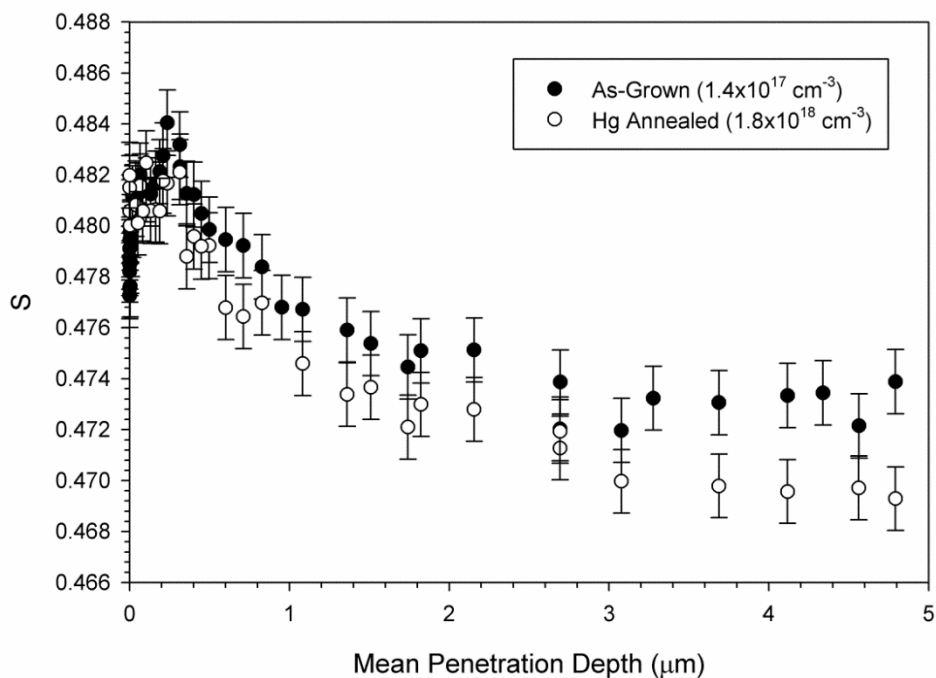
Figure 5-21: PAS measurement of SZ57 (Hg$_{0.75}$Cd$_{0.25}$Se, grown with 5N Se) both as-grown and after annealing under Hg, with the corresponding 77K electron concentration. Anneal was for 24 hours at 250 °C.

113
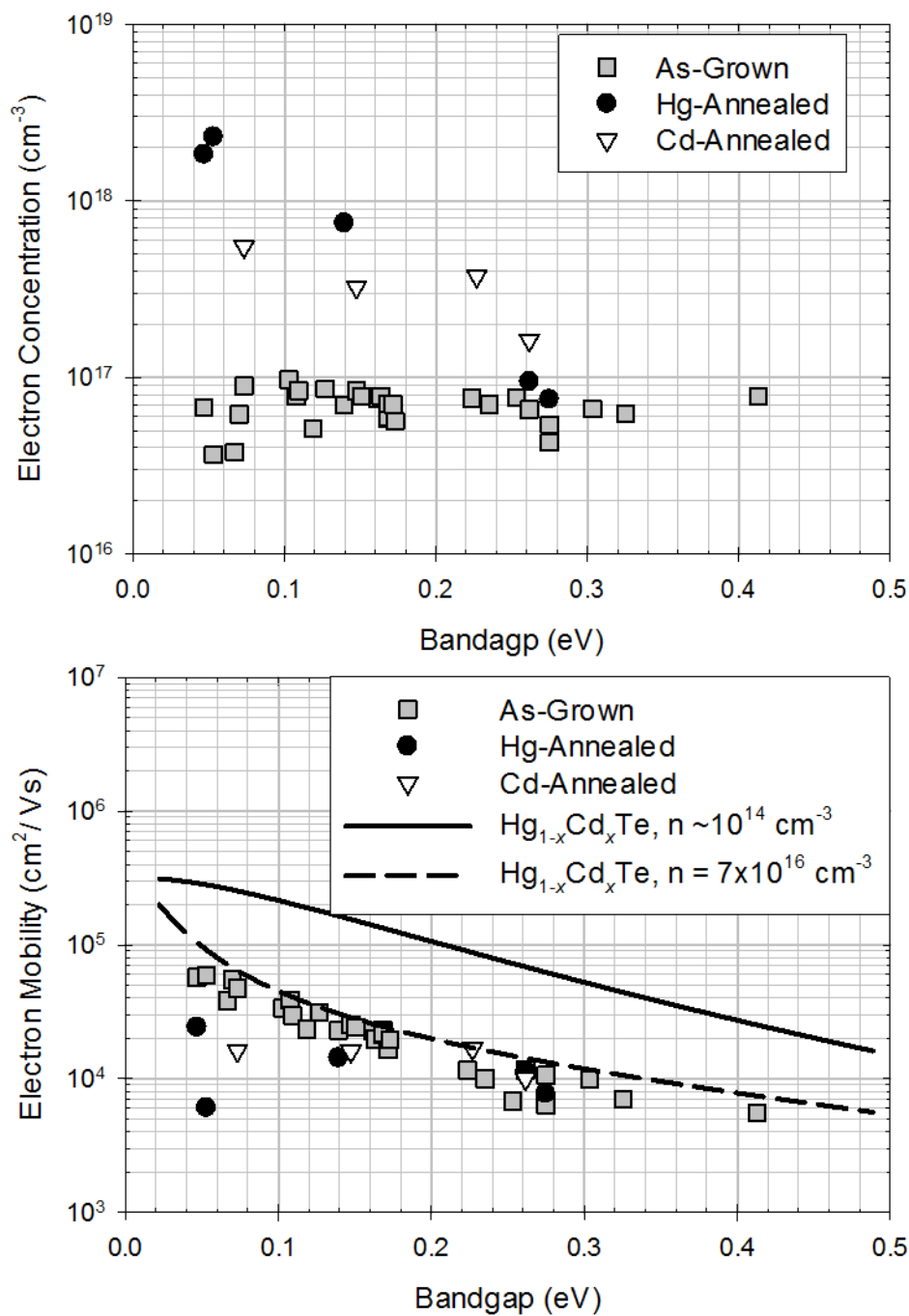
Figure 5-22: Electron concentration (Top) and mobility (Bottom) at 77K vs. bandgap for as-grown, Hg-annealed, and Cd-annealed Hg$_{1-x}$Cd$_x$Se samples grown with 6N Se, along with predicted 77K Hg$_{1-x}$Cd$_x$Te mobility for both low doping ($n \sim 10^{14}$ cm^{-3}), and $n = 7 \times 10^{16}$ cm^{-3}, $N_i = 1.7 \times 10^{17}$ cm^{-3}. Anneals were for 24 hours at 250 °C.
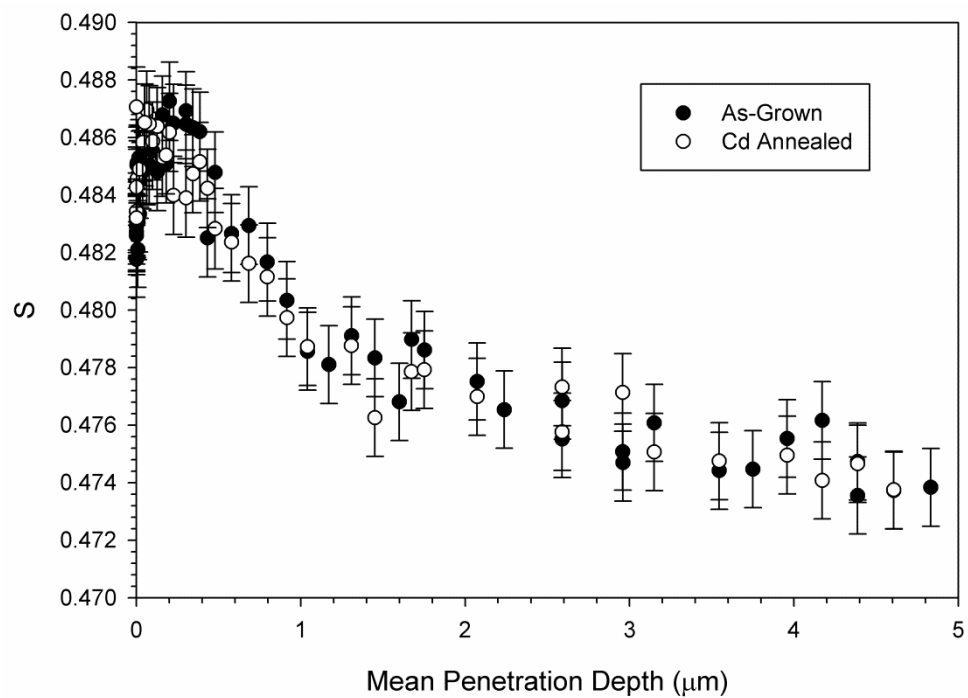
Figure 5-23: PAS measurement of SZ53 ($Hg_{0.80}Cd_{0.20}Se$ grown with 5N Se) both as-grown and after Cd annealing. Anneal was for 24 hours at 250 °C.
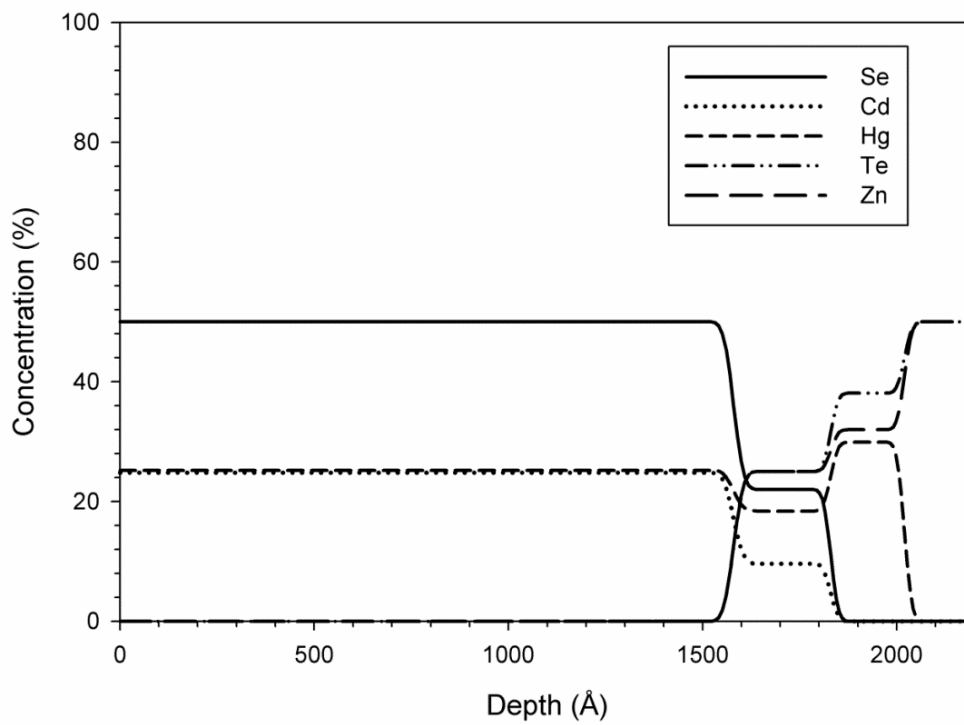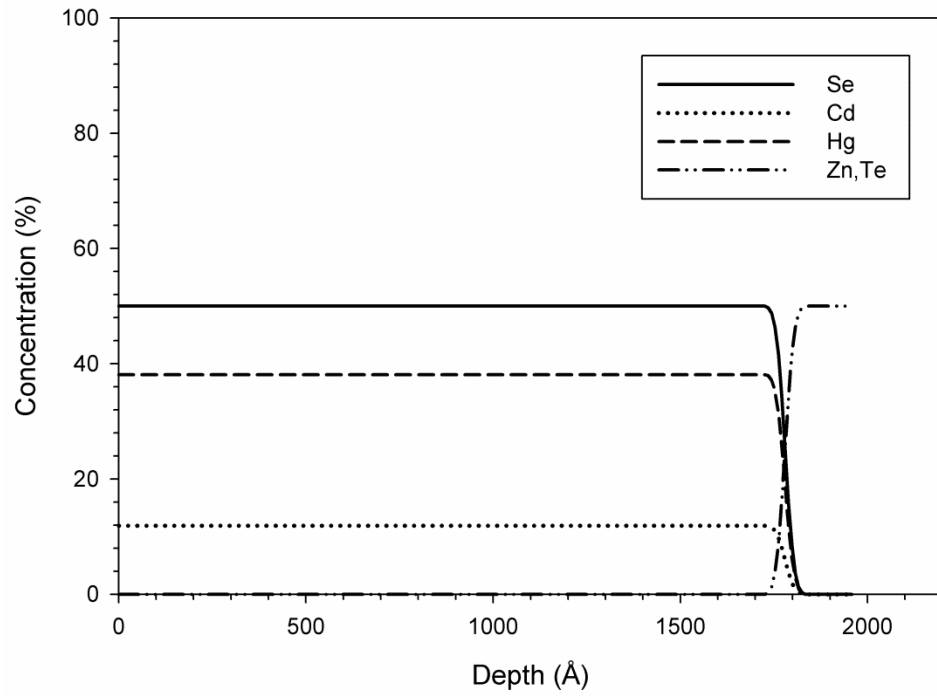
Figure 5-24: RBS depth profile of SZ126 as-grown (Top) and after annealing under Cd for 24 hours at 250 °C (Bottom).

116

Sample Name	Anneal	% Hg	% Cd	x-value (RBS)
SZ126	As-Grown	38.1	11.9	0.24
SZ126	Hg	36.5	13.5	0.27
SZ125	Se	37.9	12.1	0.24
SZ126	Cd	25.2	24.8	0.50
SZ128	As-Grown	35.8	14.2	0.28
SZ128	Hg	34.7	15.3	0.31
SZ128	Se	36.2	13.8	0.28
SZ128	Cd	29.2	20.8	0.42

Table 5-2: *x*-value calculations from RBS measurements after various anneals of SZ126 and SZ128.

Sample	Anneal	% Se	% Hg	% Cd	EDX x-value	FTIR x-value
SZ103	As-Grown	50.91	36.06	13.03	0.260	0.268
SZ103	Cd-Annealed	50.68	35.48	13.83	0.276	0.268
SZ116	As-Grown	50.78	38.62	10.6	0.212	0.207
SZ116	Cd-Annealed	50.78	36.63	10.59	0.212	0.207

Table 5-3: EDX measurements of SZ103 and SZ116 both as-grown and after annealing under Cd for 24 hours at 250 °C, and a comparison of the *x*-values derived from EDX and FTIR.

and Te roughly 20 nm into the $Hg_{1-x}Cd_xSe$ layer after annealing.

Figure 5-25 gives n and μ after annealing under vacuum and Se. Vacuum anneals did not produce an appreciable change in the n, suggesting that $Hg_{1-x}Cd_xSe$ is reasonably stable against decomposition and that the point defect distribution is likely determined by near vacuum conditions during growth. Further experiments are required to definitively confirm this. The lowest values for n were obtained by annealing under Se, with a greater decrease observed in samples with lower x-values with an average value $3x10^{16}$ cm^{-3}. The Se-annealed samples also saw a slight increase in μ, which appeared to correspond to the predicted mobility of $Hg_{1-x}Cd_xTe$ with $n = 3x10^{16}$ cm^{-3} and $N_i = 7x10^{16}$ cm^{-3}.

It was suggested that the equilibrium concentration of V_{Se} with Se vapor in $Hg_{1-x}Cd_xSe$ would decrease at lower temperatures, and so in addition to the standard 250 °C/24 hour anneals, Se anneals were also performed at 100 °C in addition to the standard 250 °C anneals. 100 °C anneals were initially performed over 24 hrs, and then annealing time was increased to 40 days to allow more time for the Se to incorporate at this lower temperature. Finally, in order to reduce both V_{Hg} and V_{Se}, samples were subjected to two 250 °C/24 hour anneals, one under Hg and then one under Se. The resulting n and μ after these anneals are given in Figure 5-26.

In general, the Se-annealed electron concentration appeared to reach a minimum of $n = 3$-$5x10^{16}$ cm^{-3} at 77K regardless of what parameters were used. PAS suggests that annealing under Se created V_{Hg}, particularly in HgSe and low x-value $Hg_{1-x}Cd_xSe$ as shown in Figure 5-27, and thus the reduction in n could be due to a combination of reduced n-type V_{Se} and increased compensating p-type V_{Hg}. However, one sample (SZ106) that had been annealed under Hg then Se was found to have both a lower V_{Hg} signature and a lower n as shown in Figure 5-28, strongly suggesting that in this case the lower concentration was unrelated to V_{Hg} and perhaps could be attributed to the filling of V_{Se}.
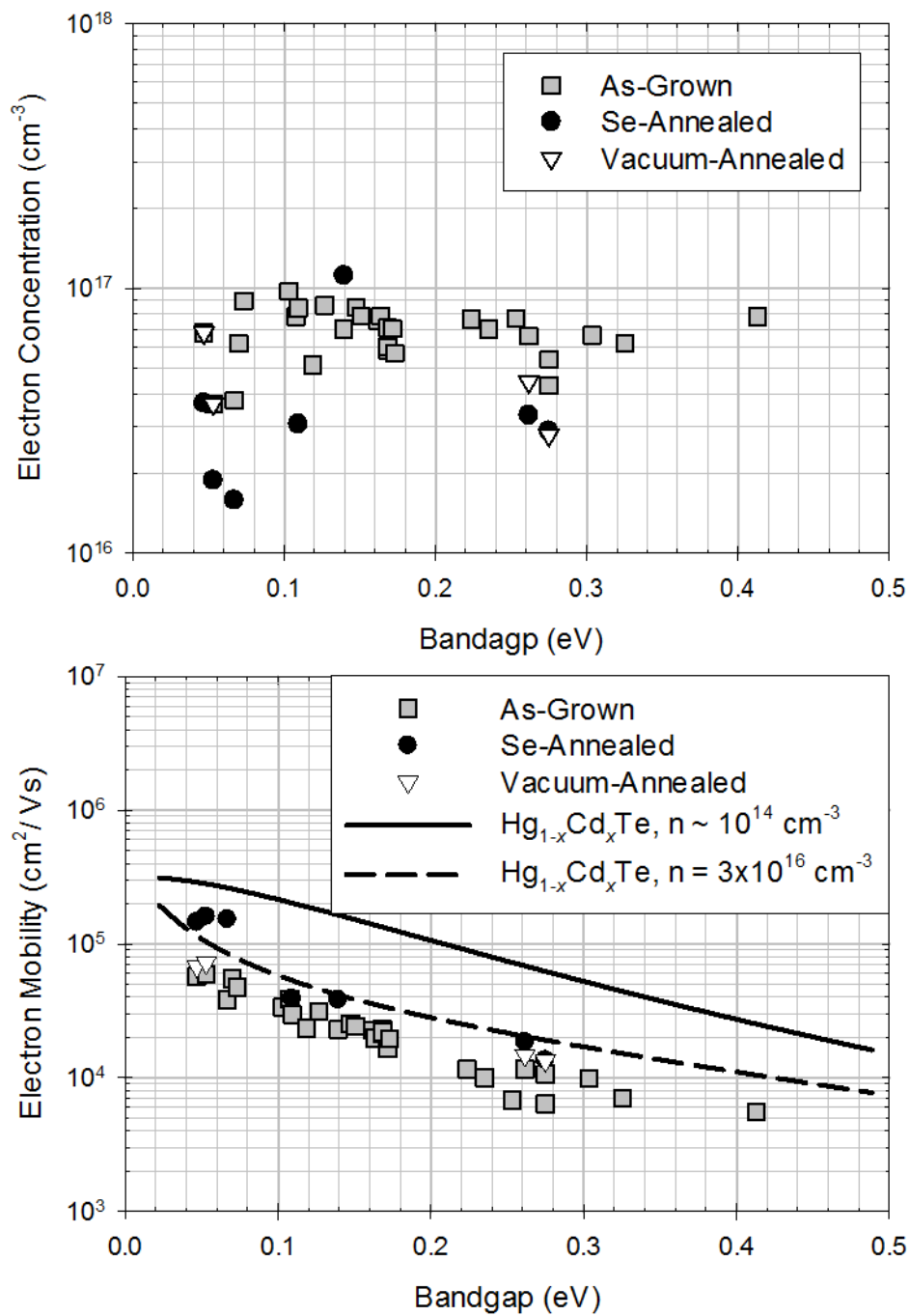
Figure 5-25: 77K electron concentration (Top) and mobility (Bottom) of Hg$_{1-x}$Cd$_x$Se samples grown with 6N Se vs. bandgap, as-grown and after annealing under Se and vacuum for 24 hours at 250 °C, and the predicted 77K Hg$_{1-x}$Cd$_x$Te mobility for both low doping ($n\sim10^{14}$ cm^{-3}) and $n = 3$x10^{16} cm^{-3} and $N_i = 7$x10^{16} cm^{-3}.
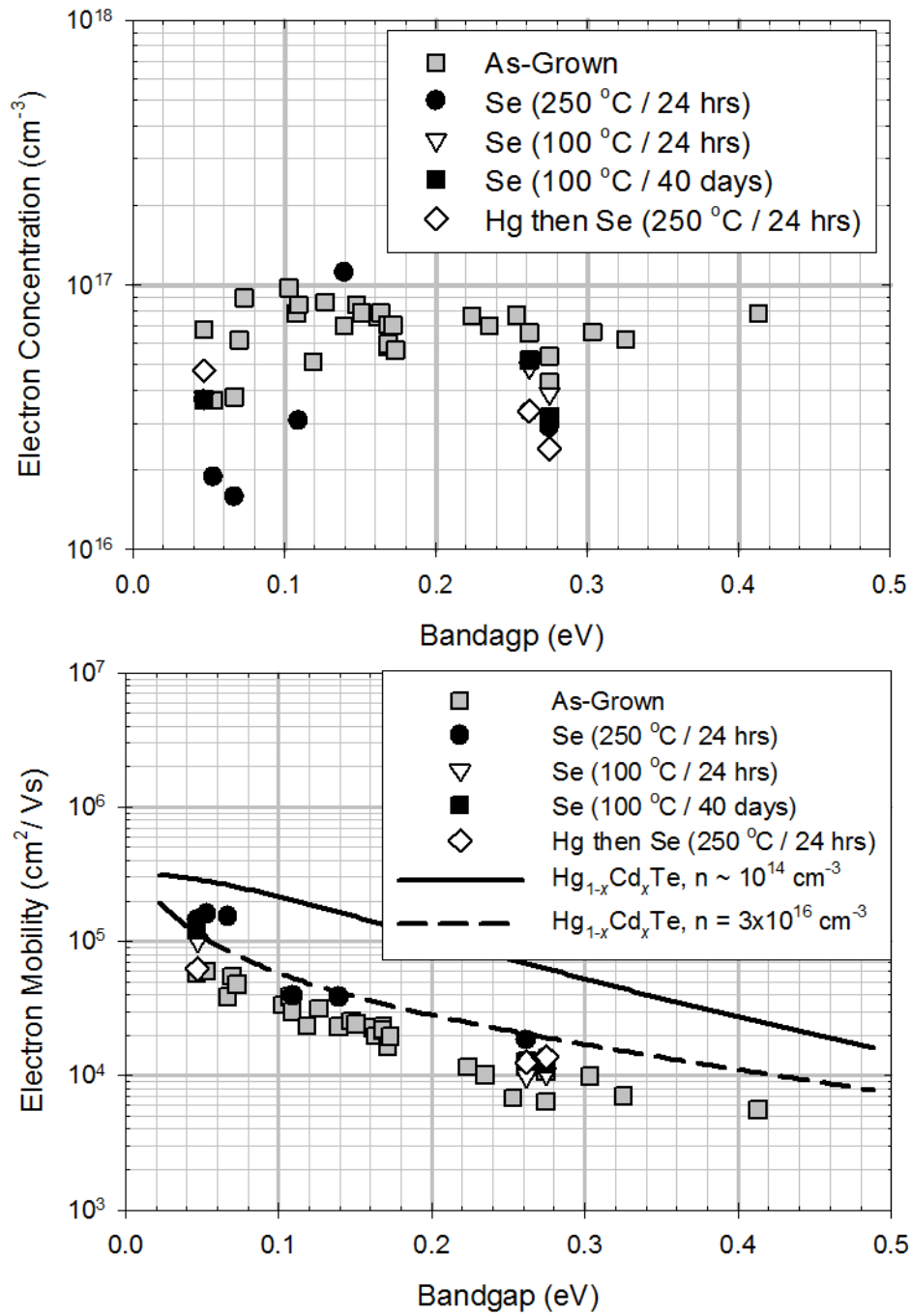
Figure 5-26: 77K electron concentration (Top) and mobility (Bottom) of $Hg_{1-x}Cd_xSe$ samples grown with 6N Se vs. bandgap, as-grown and after various Se-annealed, and the predicted 77K $Hg_{1-x}Cd_xTe$ mobility for both low doping ($n\sim10^{14}$ cm^{-3}) and $n = 3x10^{16}$ cm^{-3} and $N_i = 7x10^{16}$ cm^{-3}.
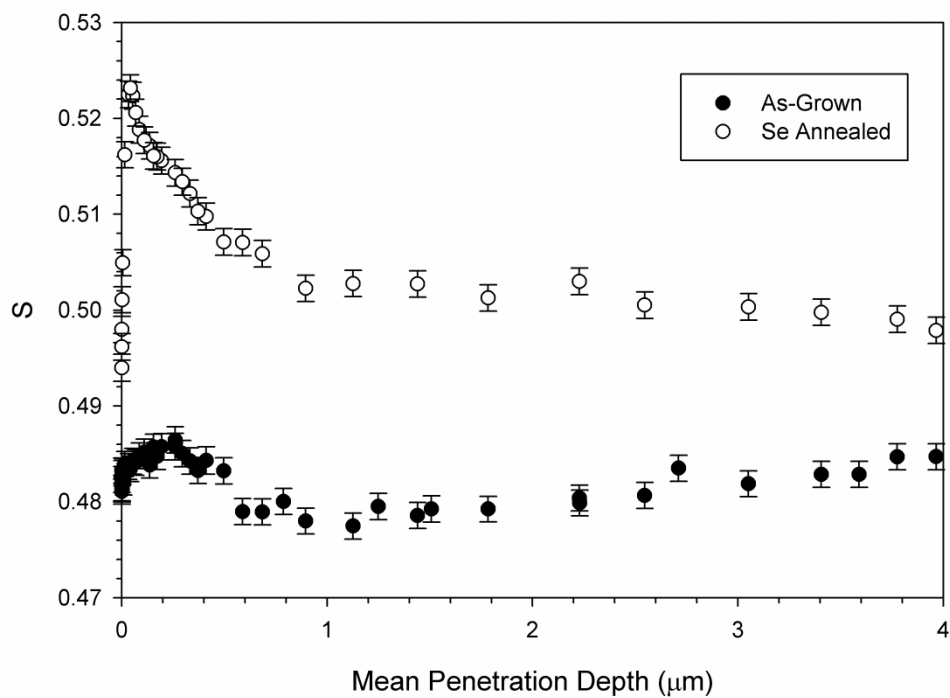
Figure 5-27: PAS measurement of an HgSe sample SZ80 (x = 0) before and after annealing under Se for 24 hours at 250 °C.
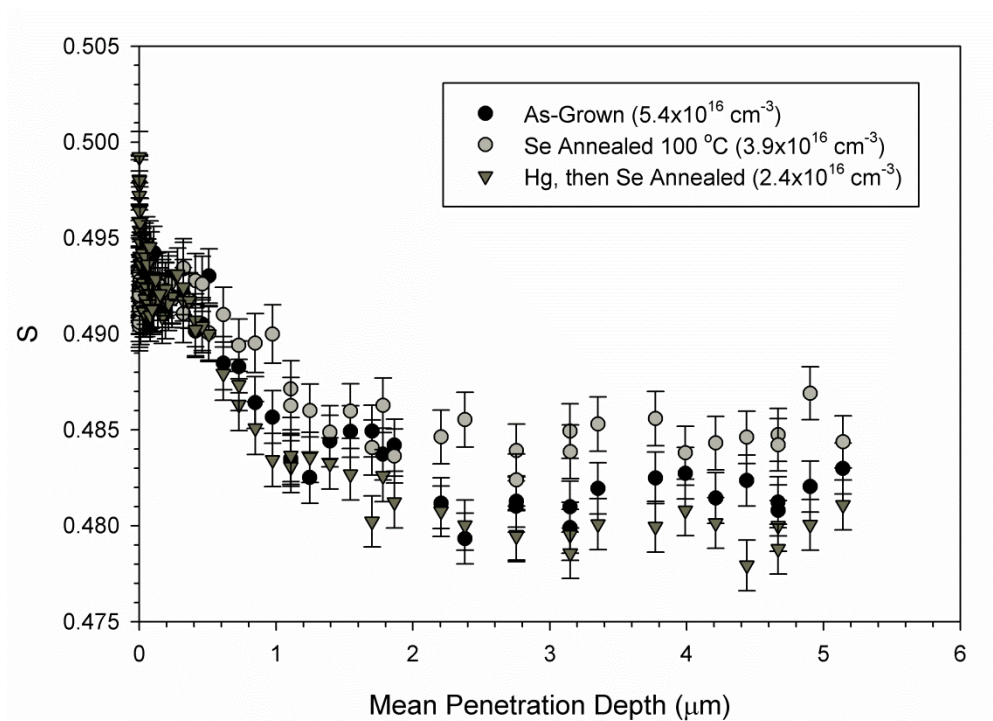
Figure 5-28: PAS measurement of SZ106 (x=0.28) as-grown, after Se-annealing at 100 °C for 24 hours, and after annealing under Hg, then Se at 250 °C for 24 hours, with the corresponding 77K electron concentration.

Variable temperature Hall measurements of sample SZ106 given in Figure 5-29 saw a greater reduction in n near room temperature than lower temperatures after annealing under Hg and then Se. Since the intrinsic electron concentration (n_{int}) is expected to be similar to that of $Hg_{1-x}Cd_xTe$, the room temperature n of SZ106 is greater than expected for n_{int} roughly by a factor of 16 and thus related to extrinsic doping. This suggests that there are two sources of background electrons, one with an energy level located in the conduction band (and thus still ionized at 4K) and one with an energy level in the bandgap that exhibits *freeze-out* between 100 and 300K. The fact that switching to 6N Se predominantly reduced the 12K concentration suggests that the energy levels in the conduction band are caused by impurities, similar to In dopants in $Hg_{1-x}Cd_xTe$ [3].

Likewise, the fact that a greater reduction in n after Se annealing is observed at higher temperatures suggests that the energy levels in the bandgap are due to V_{Se}. If so, variable temperature Hall measurements of SZ106 both as-grown and after annealing under Hg and then Se suggest a V_{Se} concentration $\sim 8 \times 10^{15}$ cm^{-3} at 300K and a background donor level of $\sim 2 \times 10^{16}$ cm^{-3}. By subtracting the background donor concentration from the total concentration and applying a fit to the freeze-out region as described in Section 3.10.3, the V_{Se} ionization energy (E_d) was calculated to be ~ 40 meV.

In addition to reducing n overall, annealing under Hg then Se appears to reduce the gradients in mobility and concentration described in Section 5.3.2. While annealing under Hg appeared to increase the conductivity overall, annealing under Se, and Hg then Se, produced a sharper dominant electron peak in conductivity as well as smaller secondary peaks according to QMSA as shown in Figure 5-30. This would suggest a more discrete mobility (and thus a reduced mobility gradient) after annealing under Se, and even more so after annealing under Hg then Se. One possible source of the mobility gradient is an inhomogeneous distribution of V_{Se} in

122
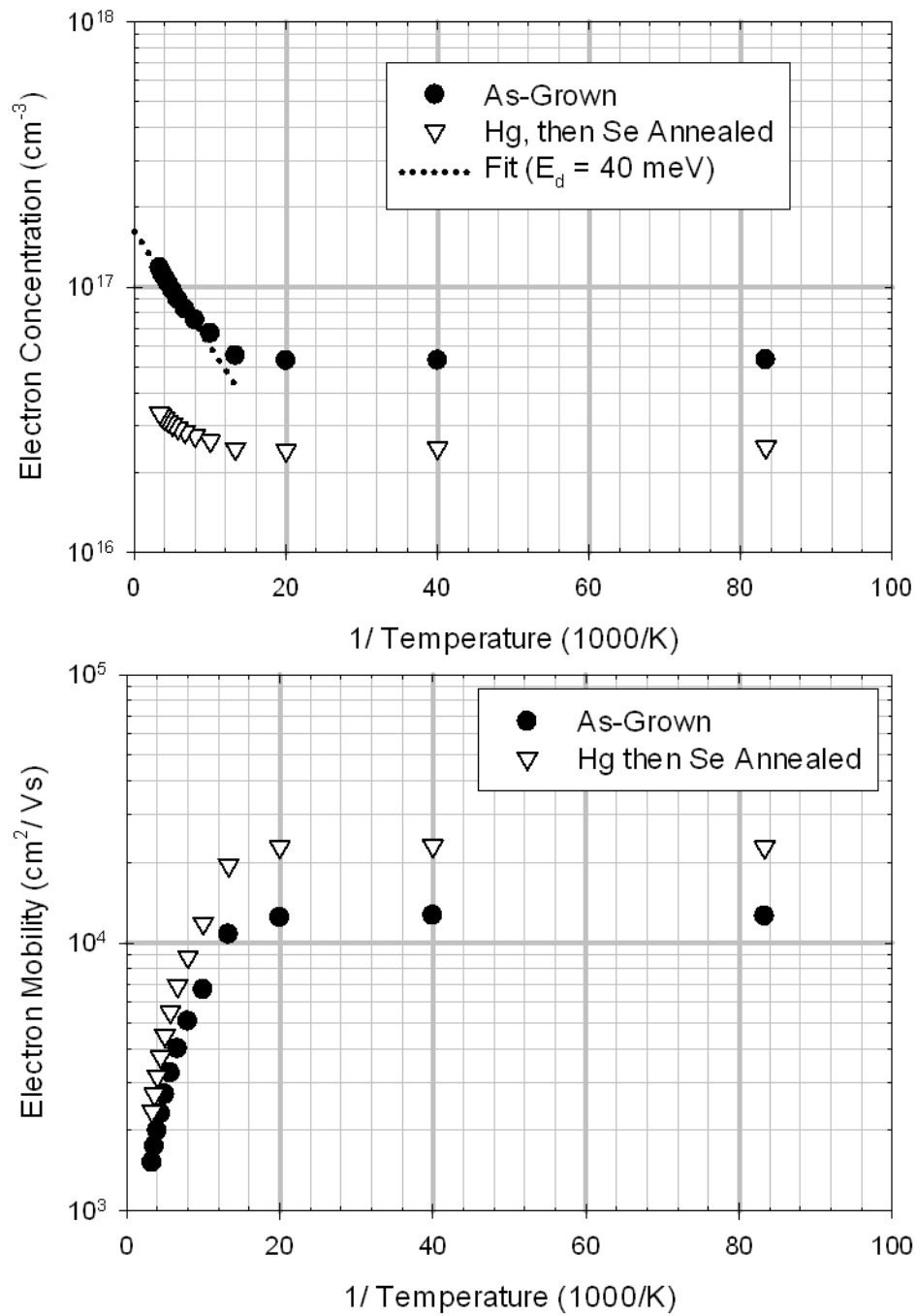
Figure 5-29: Electron concentration (Top) and mobility (Bottom) vs. temperature SZ106 (*x*=0.28) both as-grown, and after annealing under Hg, then Se for 24 hours each at 250 °C, as well as a fit to concentration at higher temperatures.
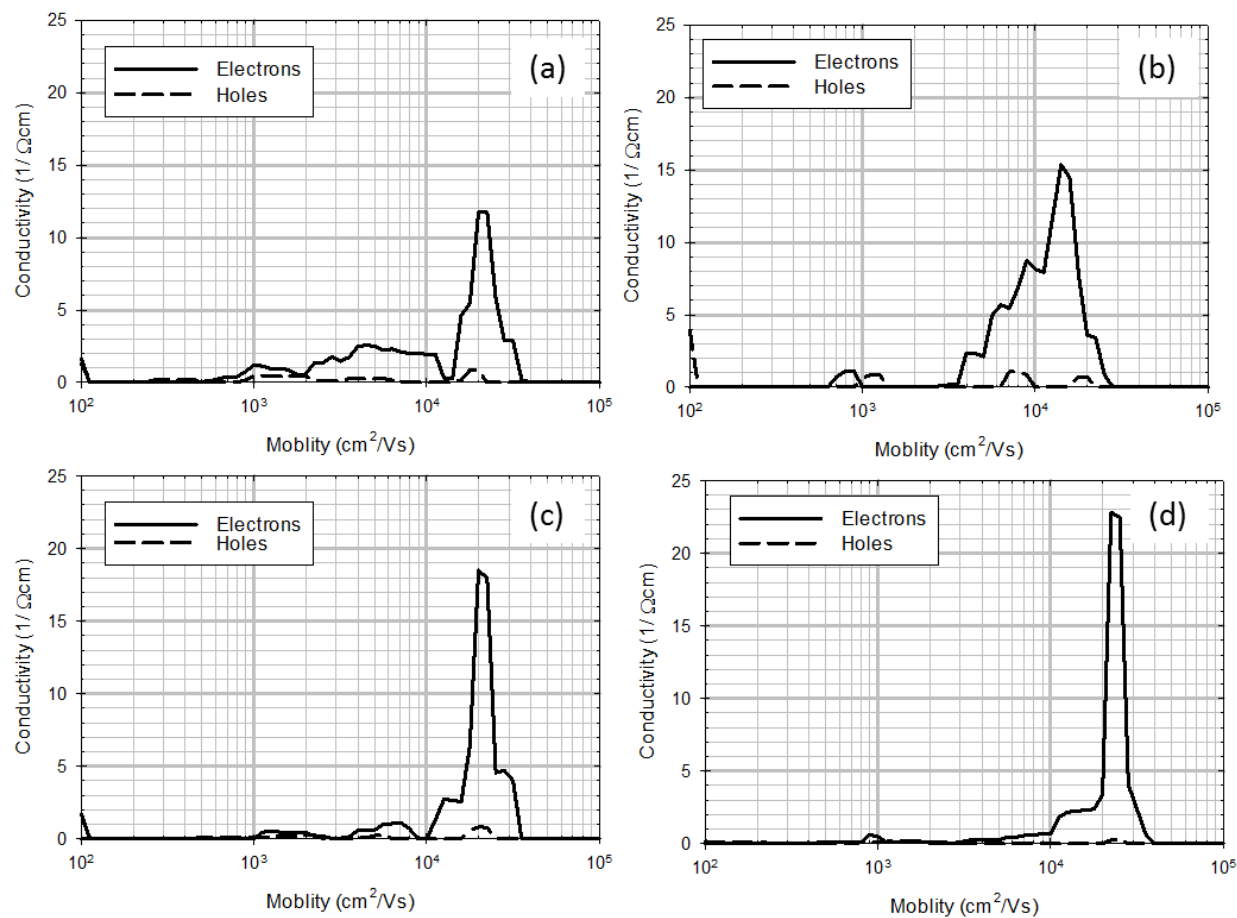
Figure 5-30: Conductivity vs. Mobility determined by QMSA for SZ106 ($x = 0.28$) at 77 K (a) as-grown, (b) Hg-annealed, (c) Se-annealed, and (d) Hg, then Se annealed. Anneals were for 24 hours at 250 °C.

124
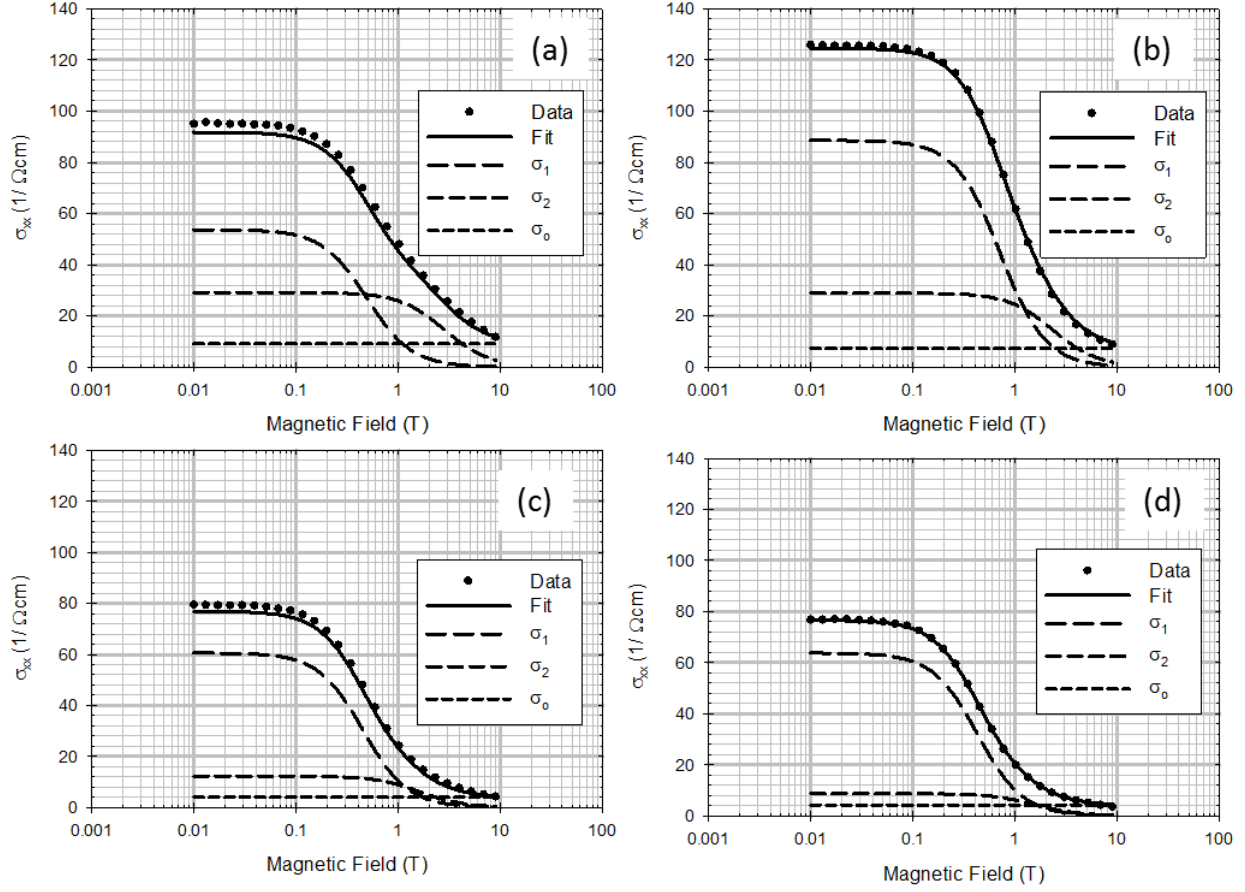
Figure 5-31: MCF to σ_{xx} vs. magnetic field using equation (5-1) for SZ106 ($x = 0.28$) at 77K (a) as-grown, (b) Hg-annealed, (c) Se-annealed, and (d) Hg, then Se annealed. Anneals were for 24 hours at 250 °C.
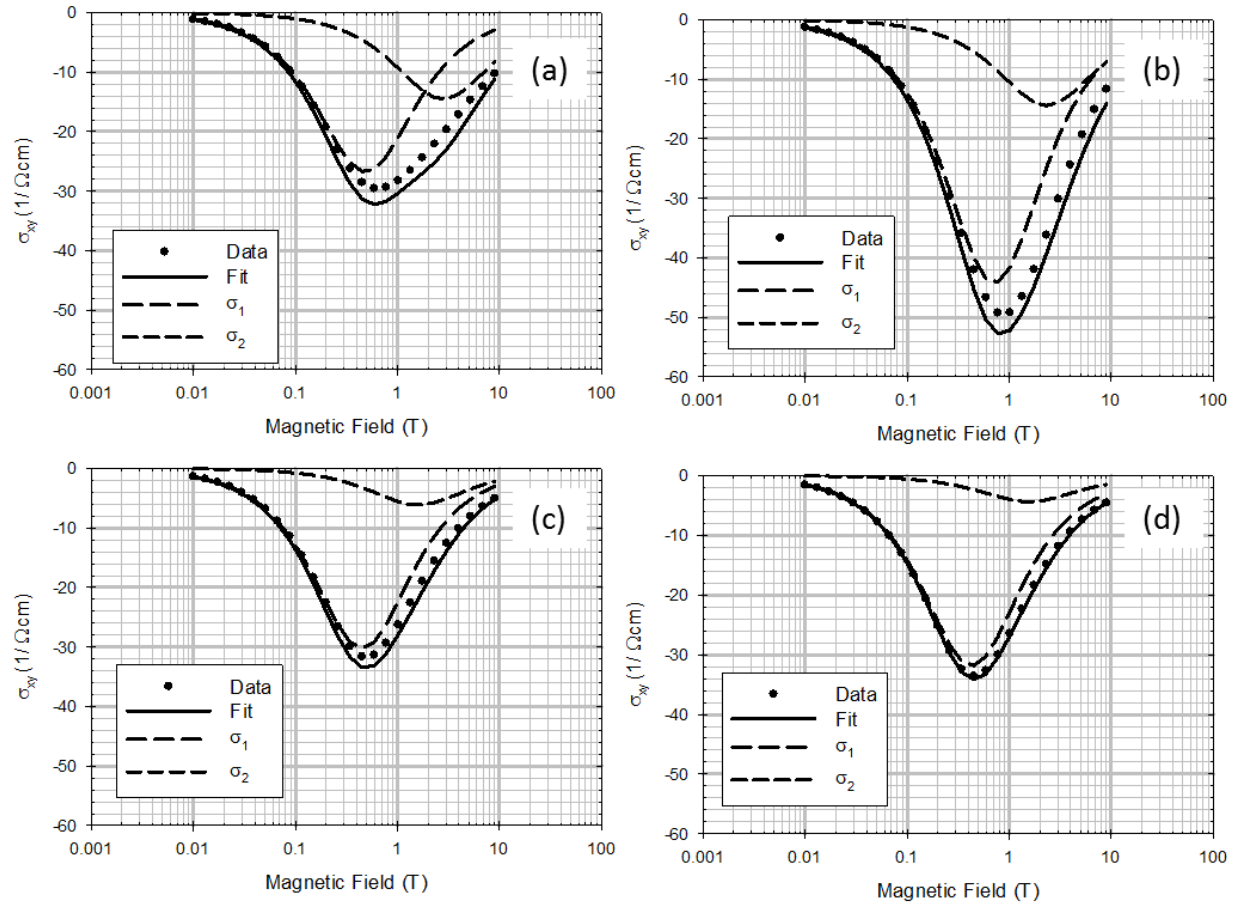
Figure 5-32: MCF to σ_{xy} vs. magnetic field using equation (5-2) for SZ106 (x = 0.28) at 77K (a) as-grown, (b) Hg-annealed, (c) Se-annealed, and (d) Hg, then Se annealed. Anneals were for 24 hours at 250 °C.

Parameter	As-Grown	Hg-Annealed	Se-Annealed	Hg, then Se Annealed	Unit
n_1	1.48	3.95	1.70	1.71	$\times 10^{16}\,cm^{-3}$
μ_1	21,304	13,973	22,205	23,298	cm^2/Vs
n_2	4.40	4.21	1.23	0.85	$\times 10^{16}\,cm^{-3}$
μ_2	4,285	4,279	6,233	6,429	cm^2/Vs
σ_o	13.66	7.17	5.87	4.20	$(\Omega cm)^{-1}$

Table 5-4: Hall parameters obtained through MCF to σ_{xx} and σ_{xy} vs. magnetic field using equations (5-1) and (5-2) respectively for SZ106 at 77K.

the sample, and annealing under Se reduces the V_{Se} distribution and therefore makes the mobility more discrete.

Figure 5-31 and Figure 5-32 show MCF of SZ106 to σ_{xx} vs. magnetic field using equation (5-1) and σ_{xy} vs. magnetic field using equation (5-2) respectively. The best MCF fits were obtained for the sample annealed under Hg then Se, which is consistent with a reduced mobility gradient since MCF assumes charge carriers have discrete mobilities. Table 5-4 gives the parameters obtained by MCF of SZ106. While the concentration of the dominant electron (n_1) increased slightly after Hg then Se annealing (1.5×10^{16} cm^{-3} to 1.7×10^{16} cm^{-3}), the secondary electron concentration (n_2) saw a significant decrease (4.4×10^{16} cm^{-3} to 8.5×10^{15} cm^{-3}) as did the conductivity due to low mobility carriers σ_o (13.7 to 4.2 (Ωcm)$^{-1}$). This would suggest that n_2, μ_2, and σ_o correspond to the mobility gradient, and optimizing the annealing procedure could reduce the mobility gradient to the point where MCF can be performed on Hg$_{1-x}$Cd$_x$Se assuming only a single carrier.

The lowest value for n was obtained after annealing sample SZ115 ($x = 0.15$) for 24 hours at 250 °C under Se. The annealed sample of SZ115 had $n = 9.4 \times 10^{15}$ cm^{-3} at 12K, as shown in Figure 5-33. Fitting to the concentration of as-grown SZ115 at higher temperatures yielded a value of $E_d = 43$ meV, which is consistent with the value obtained for SZ106. PAS of SZ115 given in Figure 5-34 indicates a slight increase in V_{Hg} after annealing, but the electron mobility did not decrease significantly suggesting minimal p-type compensation. This suggests it may be possible to influence the doping density with vacancies without significantly limiting mobility. If V_{Se} defects do freeze-out, then at lower temperatures V_{se} defects should be neutralized, and therefore detectable by PAS. Thus PAS measurements performed at lower temperatures could determine whether or not this defect is due to V_{Se}. Additionally, a series of
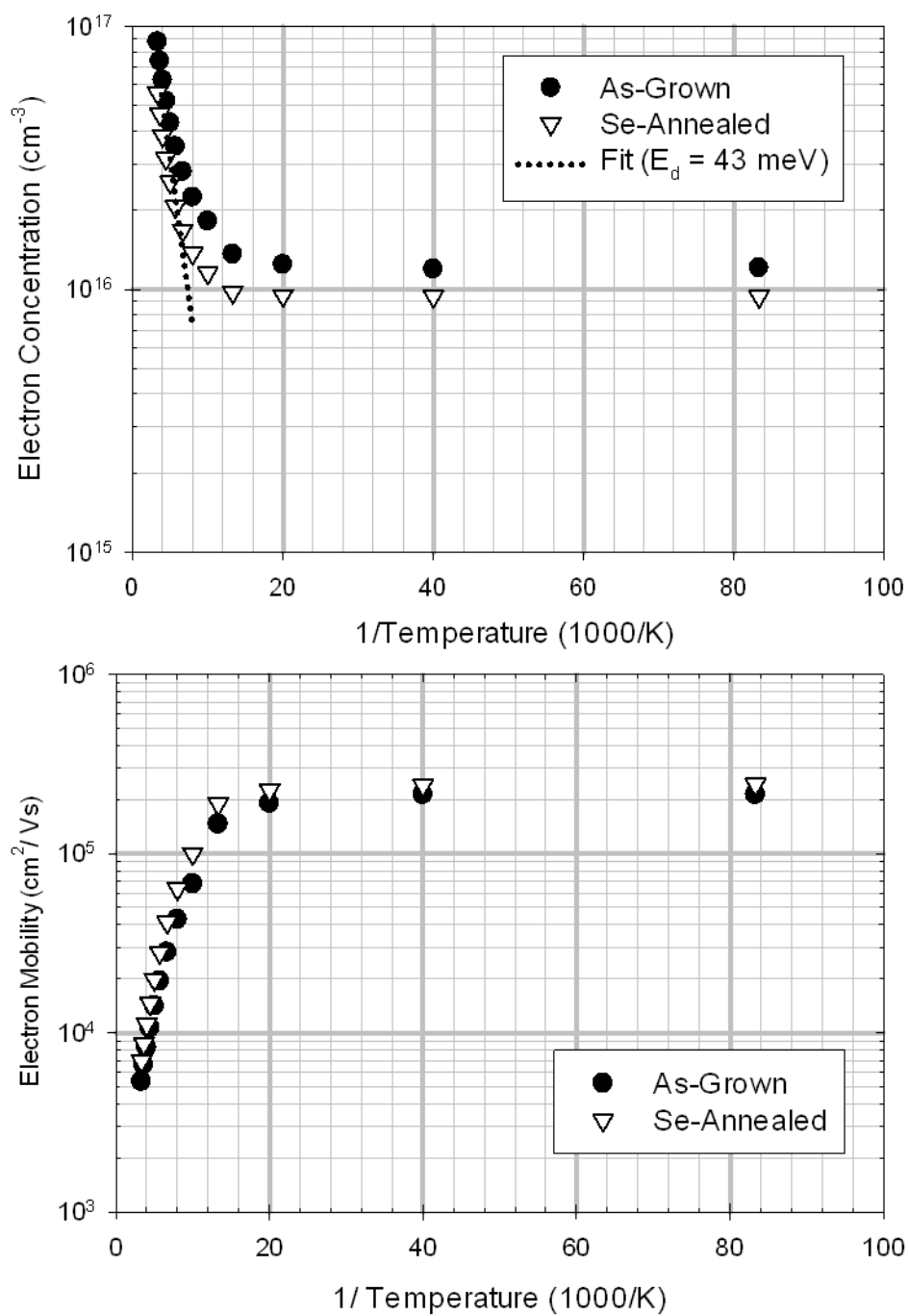
Figure 5-33: Electron concentration (Top) and mobility (Bottom) vs. temperature for SZ115 (*x*=0.15) both as-grown, and after annealing under Hg, then Se for 24 hours each at 250 °C.
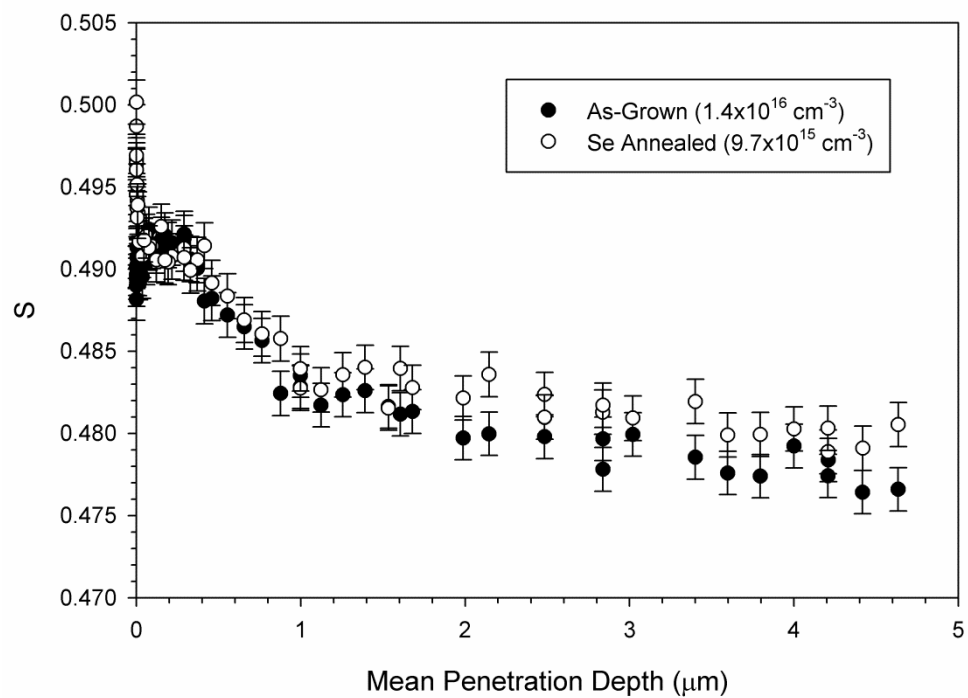
**Figure 5-34: PAS measurement of SZ115 as-grown, and after Se-annealing at 250 °C for 24 hours, with the 77K electron concentration given in parenthesis.**

anneals involving Hg and Se will need to be performed and further PAS measurements are required in order to determine if these samples are representative.

5.4 **Summary**

The growth of $Hg_{1-x}Cd_xSe$ on ZnTe/Si substrates was using a Se effusion cell (~Se_6) and a Se cracker (~Se_2). Like $Hg_{1-x}Cd_xTe$, $Hg_{1-x}Cd_xSe$ growth requires a large Hg overpressure and low substrate temperatures due the low sticking coefficient of Hg. The $Hg_{1-x}Cd_xSe$ growth rate was found to decrease when the substrate temperature was raised above ~130 °C when growing for a predominantly Se_6 flux and ~150 °C for a predominantly Se_2 flux. $Hg_{1-x}Cd_xSe$ must be grown at even lower temperatures than $Hg_{1-x}Cd_xTe$ (~185 °C), most likely due to the higher vapor pressure of Se than for Te. For a given substrate temperature and Hg overpressure, the growth rate varied linearly with Se BEP and the composition varied linearly with the Cd/Se BEP ratio. A higher *x*-value was obtained for the same Cd/Se BEP ratio when a predominantly Se_2 flux was used, suggesting greater incorporation of Cd with ~Se_2.

Nearly all samples appeared to exhibit streaky RHEED patterns during growth. After growth, sample surfaces were characterized using Nomarski microscopy, AFM, and SEM. The surface morphology of $Hg_{1-x}Cd_xSe$ samples depended on the substrate temperature and Hg BEP. The most prominent surface features of $Hg_{1-x}Cd_xSe$ growths were needle defects (also seen on $Hg_{1-x}Cd_xTe$) and "diamond" shaped defects which could be related to hillocks. The diamond and needle defects typically appear at higher growth temperatures which would suggest that they are related to Hg-deficient conditions. $Hg_{1-x}Cd_xSe$ grown at lower temperature saw the formation of Hg droplets on the surface. None of the $Hg_{1-x}Cd_xSe$ samples had the void defects typically seen in Hg-deficient $Hg_{1-x}Cd_xTe$ growths.

For a given Hg BEP of 2.5×10^{-4} Torr the optimal substrate temperature appears to be ~100 °C for samples grown with a ~Se_6 flux. These conditions provided the smoothest surfaces, and a few of these samples displayed crosshatch patterns which typically indicates a high quality growth. A smooth surface was not achieved for samples grown with a ~Se_2 flux, suggesting that the window of optimal growth parameters is narrower for growth with cracked Se. Only a small number of samples were grown with ~Se_6 using the cracker. More of these growths will need to be performed under the optimal conditions found for the effusion cell to confirm that these conditions are optimal for ~Se_6 fluxes. The rocking curve measured by XRD ranged from 200-300 arcseconds for the HgCdSe samples, with no clear relationship observed with growth parameters.

$Hg_{1-x}Cd_xSe$ samples grown with the effusion cell loaded with 5N Se had n ranging from 10^{17}-10^{18} cm^{-3} even at temperatures as low as 12K despite being nominally undoped, which is consistent with results reported by previous groups. However, samples grown with the cracker loaded with 6N Se had as-grown electron concentrations of 3-5×10^{16} cm^{-3} at 12K and mobilities similar to $Hg_{1-x}Cd_xTe$ with $n = 7 \times 10^{16}$ cm^{-3} and $N_i = 1.7 \times 10^{17}$ cm^{-3} at 77K . VFH measurements suggest a gradient in electron mobility, possibly due to an inhomogeneous distribution of V_{Se} introduced during growth.

The concentration remained low even when the cracking zone temperature was reduced to 325 °C to produce a ~Se_6 flux (like the effusion cell), suggesting that this lower n is due to the higher purity source material (5N vs. 6N) rather than the atomic species of Se flux (~Se_6 vs. ~Se_2). Exactly what impurities are coming from the Se source have yet to be identified. SIMS detected Br and Cl accumulating at the ZnTe interface, which could be introduced during the substrate preparation process. C,O, and Si were detected at the interface and near the surface of

the $Hg_{1-x}Cd_xSe$ layer—how they are introduced or if they are electrically active still needs to be determined.

PAS measurements strongly suggest the presence of p-type V_{Hg} in as-grown $Hg_{1-x}Cd_xSe$, much like $Hg_{1-x}Cd_xTe$. N-type Hg_i and V_{Se} are other possible defects, but no effective method of detecting them directly has yet been found. Annealing samples under Hg and Cd overpressures resulted in higher n, and Cd-anneals were also found to increase the x-value of samples near the surface, but not in the bulk. The lowest n's were obtained by annealing under Se. Se-annealing appears to increase V_{Hg}, but a sample annealed under Hg and then Se had fewer V_{Hg} and lower n, suggesting that V_{Se} were removed with the Se-annealing.

VFH suggests that annealing under Hg, then Se also reduced the mobility gradient, which is consistent with the anneal reducing an inhomogeneous distribution of V_{Se}. Temperature dependent Hall measurements of sample SZ106 indicate a greater reduction of n at higher temperatures, suggesting the presence of two donors: one with an energy level located in the conduction band (likely due to impurities) and one with an energy level the bandgap which freezes out at lower temperatures. Based on this sample the impurities appear to produce $n\sim2x10^{16}$ cm^{-3} while the energy level in the bandgap has an ionization energy of $E_d\sim40$ meV which produces $n\sim8x10^{15}$ cm^{-3} at 300K. The fact that Se-annealing appears to reduce the latter n suggests the energy level in the bandgap could be due to V_{Se}. Further PAS measurements are needed determine if SZ106 is representative.

6 Conclusions and Future Work

Hg$_{1-x}$Cd$_x$Se shows promise as a material for infrared detector technology. GaSb provides a nearly lattice-matched substrate for Hg$_{1-x}$Cd$_x$Se growth that is scalable to large areas and has dislocation densities of ~10^4 cm^{-2}. ZnTe$_{1-x}$Se$_x$ MBE layers were developed to serve as a non-conducting, II-VI buffer layer between II-VI Hg$_{1-x}$Cd$_x$Se and III-V GaSb to prevent mixed-phase at the interface and Ga inter-diffusion after annealing. Lattice-matched ZnTe$_{0.99}$Se$_{0.01}$/GaSb layers were produced with dislocation densities ~7×10^4 cm^{-2}, comparable to the GaSb substrate and thus providing a low dislocation density II-VI surface for Hg$_{1-x}$Cd$_x$Se deposition.

The growth of Hg$_{1-x}$Cd$_x$Se via MBE was examined using ZnTe/Si substrates. Hg$_{1-x}$Cd$_x$Se growths must be performed under large Hg overpressures and at even lower substrate temperatures than Hg$_{1-x}$Cd$_x$Te. Selenium vapor contains a mix of atomic species from Se$_2$ to Se$_8$, so growths were performed using both an Se effusion cell that produced a~Se$_6$, and an Se cracker that could produce either an ~Se$_2$ or ~Se$_6$ flux. The surface morphology of Hg$_{1-x}$Cd$_x$Se was found to depend on the substrate temperature and Hg overpressure. Hg-deficient conditions produced needle defects and diamond-shaped defects that could be related to hillocks on the sample surface, but not void defects as observed on Hg$_{1-x}$Cd$_x$Te surfaces. Samples grown with the effusion cell suggest that for an Hg BEP of 2.4×10^{-4} Torr, the ideal substrate temperature is ~100 °C for a ~Se$_6$ flux. The optimal parameters for growths with an ~Se$_2$ flux using the cracker were not found, and growths with an ~Se$_6$ flux using the cracker need to be performed using the same optimal parameters found for the effusion cell. For a given substrate temperature and Hg BEP, the growth rate can be controlled by the Se BEP and the composition by the Cd/Se BEP ratio.

The large background electron concentrations reported earlier for Hg$_{1-x}$Cd$_x$Se (10^{17}-10^{18} cm^{-3}) were reduced by an order of magnitude by using Se source material with 6N purity raher

than 5N. SIMS ultimately could not identify the specific contaminants responsible for the background electrons, but it did detect Br and Cl at the $Hg_{1-x}Cd_xSe/ZnTe$ interface that could be introduced during the substrate preparation process. SIMS also indicated the presence of C, O, and Si at the interface and near the sample surface—how these elements were introduced and whether they are electrically active need to be determined.

PAS measurements strongly suggest the presence of p-type V_{Hg}, and n-type Hg_i and V_{Se} have also been proposed as potential native defects. An $Hg_{1-x}Cd_xSe$ sample annealed under Hg then Se had lower V_{Hg} and lower n, suggesting that this process reduces V_{Hg} and V_{Se}. This anneal also appears to reduce a mobility gradient that could be produced by an inhomogeneous distribution of V_{Se}. Temperature dependent Hall measurements indicate two species of donors, one that freezes out at lower temperatures (bandgap energy level) and one that does not (conduction band energy level). The former was reduced by Se-annealing, suggesting it is V_{Se}.

Many challenges remain before $Hg_{1-x}Cd_xSe$ FPAs can be produced. As stated in Section 4.6, the slight lattice-mismatch between $Hg_{1-x}Cd_xSe$ and GaSb could be alleviated by a graded $ZnTe_{1-x}Se_x$ buffer layer with an x-value that gradually shifts from 0.01 to 0.04. These will need to be explored, as will the MBE growth of $Hg_{1-x}Cd_xSe$ on $ZnTe_{1-x}Se_x$/GaSb. Another option to consider is adding Te to form the quaternary alloy $Hg_{1-x}Cd_xSe_{1-y}Te_y$ to lattice-match the material to $ZnTe_{0.99}Se_{0.01}$/GaSb. Of primary importance is further reducing the background electron concentration of $Hg_{1-x}Cd_xSe$, preferably to at least $\sim10^{14}$ cm^{-3}. The greatest reduction in n was achieved by switching from 5N Se source material to 6N, and so n could be further reduced by using Se source material with 7N purity. XPS measurements on the ZnTe/Si substrates should be employed to determine if Cl and Br is being added during the substrate preparation process, and the source of the C, O, and Si on the surface and interface need to be determined (as well as their effect on the electrical properties).

Only a handful of samples could be measured by PAS, so more measurements are needed to confirm that the observed trends in $Hg_{1-x}Cd_xSe$ are representative. Currently the PAS measurements are performed at room temperature. However, if the selenium vacancies do freeze out, then at lower temperatures they would eventually be neutralized and therefore detectable by PAS. Thus a system will need to be developed to measure PAS at lower temperatures. A combination of Hg and Se annealing appears to produce the best Hall results, but the annealing parameters have yet to be fully explored. A series of Hg and Se anneals will need to be performed at various temperatures and durations, and then evaluated using PAS and Hall measurements to determine the most effective process for removing native defects.

Once the background electron concentration has been lowered, an effective method for p-type doping $Hg_{1-x}Cd_xSe$ will need to be determined. Given that $Hg_{1-x}Cd_xSe$ appears to contain vacancies of Group VI Se, the best method would probably be filling these vacancies with a Group V element such as arsenic. After p-type doping of $Hg_{1-x}Cd_xSe$ has been established, a procedure for producing $Hg_{1-x}Cd_xSe$ p-n junctions will need to be explored. This process will then need to be scaled up so that large area $Hg_{1-x}Cd_xSe$ diode layers can then be fashioned into 3rd generation LWIR FPAs.

Directly comparing the dislocation densities of $Hg_{1-x}Cd_xTe$ and $Hg_{1-x}Cd_xSe$ will require EPD measurements of $Hg_{1-x}Cd_xSe$, and thus a defect etchant for $Hg_{1-x}Cd_xSe$ needs to be determined. Preliminary work on defect etching of $Hg_{1-x}Cd_xSe$ is given in the following Appendix 2.

7 Appendix 1: Sample List

7.1 TxState Sample List

Name	Substrate	Purpose	L1 Tsub (°C)	L1 growth time
Z1	GaSb(211)	First growth of ZnTe	345	30 mins
Z2	GaSb(211)	Second growth of ZnTe	345	2h
Z4	GaSb(211)	hydrogen Cleaning		
Z5	GaSb(211)	hydrogen Cleaning		
Z6	GaSb(211)	hydrogen Cleaning		
Z7	GaSb(211)	hydrogen Cleaning		
Z8	GaSb(211)	hydrogen Cleaning		
Z9	GaSb(211)	hydrogen Cleaning		
Z10	GaSb(211)	hydrogen Cleaning		
Z11	GaSb(211)	hydrogen Cleaning		
Z12	GaSb(211)	Thermal desporption under vacuum		
Z13	GaSb(211)	hydrogen Cleaning		
Z14	GaSb(211)	Growth of ZnTe	332	2:05:30
Z15	GaSb(211)	Growth of ZnTe	285	2:00:00
Z16	GaSb(211)	Growth of ZnTe	332	3:00:00
Z17	GaAs(100)	Growth of ZnTe	285	6h
Z18	GaSb(100)	Growth of ZnTe	285	34 mins
Z19	GaAs (100)	Growth rate study: Fixed Te, Vary Zn	285	3:39:50
Z20	GaAs (100)	Growth rate study: Fixed Te, Vary Zn	285	1:25:00
Z21	GaAs (100)	Growth rate study: After unclog Zn	285	3:53:20
Z22	GaAs (100)	Growth rate study: Fixed Te, Vary Zn, Vary Tsub	variable	3:45:00
Z23	GaAs (100)	Growth rate study	285	2:41:27
Z24	GaAs (100)	near stochiometric growth at Tsub = 345°C	345	3hr
Z25	GaAs (100)	Growth rate study: Fixed Zn, Vary Te	375	5:36
Z26	GaAs (100)	slightly Zn-rich growth at Tsub = 375°C	375	4hr
Z27	GaAs (100)	thermally desorb GaAs at 580°C	580	
Z28	GaAs (100)	AH clean at 420°C for 20 min at 2e-6 torr		
Z29	GaAs (100)	Re-do of Z26	375	2hr
Z30	GaAs (100)	Similar to Z29 but at Tsub = 345°C	345	2hr
Z31	GaAs (100)	Growth rate study at Tsub = 345°C	345	6:02:53
Z32	GaAs (100)	Zn-rich ZnTe, change Te from 30s to 10s	345	3hr
Z33	GaAs (100)	Thermal desorption of GaAs(100)	640	
Z34	GaAs (211)	Repeat Z32 but on GaAs(211)	345	3hr
Z35	GaAs (211)	Repeat Z34 and hope for stable Zn	345	3hr
Z36	GaAs (211)	Repeat of Z34 but for twice as long	345	6hr

Z37	GaSb(111)	AHC at 400°C for 20 min at 2e-6 torr		
Z38	GaSb(111)	AHC at 350°C for 20 min at 2e-6 torr		
Z39	GaSb(111)	AHC at 300°C for 20 min at 2e-6 torr		
Z40	GaSb(111)	AHC at 250°C for 20 min at 2e-6 torr		
Z41	GaSb(111)	AHC: 400°C, 20 min, 2e-6, 50° tilt XPS		
Z42	GaSb(111)	AHC: 300°C, 20 min, 2e-6, 50° tilt XPS		
Z43	GaAs(100)	Growth rate study after removing Zn insert	345	
Z44	GaSb(111)	AHC: 350°C, 20 min, 2e-6, 50° tilt XPS		
Z45	GaAs(100)	ZnTe calibration. Zn=4.4e-7, Tsub = 345	345	
Z46	GaAs(100)	ZnTe calibration. Zn=2.3e-7, Tsub = 345	345	
Z47	GaSb(111)	AHC at 425°C for 20 min at 2e-6 torr		
Z48	GaSb(100)	Fine tune ZnTe growth rate	345	
7-166	GaSb(100)	2 um GaSb/GaSb(100)	650	2hr
Z49	GaSb(100)	2 um stoichiometric ZnTe/GaSb(100)	345	7hr
7-168	GaSb(211)	2 um GaSb/GaSb(211)	600	2hr
7-169	GaSb(100)	2 um GaSb/GaSb(100) for ZnTe growth	700	2hr
Z50	GaSb(100)	2 um Zn-rich ZnTe/GaSb(100)	345	7hr
7-171	GaSb(211)	2 um GaSb/GaSb(211) for ZnTe growth	600	2hr
Z51	GaSb(100)	2 um Te-rich ZnTe/GaSb(100)	345	7hr
C52	GaAs(100)	CdTe cell calibration	210	1hr
Z53	GaAs(100)	1/4 mount GaAs desorption for temperature calibration	720	
Z54	GaSb(100)	2 um ZnTe/GaSb/GaSb(100)	445	7hr
C55	GaAs(100)	CdTe cell calibration	200	1hr
C56	GaAs(100)	CdTe cell calibration confirm	210	1hr
7-177	GaSb(211)	2 um GaSb/GaSb(211)	600	2 hr 1 min
Z57	GaAs(100)	ZnSe calibration	345	
7-178	GaSb(211)	2 um GaSb/GaSb(211)	600	2 hr 1 min
7-179	GaSb(100)	2 um GaSb/GaSb(100) - drop somewhere…	610	2 hr 1 min
7-180	GaSb(100)	2 um GaSb/GaSb(100) - drop in Sb buffer	600	2 hr 1 min
C58	GaAs (100)	CdSe calibration	275	
C59	GaAs (100)	CdSe calibration	275	
C60	GaAs (100)	CdSe calibration	275	
C61	GaAs (100)	CdTe cell confirm	180	1hr
C62				
7-194	GaSb(100)	2 um GaSb to check Sb uniformity	670	2 hr 1 min
Z63	GaSb(211)	hydrogen cleaning and defect etch		
C64	GaSb (100)	Stoichiometric growth of CdSe	275	5h
Z65	GaSb (100)	Growth of ZnTeSe matched to HgCdSe	345	3h 30m
C66	GaSb (100)	CdTeSe matched to HgCdSe	275	5h
Z67	GaSb (100)	Growth of ZnTeSe matched to GaSb	345	3h 3m
Z68_1	GaSb (100)	AHC study of IE GaSb(100)		
Z68	GaSb (100)	ZnTeSe matched to GaSb		

Z69	GaSb (100)	ZnTeSe matched to GaSb at lower growth rate	345	7hr
Z70	GaSb (100)	ZnTeSe matched to GaSb at lower Ts	330	4 hr
Z71	GaSb (100)	AHC in II-VI chamber		
Z72	GaSb (100)	ZnTeSe/ZnTe/GaSb	345	30 min
Z73	GaSb (100)	Same as Z72 except Ts = 360°C	360	30 min
Z74	GaSb (211)	1st ZnTeSe on GaSb(211)	345	30 min
Z75	GaSb (211)	2nd ZnTeSe on GaSb(211)	360	30 min
Z76	GaSb (211)	higher Ts ZnTeSe	375	30 min
Z77	GaSb (211)	higher Zn flux at Ts = 360	360	30 min
7-207	GaSb (211)	Regrowth with fixed Sb source		
Z78	GaSb (211)	stoichiometric ZnTeSe at 360°C	360	30 min
Z79	GaAs(100)	ZnTe growth rate study to increase Z78 GR	360	variable
Z80	GaSb (211)	2.1 um ZnTe/GaSb(211)	345	2 hr 51 min
Z81	GaSb (211)	50 nm ZnTe for tc study	360	9 min 54 s
Z82	GaSb (211)	100 nm ZnTe for tc study	360	19 min 48s
Z83	GaSb (211)	150 nm ZnTe for tc study	360	29 min 42s
Z84	GaSb (211)	200 nm ZnTe for tc study	360	39 min 36s
Z85	GaSb (211)	250 nm ZnTe for tc study	360	49 min 30s
Z86	GaSb (211)	AHC only		
Z87	GaSb(211)	300 nm ZnTe for tc study	360	59 min 24s
Z88	GaSb(211)	repeat 300 nm ZnTe for tc study	360	59 min 24s
7-247	GaSb(211)	1st GaSb on new IE GaSb(211)	650	2 hr
Z89	GaSb(211)	1 um ZnTe for tc study	360	3 hr 18 mins
Z90	GaSb(211)	500 nm ZnTe for tc study	360	1 hr 39 mins
Z91	GaAs(100)	500 nm ZnTe on another sub	360	1 hr 39 mins
Z92	GaSb(211)	400 nm ZnTe for tc study	360	1 hr 19 mins
Z93	GaSb(211)	350 nm ZnTe for tc study	360	1 hr 9 mins
Z94	GaSb(211)	375 nm ZnTe for tc study	360	1 hr 14 mins 17s
Z95	GaAs(211)	500 nm ZnTe on another sub	360	1 hr 39 mins

7.2 ARL Sample List

Name	Substrate	Structure	x-value	Thickness (μm)	Growth rate (μm/hr)
Began Growth with Se effusion cell loaded with 5N Se					
SZ0002	ZnTe/Si	HgCdSe	0.305	4.50	1.5
SZ0003	ZnTe/Si	HgCdSe	0.184	5.90	1.5
SZ0004	ZnTe/Si	HgCdSe	0.148	7.80	2.0

SZ0005	ZnTe/Si	HgCdSe	0.188	8.60	2.2
SZ0006	ZnTe/Si	HgCdSe	0.216	7.50	2.0
SZ0007	ZnTe/Si	HgCdSe	0.158	4.70	2.2
SZ0008	ZnTe/Si	HgCdSe	0.216	3.50	1.8
SZ0009	ZnTe/Si	HgCdSe	0.189	3.40	1.7
SZ0010	ZnTe/Si	HgCdSe	0.214	3.50	1.7
SZ0011	ZnTe/Si	HgCdSe	0.189	3.40	1.7
SZ0012	ZnTe/Si	HgCdSe	0.187	3.90	2.0
SZ0013	ZnTe/Si	HgCdSe	0.186	3.40	1.7
SZ0014	ZnTe/Si	HgCdSe	0.203	3.40	1.7
SZ0015	ZnTe/Si	HgCdSe	0.213	3.00	1.5
Chamber vented for Maintenance					
SZ0040	ZnTe/Si	HgCdSe	0.288	3.80	1.5
SZ0041	ZnTe/Si	HgCdSe	0.203	4.80	1.6
SZ0042	ZnTe/Si	HgCdSe	0.251	7.60	2.5
SZ0043	ZnTe/Si	HgCdSe	0.183	7.30	2.4
SZ0044	ZnTe/Si	HgCdSe	0.183	6.80	2.3
SZ0045	ZnTe/Si	HgCdSe	0.169	7.70	2.6
SZ0046	ZnTe/Si	HgCdSe	0.183	5.40	1.8
SZ0047	ZnTe/Si	HgCdSe	0.174	6.40	2.1
SZ0048	ZnTe/Si	HgCdSe	0.160	6.80	2.3
SZ0049	ZnTe/Si	HgCdSe	0.176	5.50	1.8
SZ0050	ZnTe/Si	HgCdSe	0.194	7.60	1.9
SZ0051	ZnTe/Si	HgCdSe	0.186	5.00	1.7
SZ0052	ZnTe/Si	HgCdSe	0.197	9.90	2.5
SZ0053	ZnTe/Si	HgCdSe	0.203	8.30	2.8
SZ0054	ZnTe/Si	HgCdSe	no cut-off	3.40	0.9
SZ0055	ZnTe/Si	HgCdSe	0.334	3.40	0.9
SZ0056	ZnTe/Si	HgCdSe	0.211	8.90	3.0
SZ0057	ZnTe/Si	HgCdSe	0.251	7.00	1.8
SZ0058	ZnTe/Si	HgCdSe	0.203	7.40	2.5
SZ0059	ZnTe/Si	HgCdSe	0.180	7.80	2.6
SZ0060	ZnTe/Si	CdSe/HgCdSe	0.214	5.10	1.6
SZ0061	ZnTe/Si	CdSe/HgCdSe	0.233	5.60	1.8
SZ0062	ZnTe/Si	HgSe	0.076	5.90	2.0
SZ0063	ZnTe/Si	HgSe	0.092	6.70	2.2
Chamber vented for Maintenance					
SZ0064	ZnTe/Si	HgCdSe	0.424	3.50	1.2
SZ0065	ZnTe/Si	HgCdSe	0.194	Uncertain	
SZ0066	ZnTe/Si	HgCdSe	0.239	4.90	1.6

SZ0067	ZnTe/Si	HgCdSe	0.298	1.81	1.2
SZ0069	ZnTe/Si	HgCdSe	0.35	1.45	1.5
SZ0071	ZnTe/Si	HgCdSe	0.422	2.53	0.8
SZ0072	ZnTe/Si	HgCdSeTe	0.614	0.93	0.5
SZ0073	ZnTe/Si	HgCdSe	0.33	2.40	1.2
SZ0074	ZnTe/Si	HgCdSe	0.306	3.64	1.2
SZ0075	ZnTe/Si	HgCdSeTe	0.244	4.26	1.4
SZ0076	ZnTe/Si	HgCdSeTe	0.149	5.76	1.9
SZ0077	ZnTe/Si	HgCdSe	0.243	4.27	1.4
SZ0078	ZnTe/Si	HgCdSe	0.393	2.23	0.8
SZ0079	ZnTe/Si	HgCdSe	0.224	4.24	1.4
Chamber vented for Maintenance					
SZ0080	ZnTe/Si	HgSe	N/A	3.40	1.1
SZ0081	ZnTe/Si	HgSe	N/A	4.48	1.5
SZ0082	ZnTe/Si	HgSe	N/A	1.54	0.6
SZ0083	ZnTe/Si	HgSe	N/A	2.10	0.7
SZ0084	ZnTe/Si	HgSe	N/A	3.31	1.1
SZ0085	ZnTe/Si	HgSe	N/A	5.14	1.7
SZ0086	ZnTe/Si	HgSe	N/A	1.95	0.7
SZ0087	ZnTe/Si	CdSe/HgCdSe	0.31	4.78	1.1
SZ0088	ZnTe/Si	CdSe/HgCdSe	0.262	5.36	1.2
SZ0089	ZnTe/Si	HgCdSe	0.701	1.30	0.4
SZ0090	ZnTe/Si	HgCdSe	0.673	5.34	1.8
SZ0091	ZnTe/Si	HgCdSe	0.541	4.99	1.7
SZ0092	ZnTe/Si	HgCdSe	0.303	4.63	1.5
SZ0093	ZnTe/Si	HgCdSe	0.787	2.79	1.4
SZ0094	ZnTe/Si	HgCdSe	0.146	3.05	1.5
SZ0096	ZnTe/Si	HgCdSe	0.725	5.04	1.7
Chamber vented for Maintenance: Installed Se Cracker with 6N Se					
SZ0097	ZnTe/Si	HgCdSe	0.198	7.76	2.6
SZ0098	ZnTe/Si	HgCdSe	0.134	4.53	1.5
Sz0099	ZnTe/Si	HgCdSe	0.138	8.86	3.0
SZ0100	ZnTe/Si	HgCdSe	0.151	4.59	1.5
SZ0101	ZnTe/Si	HgCdSe	0.149	5.15	1.7
SZ0102	ZnTe/Si	HgCdSe	0.174	4.63	1.5
SZ0103	ZnTe/Si	HgCdSe	0.268	3.80	1.3
SZ0104	ZnTe/Si	HgCdSe	0.263	3.42	1.1
SZ0105	ZnTe/Si	HgCdSe	0.357	2.89	1.0
SZ0106	ZnTe/Si	HgCdSe	0.276	6.42	4.3
SZ0107	ZnTe/Si	HgCdSe	0.293	4.25	2.1

SZ0108	ZnTe/Si	HgCdSe	0.213	3.43	0.9
SC0108	CdTe/Si	HgCdSe	0.214	3.53	0.9
SZ0109	ZnTe/Si	HgCdSe	0.245	3.43	3.4
SZ0110	ZnTe/Si	HgCdSe	0.306	4.07	4.1
SZ0111	ZnTe/Si	HgCdSe	0.208	3.51	0.9
SC0111	CdTe/Si	HgCdSe	0.211	3.66	0.9
SZ0112	ZnTe/Si	HgCdSe	0.17	3.12	1.6
SZ0113	ZnTe/Si	HgCdSe	0.18	3.47	1.7
SZ0114	ZnTe/Si	HgCdSe	0.185	2.76	1.4
SZ0115	ZnTe/Si	HgCdSe	0.147	8.54	2.9
SZ0116	ZnTe/Si	HgCdSe	0.207	5.07	1.3
SZ0117	ZnTe/Si	HgCdSe	0.252	2.63	0.9
SZ0118	ZnTe/Si	HgCdSe	0.173	3.83	1.3
SZ0119	ZnTe/Si	HgCdSe	0.211	3.52	1.2
SZ0120	ZnTe/Si	HgCdSe	0.211	3.35	1.1
SZ0121	ZnTe/Si	HgCdSe	0.2	4.62	1.2
SZ0122	ZnTe/Si	HgCdSe	0.193	4.74	1.2
SZ0123	ZnTe/Si	HgSe	0	2.35	1.2
SZ0124	ZnTe/Si	Thin HgSe	0	~85nm	~1.2
SZ0125	ZnTe/Si	Thin HgSe	0	~75nm	~1.2
SZ0126	ZnTe/Si	HgCdSe	Thin	0.2	1.2
SZ0127	ZnTe/Si	HgCdSe	thin	0.73	0.7
sz0128	ZnTe/Si	HgCdSe	thin	0.73	0.7
SZ0129	ZnTe/Si	HgCdSe	0.115	7.42	1.9
SZ0130	ZnTe/Si	HgCdSe	0.175	4.2	1.1
SZ0131	ZnTe/Si	HgCdSe	0.201	3.47	0.9
SZ0132	ZnTe/Si	HgCdSe	0.298	2.47	0.6
SZ0133	ZnTe/Si	HgCdSe	0.109	6.71	1.7
SZ0134	ZnTe/Si	CdTe/HgCdSe	0.276	6.54	1.5
TC0135	CdTe/Si	HgCdTe	0.618	3.12	0.8
TC0136	CdTe/Si	HgCdTe	0.315	5.49	0.9

8 Appendix 2: Wet Etching of Mercury Cadmium Selenide

Fabricating often involves chemical etching of a semiconductor material. Wet chemical etching (etching in liquids as opposed to plasmas) typically has three applications for device fabrication—pattern fabrication, polishing, and the visualization of damage or defects [53]. No prior research on wet etching of $Hg_{1-x}Cd_xSe$ was found, and so a preliminary study of wet etching $Hg_{1-x}Cd_xSe$ for polishing and defect visualization was performed.

8.1 Polishing Etch

The surface roughness of a photodiode can affect the device performance. A rough surface creates recombination centers for minority carriers, leading to a shorter minority carrier lifetime. Surface roughness can also contribute to the dark current, creating noise [4]. Thus in order to achieve maximum device performance, a process must be developed to produce as smooth a surface as possible. Typically this will involve a chemical solution that etches the material at a uniform rate. Depending on the material, a smooth surface can be obtained by submerging the material in this solution (chemical etching), rubbing the material surface across an abrasive pad coated in this solution (chemomechanical polishing, or CMP), or submerging the material and applying a potential difference (electrochemical polishing).

In addition to reducing surface roughness, etching is also used to remove surface oxides and other surface contaminants. Semiconductor samples are typically etched to remove any oxide layers on the surface immediately prior to loading in high vacuum systems. Thus an etchant is required that will remove the material uniformly at a known rate [53].

8.1.1 Mercury Cadmium Telluride

The most commonly used etchant for $Hg_{1-x}Cd_xTe$ is a solution of bromine (Br) and

methanol (MeOH). Br reacts with Cd and Hg to form $CdBr_2$ and $HgBr_2$ respectively, leaving behind elemental Te. These products then dissolve in the solution. Not all reactions in this process occur at equal rates, and so the three elements are not removed uniformly from the sample. Cd has the fastest reaction rate in Br:MeOH while Te has the slowest. As a result, etching $Hg_{1-x}Cd_xTe$ in Br: MeOH typically produces a Te-rich surface. This remaining Te produces a relatively rough surface, and thus a smooth $Hg_{1-x}Cd_xTe$ surface usually requires chemo-mechanical polishing with Br: MeOH rather than just a chemical etch [54]. The rate at which the material is removed (etch rate) is determined by the concentration of bromine, with higher concentrations leading to a faster etch rate and vice versa. A typical bromine concentration is 0.2% by volume, which removes ~30 nm/s [55].

8.1.2   Mercury Cadmium Selenide

$Hg_{1-x}Cd_xSe$ samples grown on ZnTe/Si substrates were etched in Br:MeOH solutions, followed by methanol rinses in two separate beakers. The etch depths was determined by scratching pieces of the sample at opposite corners down to the silicon substrate, and measuring the change in height between the Si substrate and the surface of the layer with the Tencor step-profiler before and after etching. This difference in height was divided by the etching time to determine the etch rate of the solution. Initially the standard $Hg_{1-x}Cd_xTe$ etch solution with a 0.2% Br-concentration was used, which has an etch rate of ~30 nm/s for $Hg_{1-x}Cd_xTe$. However, no noticeable change in thickness for $Hg_{1-x}Cd_xSe$ was observed after etching for 30 seconds. Higher bromine concentrations were used—2.5% Br had an etch rate of ~250 nm/s, 1% Br an etch rate of ~75 nm/s. These etchants still left a rough surface when viewed under Nomarski microscopy, as seen in Figure 8-1 and Figure 8-2.
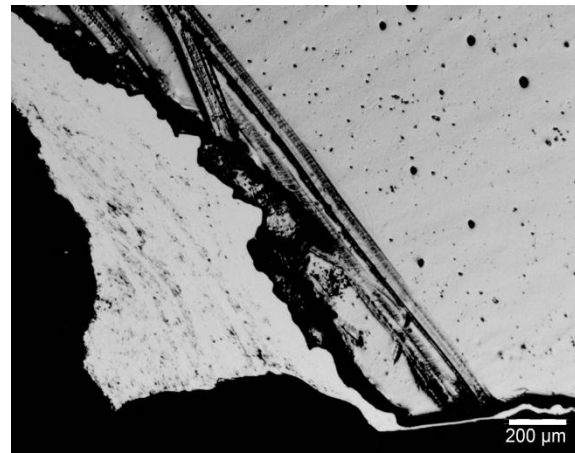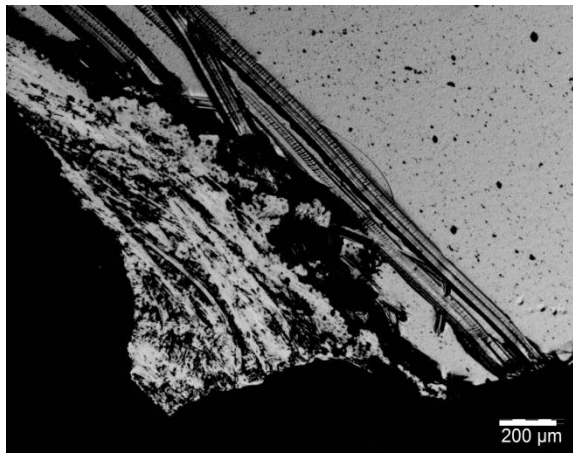
Figure 8-1: Sample SZ53 pre-etch (Left) and etched 10 seconds in 2.5% Br:MeOH (Right) viewed under Nomarski (x5).
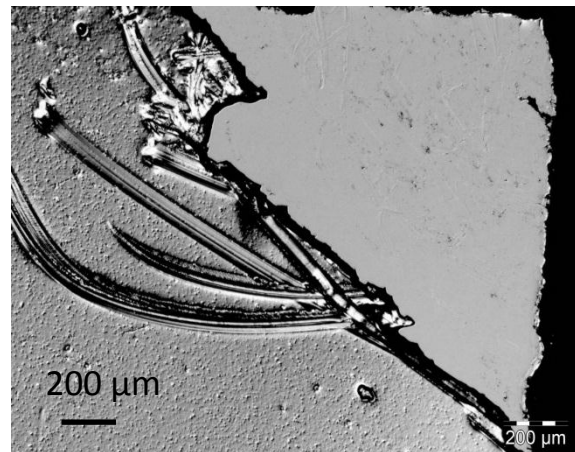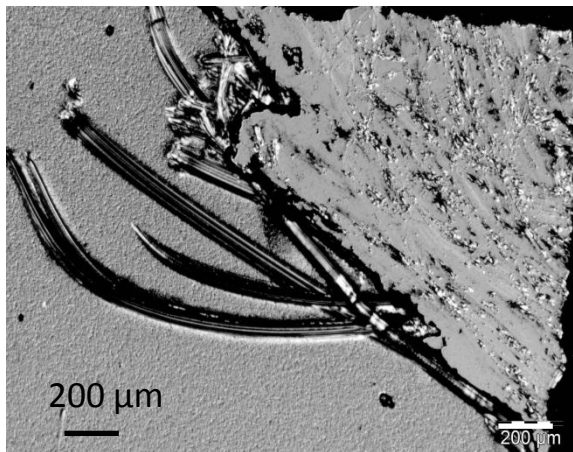

Figure 8-2: Sample SZ56 pre-etched (Left) and etched 30 seconds in 1% Br:MeOH (Right) viewed under Nomarski (x5).

Apparently higher bromine concentrations are required for etching $Hg_{1-x}Cd_xSe$. The 1% Br concentration that etches $Hg_{1-x}Cd_xSe$ at ~75 nm/s would etch $Hg_{1-x}Cd_xTe$ at ~117 nm/s. Since both alloys have Cd and Hg in common, the lower etch rate of $Hg_{1-x}Cd_xSe$ is likely due to Se having a slower removal rate than Te. If so, Br-MeOH etching also likely produces a Se-rich surface in $Hg_{1-x}Cd_xSe$. Further work is required to determine the relationships between etch rate and surface composition with the Br concentration of the etch solution. Additionally, the effects of Br-MeOH on GaSb need to be determined. If Br-MeOH reacts significantly with GaSb, another polishing etch may need to be developed for $Hg_{1-x}Cd_xSe$ grown on GaSb substrates.

8.2   Defect Etching

8.2.1   Etch Pit Density Measurements

The dislocation density of a sample can be measured through various techniques. Transmission electron microscopy (TEM) can image the dislocations directly, but TEM images are confined to such a small region that this technique is only viable for large dislocation densities ($<10^8$ cm^{-2}). As described in Section 3.9, cPL is another technique that can be used to measure dislocation densities, but is impractical for IR materials (particular LWIR). Thus dislocation densities are typically determined by etch pit density (EPD) measurements.

EPD requires an etch solution that etches the sample at different rates for different crystallographic orientations. Such an etch solution, referred to as a "dislocation etch," should have a slow etch rate for the orientation and polarity of the crystal surface. Dislocations in the material form a break in this orientation, and so the samples are etched at a faster rate around dislocations. As a result, a pit is formed around the dislocation which is visible under a microscope. Thus by etching samples in a dislocation etch and then viewing them under a

145

microscope, the density of the dislocations can be determined by the density of the etch pits. The size and morphology of the etch pits depends on the crystallography of the material and the composition of the etchant, but in general they appear as specific geometric shapes emanating from a single point (where the dislocation meets the surface) [53].

8.2.2 Mercury Cadmium Telluride

EPD is the standard technique for measuring the dislocation densities of $Hg_{1-x}Cd_xTe$, since dislocation densities in $Hg_{1-x}Cd_xTe$ are often too low to measure via TEM, and imaging $Hg_{1-x}Cd_xTe$ too problematic for cPL. Defect etchants were developed for (211)B $Hg_{1-x}Cd_xTe$, since (211)B is the standard crystallographic orientation for $Hg_{1-x}Cd_xTe$. Two such etchants are the Everson etch (originally developed for (211)B CdTe) and the Benson etch, which produces roughly triangular etch pits [47].

8.2.3 Mercury Cadmium Selenide

Since the potential advantage of $Hg_{1-x}Cd_xSe$ over $Hg_{1-x}Cd_xTe$ is its lower dislocation densities on a lattice-matched substrate, direct comparisons of the two materials will require EPD measurements of $Hg_{1-x}Cd_xSe$. Both the Everson and Benson etches had no effect on the $Hg_{1-x}Cd_xSe$ samples, most likely due to differences between telluride and selenide chemistry. Thus a new dislocation etchant must be developed for $Hg_{1-x}Cd_xSe$. Solutions of nitric and hydrochloric acids ($HNO_3:HCl$) had produced etch pits in HgSe and CdSe separately [56], and so various solutions containing HNO_3, and HCl, were used to etch $Hg_{1-x}Cd_xSe$ samples. All etches were followed by a 60 second rinse in a beaker overflowing with deionized water.

Figure 8-3 shows the trapezoid-shaped pits produced after etching sample SZ48 in a $HNO_3:HCl$ (2:1) solution for 10 seconds. The fact that the pits had regular shapes and were

oriented in the same direction suggests that they are dislocation etch pits. However, the bottom of an etch pit should converge at a single point (the dislocation) with clear faceted walls. These pits appeared to have flat bottoms, which is unusual. Etching SZ48 in HNO_3:HCl (5:4) for 20 seconds also produced trapezoidal pits with less clearly defined edges, and SEM images revealed what appear to be pits within the pits shown in Figure 8-4.

Various buffering agents were added to the etch solutions in order to slow down etch process. Also, indentations were made in the samples in order to create stress lines in the samples, as dislocations (and thus etch pits) are more likely to form around them. Solutions with lactic acid ($C_3H_6O_3$) produced pits along the stress lines, more clearly defined walls when viewed under SEM as seen in Figure 8-5. However, the pits still contained oddly flat bottoms. Phosphoric acid (H_3PO_4) was also used as a buffering agent. The trapezoidal etch pits from these solutions appeared to be deeper and come to more of a point, and appeared along stress lines as expected. Figure 8-6 exhibited what appear to be hexagonal etch pits in one region of sample SZ52 after etching in HNO_3:HCl:H_3PO_4 (8:4:1) for 20 seconds. When viewed under SEM, some of the pits appeared to be filled with particulates but others appeared to emanate from a single point with clearly faceted walls as expected for dislocations. This suggests that the "flat bottoms" observed for other etch pits could be due to the etched material residue re-collecting in the pit rather than being removed, obscuring the dislocation point.

Unfortunately, these hexagonal pits were not repeatable. The HNO_3:HCl:H_3PO_4 solutions had a light yellow color when initially mixed, but gradually turned dark orange after a few minutes, and the etch rate of the solution appeared to increase with the darker color. Thus the etching processes of the HNO_3:HCl:H_3PO_4 solutions were not consistent, making them unreliable as a dislocation etch. Further work is required to find the right solution that will serve
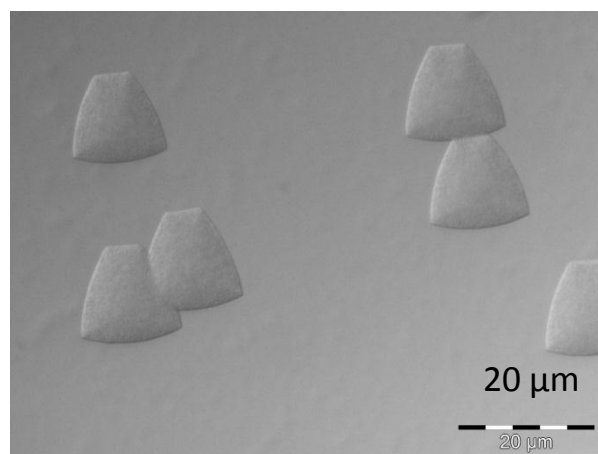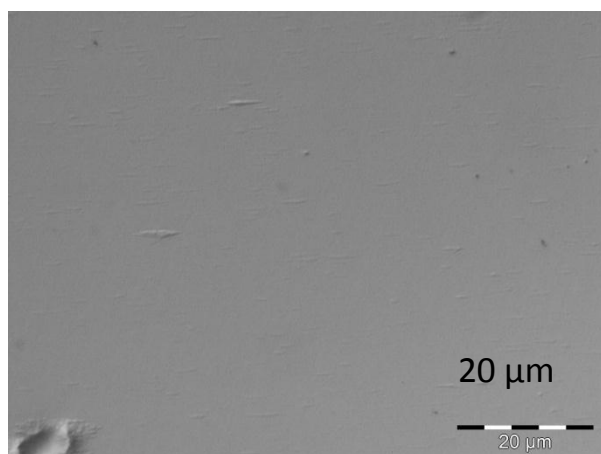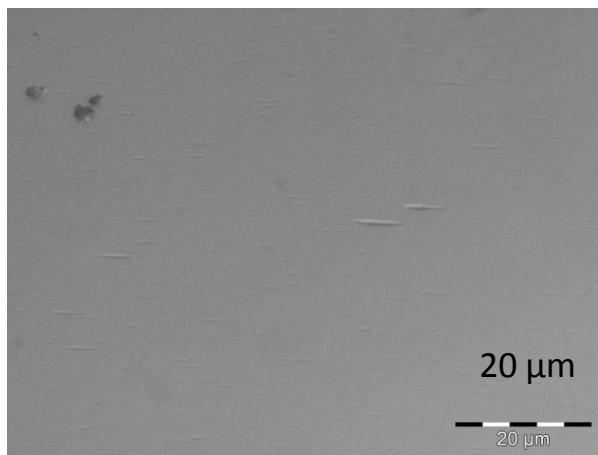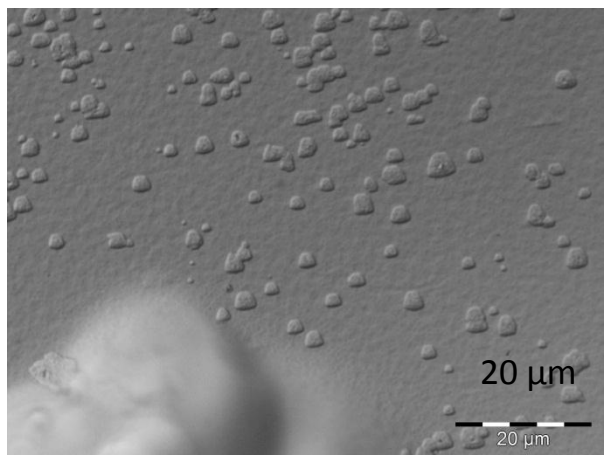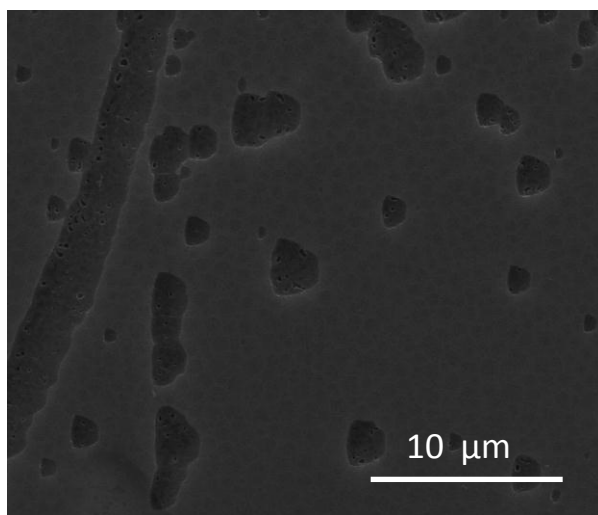
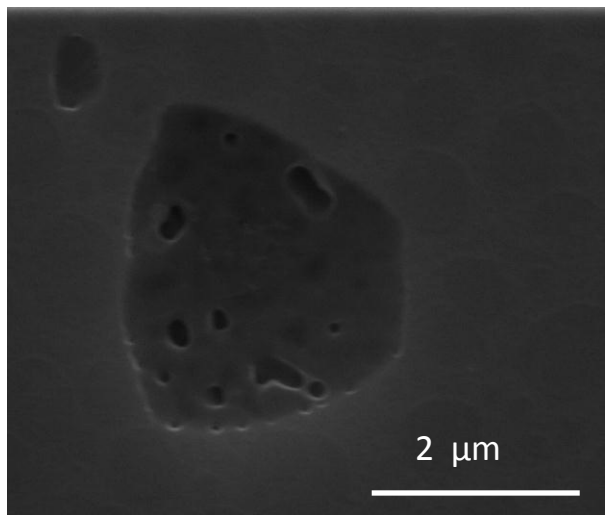**Figure 8-3: Sample SZ48 pre-etched (Left) and etched 10 seconds in HNO3:HCl (2:1) (Right) viewed under Nomarski (x100).**

(a)

(b)
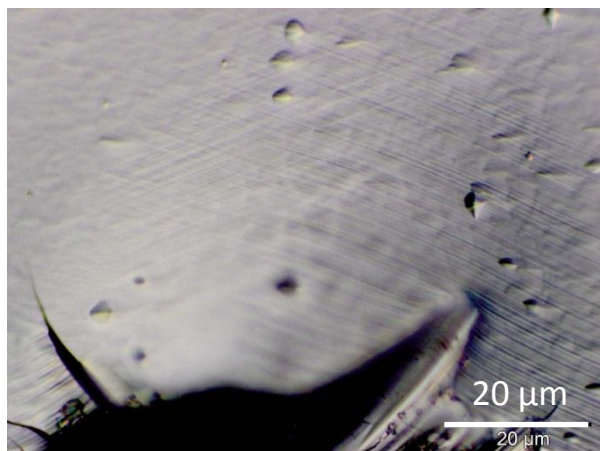

(c)
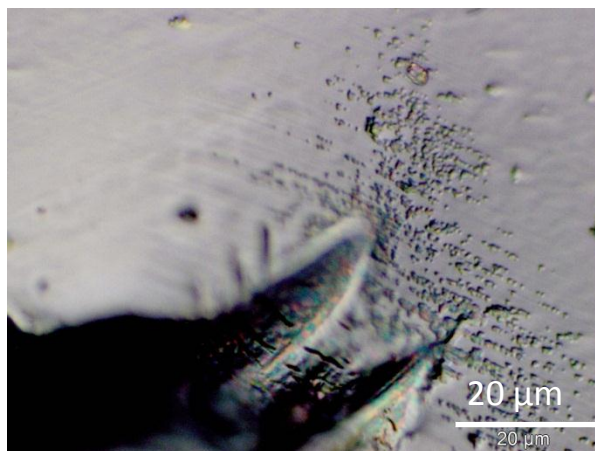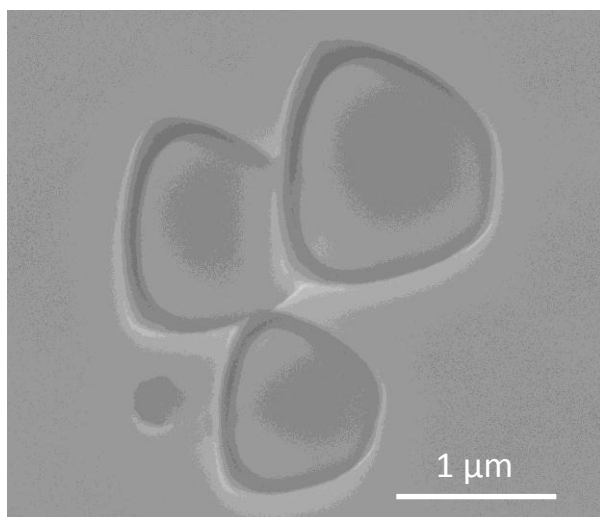

(d)

Figure 8-4: Sample SZ48 etched 20 seconds in HNO$_3$:HCl (5:4) (a) pre-etched, Nomarski x100 (b) etched, Nomarski x100 (c) etched, SEM x 4485 and (d) etched, SEM x 25,374.
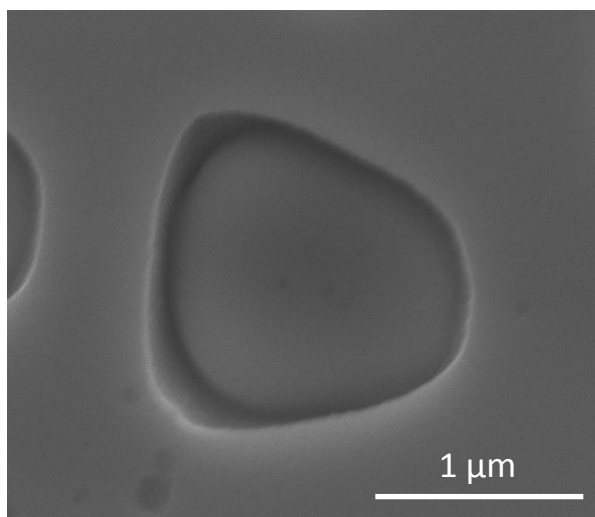
(a)

(b)

(c)

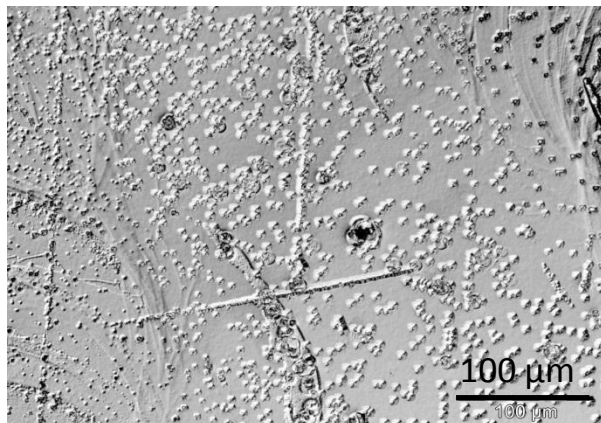

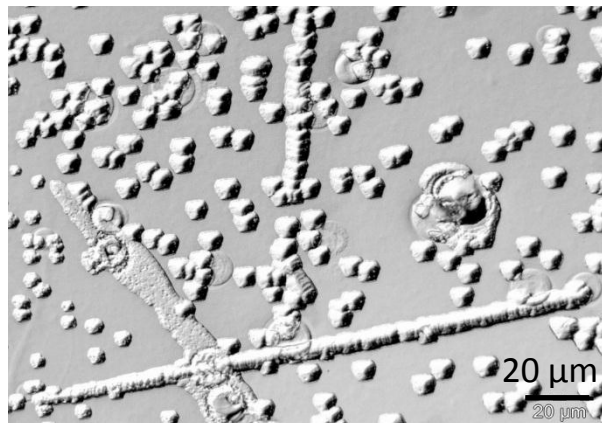(d)

Figure 8-5: Samples etched 20 seconds in HNO$_3$:HCl:C$_3$H$_6$O$_3$ (2:1:2) (a) SZ52 pre-etched, Nomarski x100 (b) SZ52 etched, Nomarski x100, (c) SZ50 etched, SEM x 39,749 and (d) SZ50 etched, SEM x 51,548.

(a)
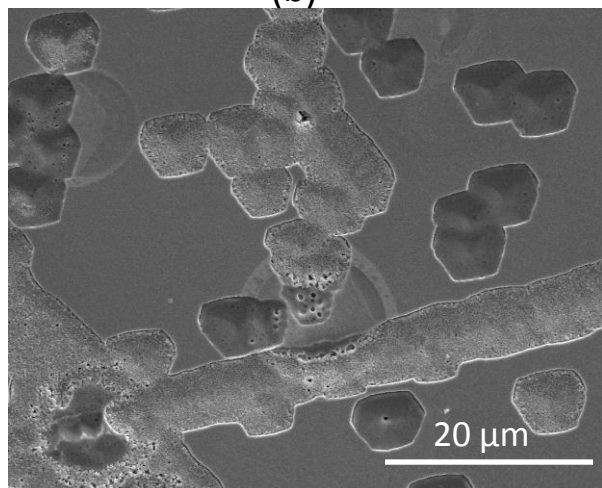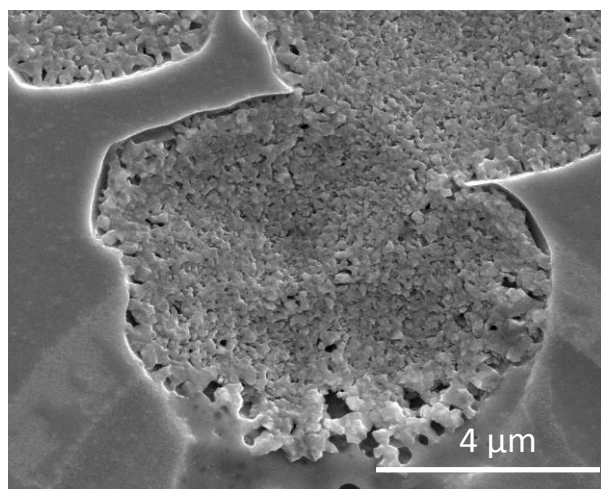
(b)
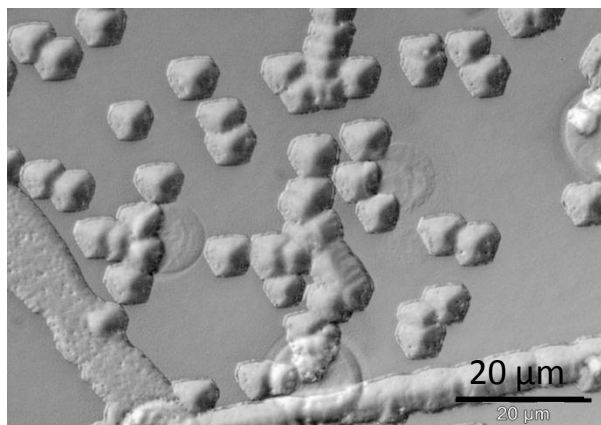
(c)

(d)

(e)
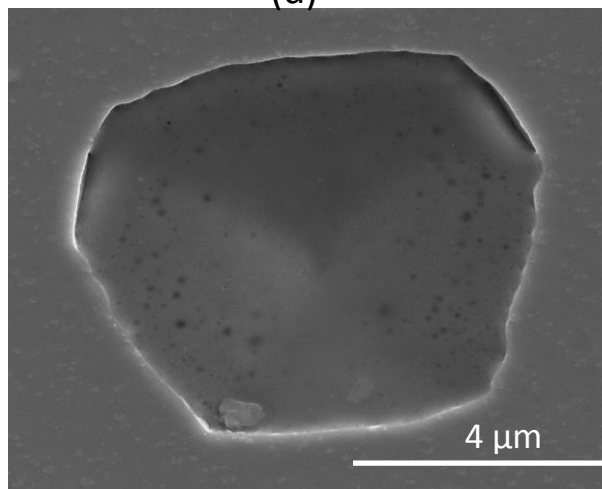
(f)

Figure 8-6: Sample SZ57 etched 20 seconds in HNO$_3$:HCl:H$_3$PO$_4$ (8:4:1) (a) Nomarski, x20 (b) Nomarski x50 (c) Nomarski x100 (d) SEM x 2554 (e) SEM x 13,536 and (f) SEM x 16,532.

151

as a consistent dislocation etch, but this initial research indicates it will have some combination of HNO_3 and HCl. Once a solution has been found that will consistently produce etch pits with clearly defined pointed bottoms, TEM measurements will be performed to confirm that the points correspond to a dislocation. This will allow EPD measurements to directly compare $Hg_{1-x}Cd_xSe$ with $Hg_{1-x}Cd_xTe$. Additionally, if the etchant reacts differently with GaSb than Si, a separate dislocation etchant may need to be developed for $Hg_{1-x}Cd_xSe$ layers grown on GaSb substrates.

References

[1] M. Z. Tidrow and W. R. Dyer, *Infrared Physics & Technology,* vol. 42, pp. 333-336, 2001.

[2] M. J. A. Butler, M. C. Mouchot, V. Barale and C. LeBlanc, *FAO Fish. Tech.Pap.,* vol. 295, p. 165, 1988.

[3] A. Rogalski, *Rep. Prog. Phys.,* vol. 68, pp. 2267-2336, 2005.

[4] M. A. Kinch, Fundamentals of Infrared Detector Materials, Bellingham, WA: SPIE Press, 2007.

[5] A. Rogalski, *Progress in Quantum Electronics,* vol. 27, pp. 59-210, 2003.

[6] S. M. Johnson, D. R. Rhiger and et. al., *J. Vac. Sci. Technol. B,* vol. 10, no. 4, pp. 1499-1506, 1992.

[7] M. A. Herman and H. Sitter, Molecular Beam Epitaxy: Fundamentals and Current Status, Heidelberg, Germany: Springer-Verlag, 1989.

[8] G. Brill, Y. Chen, P. Wijewarnasuriaya and N. Dhar, *Proc. SPIE,* vol. 7419, p. 74190L, 2009.

[9] T. Skauli, T. Colin, J. Sjolie and S. Lovold, *J. Elec. Mater.,* vol. 6, pp. 687-690, 2000.

[10] G. Brill, Y. Chen and P. Wijewarnasuriaya, *J. Elec. Mater.,* vol. 40, no. 8, pp. 1679-1684, 2011.

[11] J. Chai, K.-K. Lee, K. Doyle, J. H. Dinan and T. H. Myers, *J. Elec. Mater.,* vol. 41, no. 10, pp. 2738-2744, 2011.

[12] C. R. Whitsett, J. G. Broerman and C. J. Summers, *Semiconductors and Semimetals,* vol. 18, pp. 54-118, 1981.

[13] H. Foll, "Zinc Blende and Wurtzite," [Online]. Available: http://www.tf.uni-kiel.de/matwis/amat/semitech_en/kap_2/illustr/i2_1_2.html. [Accessed 22 January 2013].

[14] Y. Lansari, J. W. Cook Jr. and J. F. Schetzina, *J. Elec. Mater.,* vol. 22, no. 8, pp. 809-813, 1993.

[15] Y. Chen, S. Simingalam and et. al., *J. Elec. Mater.,* vol. 41, pp. 2917 - 2924, 2012.

[16] Tectra, [Online]. Available: http://tectra.de/evap.htm. [Accessed 2013].

[17] J. Margrave, Characterization of High Temperature Vapors, New York: John Wiley & Sons, 1967.

[18] K.-K. Lee, K. Doyle, J. Chai, J. H. Dinan and T. H. Myers, *J. Elec. Mater.,* vol. 41, pp. 2799-2809, 2012.

A. Olin, B. Nolang, E. Osadchii, E. Rosen and L.-O. Ohman, in *Chemical Thermodynamics*

[19]   *of Selenium*, Amsterdam, Elsevier, 2005, p. 89.

[20] Veeco Instruments, "Atom-H Source Specifications," 2005. [Online]. Available: http://www.veeco.com/pdfs/datasheets/atom_h_219.pdf.

[21] Veeco Instruments Inc., *Selenium Valved Cracker MArck V-500CC & 1200CC User Guide,* St. Paul, Mn: Veeco, 2011.

[22] J. F. Moulder, W. F. Stickle, P. Sobol and K. Bomben, Handbook of X-Ray Photoelectron Spectroscopy, Eden-Prarie, MN: Perkin-Elmer Corporation, 1979.

[23] K.-K. Lee, P. Weerasinghe and T. H. Myers, *Appl. Phys. Lett.,* vol. 100, pp. 052108 (1-4), 2012.

[24] M. Pluta, "Nomarski's DIC Microscopy: A Review," *Proc. SPIE ,* vol. 1846, p. 10, 1994.

[25] R. Reichelt, "Scanning Electron Microscopy," in *Science of Microscopy*, New York, Springer Science + Business Media LLC, 2007, pp. 133-272.

[26] Advanced Microanalysis Solutions, Genesis EDAX User's Manual, Mahwah, NJ: EDAX Inc., 2007.

[27] N. Jaggi and D. R. Vij, in *Handbook of Applied Solid State Spectroscopy*, New York, Springer Science + Business Media, LLC, 2006, pp. 411-449.

[28] C. J. Summers and J. G. Broerman, *Physical Review B,* vol. 21, no. 2, pp. 559-573, 1980.

[29] F. Giessibl, *Reviews of Modern Physics,* vol. 75, no. 3, pp. 949-983, 2003.

[30] N. Ashcroft and N. Mermin, in *Solid State Physics*, Orlando, Saunders College Publishing, 1976, pp. 95-99.

[31] T. Alford, L. Fledman and J. Mayer, in *Fundamentals of Nanoscale Film Analysis*, New York, Springer Science + Business Media LLC, 2007, pp. 129-151.

[32] J.-I. Kasai and Y. Katayama, *Rev. Sci. Instrum.,* vol. 66, pp. 3738-3748, 1995.

[33] D. Look, in *Electrical Characterization of GaAs Materials and Devices*, Bury St. Edmunds, St. Edmundburry Press, 1989, pp. 1-4.

[34] L. Van der Pauw, *Phillips Research Reports,* vol. 13, pp. 1-9, 1958.

[35] J. Meyer, C. Hoffman, J. Antoszeswki and L. Farone, *J. Appl. Phys.,* vol. 81, no. 2, pp. 709-713, 1997.

[36] M. D. McCluskey and E. G. Haller, Dopants and Defects in Semiconductors, Boca Raton, FL: CRC Press, 2012.

[37] C. Smith, P. C. Rice-Evans, N. Shaw and D. L. Smith, *J. Phys.: Condens. Matter,* vol. 4, pp. 5825-5834, 1992.

[38] V. Slugen, "What Kind of Information we can Obtain from Positron Annihilation Spectroscopy," European Commission Joint Research Center, Brussels, 2006.

[39] P. Shultz and K. Lynn, *Reviews of Modern Physics,* vol. 60, no. 3, pp. 701-779, 1988.

[40] R. Krause-Rehberg, "Fundamentals of positron annihilation spectroscopy," [Online]. Available: positron.physik.uni-halle.de/talks/ICPA-15_ISPS_lecture_RKR.pdf. [Accessed May 2012].

[41] H. R. Varna, in *Atomc and Nuclear Analytical Methods*, Berlin, Springer Berlin-Heidelberg, 2007, pp. 91-140.

[42] D. Drews, J. Sahm, W. Richter and R. T. D. Zahn, *J. Appl. Phys.,* vol. 78, pp. 4060-4065, 1995.

[43] M. C. Tamargo, J. L. de Miguel, D. M. Hwang and H. H. Farrell, *J. Vac. Sci. B,* vol. 6, pp. 784-787, 1998.

[44] J. Singh, in *Electronic and Optoelectronic Properties of Semiconductor Structures*, New York, Cambridge University Press, 2003 , pp. 110-111, 181-191.

[45] L. S. Hirsch, Z. Yu and et. al., *J. Electron. Mater.,* vol. 26, pp. 534-541, 1997.

[46] L. Ouyang, J. Fan and et. al., *J. Cryst. Growth,* vol. 330, pp. 30-34, 2011.

[47] J. D. Benson, L. O. Bubulac and et. al., *J. Elec. Mater.,* vol. 39, pp. 1080-1086, 2010.

[48] J.-P. Faurie, *Prog. Crystal Growth and Charct.,* vol. 29, pp. 35-159, 1994.

[49] Y. Chang, C. R. Becker and et. al., *J. Elec. Mater.,* vol. 37, pp. 1171-1183, 2008.

[50] H. Cheng, J. M. DePudyt, M. A. Haase and J. E. Potts, *J. Vac. Sci. Technol. B,* vol. 8, no. 2, pp. 181-186, 1990.

[51] K. Kumazaki, E. Matsushima and A. Odajima, *Phys. Status Solidi. A.,* pp. 579-, 1976.

[52] J. Rosbeck, R. Starr, S. Price and K. Riley, *J. Appl. Phys.,* vol. 53, pp. 6430-6440, 1982.

[53] J. L. Wehyer and J. J. Kelly, in *Handbook of Crystal Growth*, Berlin, Springer Berlin-Heidelberg, 20120, pp. 1453-1476.

[54] Z. Li-yao, Q. Hui, X. Jin-tong and X. Xiang-yang, *Proc. of SPIE,* vol. 8193, p. 81399T , 2011.

[55] W. H. Chang, T. Lee and W. M. Lau, *J. Appl. Phys.,* vol. 68, pp. 4816-4819, 1990.

[56] P. Walker and W. H. Tarn, in *CRC Handbook of Metal Etchants*, Boca Raton, FL, CRC Press LLC, 1991, pp. 221,809.